Università degli Studi di Ferrara

DOTTORATO DI RICERCA IN FISICA

CICLO XXVIII

COORDINATORE Prof. Vincenzo Guidi

Advanced modeling for studying antineutrinos and gamma rays coming from the Earth

Settore Scientifico Disciplinare FIS/07

Dottoranda
Dott.ssa Virginia Strati

Tutor
Prof. Giovanni Fiorentini

Co-Tutor
Prof. Fabio Mantovani

Anni 2013/2015

Contents

Overview 7

Chapter 1 11

Mapping the natural radioactivity in Veneto region throughout the integration of γ-ray measurements 11

1.1 Background 12
1.2 Geological setting 12
1.3 Reference geological map and sampling strategy 14
1.4 HPGe laboratory measurements and data analysis 16
1.5 Airborne γ-ray data and data analysis 17
1.6 Mapping radiometric data 18
1.7 Final remarks 19

Chapter 2 21

Advanced analysis and modeling algorithms for spatial γ-ray data of Variscan Basement (Northeastern Sardinia) 21

2.1 Background 22
2.2 Geological setting 23
2.3 Methods 24
2.4 Mapping radiometric data 26
2.5 The Arzachena pluton 31
2.6 Final remarks 32

Chapter 3 35

A multivariate spatial interpolation of airborne γ-ray data using the geological map as constraining variable 35

3.1 Background 36
3.2 Geological setting 36
3.3 Experimental setup, survey and data 38
3.4 Collocated cokriging: theoretical background 40
3.5 Interpolating airborne γ-ray data on geological constraints 41

3.6 Results and discussions 47
Chapter 4 55
Geological characterization of the oil fields of Vlora-Elbasan region (Albania) supporting the assessment of Naturally Occurring Radioactive Materials (NORMs) 55
4.1 Background 56
4.2 Geological setting 57
4.3 Sample collection 58
4.3.1 Kuçova oilfield 58
4.3.2 Marinza oilfield 59
4.3.3 Ballsh-Hekali oilfield 60
4.4 Sample preparations and measurements 61
4.4.1 HPGe gamma-ray spectrometry measurements 61
4.4.2 X-ray diffractometry measurements 62
4.5 Results and discussions 62
4.5.1 Activity concentrations in soil samples 62
4.5.2 Activity concentrations in sludge samples 67
4.5.3 Activity concentrations in oil-sand samples 67
4.6 Radiological assessment 69
4.7 Final remarks 70
Chapter 5 73
A 3D geophyisical and geochemical model of the crust surrounding the Sudbury Neutrino Observatory (SNO+) for the prediction of geoneutrino flux 73
5.1 Background 74
5.2 Constructing the model 75
5.3 Geology framework of the regional crust 78
5.3.1 Superior Province 79
5.3.2 Grenville Province 80
5.3.3 Southern Province and Sudbury Igneous Complex 80
5.3.4 Palezoic sedimentary units 81
5.3.5 Simplified surface geology 81
5.4 Geophysical 3-D model of the Regional Crust 82
5.4.1 Geophysical model of boundary surfaces 83

5.4.2 Geophysical model of regional upper crust 86
5.4.3 Cross-checking the 3-D model 88
5.5 Chemical composition of the crust near SNO+ 89
5.6 Geoneutrino signal 93
5.7 Discussions 95
5.7.1 Heat production 95
5.7.2 Mantle geoneutrino signal 97
5.8 Final remarks 99
Chapter 6 101
Expected geoneutrino signal at JUNO 101
6.1 Background 101
6.2 Methods 103
6.3 Results and discussions 105
6.4 Final remarks 109
Future perspectives 111
Bibliography 115

Overview

Our planet is far to be well-known and to date open questions about its formation and composition still remain. Geophysicist and geochemists are trying to answer to the question 'how works the Earth interior?', defined in 2005 by the Science journal as one of the most relevant among the unresolved questions. However direct investigations deeper than tens kilometers are missing and the model-based composition of the mantle is affected by a lot of sources of uncertainty. A better determination of the radiogenic energy budget is essential to bind the main geophysical and geochemical processes that have driven the evolution of the Earth. The studies conducted during my research activities in these years gave me the opportunity to take part in this scientific debate.

Combining experimental results of geoneutrino signals at operating and future experiments, can place better constraints on the mantle signal and in turn on its composition. In this perspective a deep understanding of the continental crust, in particular the region immediately surrounding the detector, is mandatory. Going to a bigger scale, the study of heat producing elements and the previsions of their distribution are key-points for the understanding of local geological processes affecting the crust as well as for the investigation of environmental radioactivity.

In these years I dealt the problematic aspects related to the numerical and cartographic modeling at different scales and I proposed operative solutions regarding mainly the study of statistical distributions, the treatment of the input and output uncertainties and the combination of multivariate information. This thesis presents the scientific challenges and the goals supporting the advanced modeling for the spatial analysis of gamma-ray data and for the predictions of geoneutrinos signal from the Earth. Although at a first sight these two topics appear distant, based on different measurement techniques and fields of view, they are strictly connected: in both the cases the natural radioactivity represents a probe for the study of the properties of Earth’s surface and interior.

The unstable nuclei, i.e. radioactive nuclei, reach a lower energy status emitting particles (alpha or beta decays) or electromagnetic waves (gamma decay). When alpha decay occurs, the instable nucleus emits a helium nucleus (or alpha particle) and become a nucleus with reduced mass number and atomic number. During beta decay the mass number remains constant, because a neutron is transformed into a proton with the emission of an electron (beta minus decay) or vice versa with emission of a positron (beta plus decay or electron capture). Commonly, an excited nucleus, originated from alpha or beta decay, emits gamma rays to reach the nucleus ground state. The energy conservation law, in the case of beta

decay, is ensured by the emission of a neutral and nearly no mass particle, the antineutrino in the case of beta minus decays and the neutrino in the other cases.

Terrestrial radioactivity is due to naturally occurring radioactive isotopes (^{238}U, ^{232}Th, ^{40}K, ^{235}U and ^{87}Rb) with half-lives comparable to the Earth's age. Among them, the potassium and some radioisotopes in the uranium and thorium decay chains emit gamma-rays having energy of the order of MeV and can be easily detected. Indeed, these highly energetic electromagnetic waves are the most penetrating of the radiations in contrast to the highly ionizing alpha and beta particles that are easily adsorbed by matter, including the atmosphere. This makes the gamma ray spectroscopy a powerful tool for the identification and quantification of radionuclides and in turn the study of their spatial distribution. Originally developed mainly in the mineral exploration field, gamma ray surveys performed in laboratory, in field setting and from aircraft permit monitoring the environmental radioactivity as well as provide valuable insights on geological mapping, structural geology and soil surveying. Furthermore, the assessment of the natural background radiation is essential in case of nuclear fallout, for the location of lost radioactive sources and in the study of radon prone areas.

The gamma rays surveys, in which I was involved in my PhD, were performed through the use of NaI (sodium iodide) and HPGe (Hyper Pure Germanium) detectors. Due to the high efficiency and the good spectral resolution, the NaI detectors are scintillation detectors used during ground surveys and airborne surveys. In particular the portable ZaNaI (Zaino NaI) detector, being able to perform real-time measurements, is mainly suitable in the case of presence of a good exposure of rocks. For example this method used in the case study of the Northeastern Sardinia survey, allowed for frequent granitic outcrops that facilitated collecting a statistically significant dataset that stimulated detailed geostatistical analyses. The AGRS_16L, an advanced modular NaI detector further equipped with auxiliary instruments, is particularly efficient for the extensive survey of wide areas like the wide plain in the Veneto region. For the laboratory measurements, the most commonly used instruments are the HPGe detectors, semiconductor detectors characterized by a high energetic resolution that assures a very low uncertainty for the activity concentration of K, U and Th. In particular the fully automated MCA_Rad system made possible the characterization of the radioactivity content for thousands of rock and soil samples.

While in the last decades gamma-rays spectroscopy became a well consolidated technique, only in 2005 the KamLAND experiment confirmed for the first time the detection of geoneutrinos, i.e. electron antineutrinos produced in beta decays along the uranium and thorium decay chains. Indeed only antineutrinos produced in four beta transitions, two each in the in the ^{238}U and ^{232}Th chains, have energy greater than 1.8 MeV, the threshold energy for the current detection mechanism, the inverse beta reaction. The construction of large-mass detectors in underground laboratories, SNO+ in Canada and JUNO in China, represents the

attempt to face the challenges of detecting geoneutrinos. Thanks to the Earth shinning with 10^{25} antineutrinos per second and organic liquid scintillators with huge quantities of target mass, we can detect the reaction between an antineutrino and a proton creating the uniquely distinctive signature of a geoneutrino event. Geoneutrinos are able to pass through most matter without interacting, they could, in theory, zip straight through more than a trillion kilometers of lead. So they can bring to surface useful information about the planet's composition and specifically determine its radiogenic element budget. In the last decade, thanks to the progresses in the understanding of neutrino physics (i.e. oscillation parameters) and in the technological development of low background neutrino detectors, the geoneutrino detection comes forward as a new method for exploring the Earth's interior. Borexino (Italy) and KamLAND (Japan) are two operating detectors which periodically publish new experimental data of geoneutrinos measurements that could be combined with the data from the future low background detectors, SNO+ and JUNO.

In these three years, my research activity took part in this scientific framework giving the valuable opportunity to insert me in a well consolidated and multidisciplinary network. In the 2015 the participation to the International workshop on KamLAND Geoscience (Tokyo) and to the Neutrino Geoscience Conference (Paris) were for me the occasion to present the recent results of my activity to the international community. Moreover the recent period spent during my research visit at University of Maryland, together with the joining to the JUNO collaboration, favored a fruitful exchange and permitted to me to focus on the open questions still remaining.

The contents of this thesis are included in 6 published works realized with the involvement of about 30 coauthors, geologists and physicists, from different areas in the world. In each of the following chapters a specific case study is presented from a particular point of view shedding light on my contribution.

In Chapter 1 is presented the map of terrestrial natural radioactivity of the Veneto region (Italy) obtained on the basis of an integrated gamma-ray dataset composed by laboratory measurements performed on rock samples and airborne measurements. I integrated these two different types of data in a unique cartographic product, using suitable geostatistical algorithms based on the distinctive geological and morphological features of the investigated areas. Moreover I addressed the problem related to the significant percentage of measurements below the minimum detection limit and applied well-known estimation methods to reconstruct the probability density functions for the radiological characterization of the analyzed rocks.

The uranium distribution map of the Northeastern Sardinia, coming from a very refined radiometric investigation, is presented in Chapter 2. The γ-ray spectroscopy measurements, realized with two different methods, are characterized by heterogeneous measurement errors. Taking on this challenge, I applied a particular geostatistical method that

permitted to analyze the input and the output uncertainties. In the estimation process the degree of the confidence associated to two different gamma-ray techniques is taken in account leading to an original cartographic product.

Chapter 3 describes a multivariate spatial interpolation used in the case of airborne gamma ray survey of Elba Island (Italy) for obtaining the radiometric maps using the geological map as a constraint. I dealt with the complex aspects of correlating quantitative data (γ-ray measurements) with the qualitative information of the geological map. The realization of the radiometric maps, in which I was actively involved, permitted us to test this geostatistical approach examining possible bias of the multivariate interpolation.

An extensive survey in one of the most oil productive regions (Vlora-Elbasan) in Albania is presented in Chapter 4 for the assessment of Naturally Occurring Radioactive Materials. My tasks concerned the analysis of the geological aspects of the surveys performed through the textural characterization of soil samples and the interpretations of the results in term of radionuclides abundances and mineralogical analysis. This led to emphasize the strong correlation between geological information and radioactivity content. In particular I participated in discussions about the description activity concentrations measurements based on geological and geochemical arguments. The discrimination of the lithologic features of the oil fields and the test of geodynamic models can result strategic issues for the planning of the future radiological assessment of the region.

Chapter 5 presents a detailed 3D model compiled from geological, geophysical, and geochemical information that provided the estimation of the geoneutrino flux expected at the SNO+ detector (Canada). I developed the geophysical construction of a 3D structural model of the region, dealing with the related aspects to the complexity of the modeling the prediction of the geoneutrino flux. In particular I applied the method of Ordinary Kriging to local seismic inputs for modeling of the local crustal structure. For the first time the masses of the main crustal reservoirs containing U and Th are estimated together with their uncertainties. Together with geochemical uncertainties, these results are crucial for a reliable estimation of geoneutrino signal in SNO+.

Chapter 6 provides the first estimation of the geoneutrino signal expected at JUNO together with an estimate of the expected reactor antineutrino signal. The location of the experiment, very close to two planned nuclear plants, allows for the main goal of JUNO, which is the study of the hierarchy mass of the neutrino using reactor antineutrinos. I produced the geoneutrino spectra and the relative uncertainties providing a result that will be a reference point and a guide for future refinements. In particular, I calculated the ratio between reactor antineutrino and geoneutrino signals considering the two under construction reactors operating or switched off, addressing strategic results for the analysis of the sensitivity of JUNO to the geoneutrino measurements.

Chapter 1

Mapping the natural radioactivity in Veneto region throughout the integration of γ-ray measurements

In this Chapter it is presented the first detailed map of the terrestrial natural radioactivity of the Veneto region, one of the main results of the research project Rad_Monitor in which I was directly involved. The investigated territory shows a clear separation from the geologic and morphologic point of view that distinguishes a mountain belt from a wide alluvial plain. For this reason, the research group decided to use two different measurement and analysis methods. The characterization of the geological formations, performed through the same strategy followed in the extensive survey in the Tuscany Region (Italy) [*Callegari et al.*, 2013], was matched with an airborne survey of the quaternary deposits of the plain areas. The activity concentration of ^{40}K, ^{238}U and ^{232}Th in 709 representative rock samples of the main Alpine lithostratigraphic units were measured by using high-purity germanium (HPGe) detectors to characterize the radioactivity content of the 41 Cartographic Units (CU) of the Veneto Lithostratigraphic map at 1:250,000 scale. An area accounting for 61% of the territory, comprising alluvial plains was investigated through airborne γ-ray measurements.

I was assigned to perform the statistical treatment of the rock analysis and the spatial interpolation of the airborne γ-ray measurements and in turn I integrated them into an unique cartographic product. This delicate issue resulted as the most difficult challenge of this study due to the different statistical distributions of the two datasets and also to the heterogeneous uncertainties of the γ-ray data. For the integration of the results and the elaboration of a unique descriptive legend, I chose appropriate statistical and geostatistical interpolators taking into account the types of data source, the nature of the investigated areas and the spatial resolution of the final map. The different contributions of the uncertainties, negligible in comparison to the overall error of the output model, are not analyzed. This aspect is widely faced in case study in the Northeastern Sardinia described in Chapter 2.

This case study represented for me also the opportunity to deal with a considerable problem that the scientific community have to face in many fields, namely the treatment of the censored data [*Helsel*, 1990]. Indeed, due to the geochemical features of the analyzed lithologies (mainly limestone and dolomites), the analysis of HPGe measurements highlights the presence of a relevant fraction of Minimum Detectable Actvity (MDA). This evidence stimulated an accurate research of an appropriate method that led to the application of well-known estimation methods to reconstruct the probability density functions for the radiological characterization of the analyzed rocks.

This study represents the first detailed investigation of the terrestrial natural radioactivity of the Veneto region and at the same time opened new scientific and technologic perspectives for the future. Indeed the obtained results encouraged detailed focuses on the correlations existing between the radioactivity content and anthropogenic activities, hydrogeology information and structural interpretations.

1.1 Background

Following the IAEA (International Atomic Energy Agency) recommendation for the development of radioelement baseline maps [*IAEA*, 2010] here the total radioactivity map of the Veneto Region (Italy) (Annex A) is presented, based on γ-ray spectroscopy measurements. A map of the natural radioactivity content is a basic component for supporting research in physics, Earth and life sciences. Many research projects have focused on the absorbed dose distribution due to the natural background radiation [*Grasty*, 2004] or on mapping the geogenic radon considering the distribution of the geological units [*Kemski et al.*, 2001]. Although different research teams in the Veneto Region studied the indoor exposure to natural radioactivity [*Trotti et al.*, 1994] and mapped the areas with elevated indoor radon levels [*Trotti et al.*, 1998], a map of the activity concentration is still a missing piece of knowledge in a region with one of the highest population densities in Europe.

The mountainous areas were investigated following the Geological map with the reconnaissance of lithostratigraphical units division at scale 1:250,000: a sampling strategy was planned to characterize the 41 Cartographic Units (CU) on the basis of the radiometric responses of 709 representative rock samples. In the quaternary plain deposits, the distribution model of the activity concentration was obtained by geostatistical interpolation of the airborne γ-ray measurements, spatialized using the Ordinary Kriging interpolator. The map of total natural radioactivity of the Veneto Region is realized by using statistical arguments for combining all the data into a unitary and coherent cartographic reference frame.

1.2 Geological setting

The mountainous areas of Veneto are characterized, from the geological point of view, by rocks deformed during the Alpine orogeny, a mountain-building event that affected a broad segment of Southern Europe and the Mediterranean region during the Paleogene and Neogene periods (65.5 to 2.6 millions of years ago).

The Alpine orogeny has been linked with the Cretaceous-Tertiary convergence that led to the disappearance of the Piemont-Liguria Ocean and to the subduction of the European plate beneath the African plate (Miocene). The Alps belong to the Alps-Himalaya orogenetic system, composed of relatively young mountains (Cretaceous-Paleogene) having a crustal

structure characterized by opposite vergence. Two main tectonic systems are distinguishable: the European chain, with a W-NW vergence, and the Southern Alps, with a S-SE vergence.

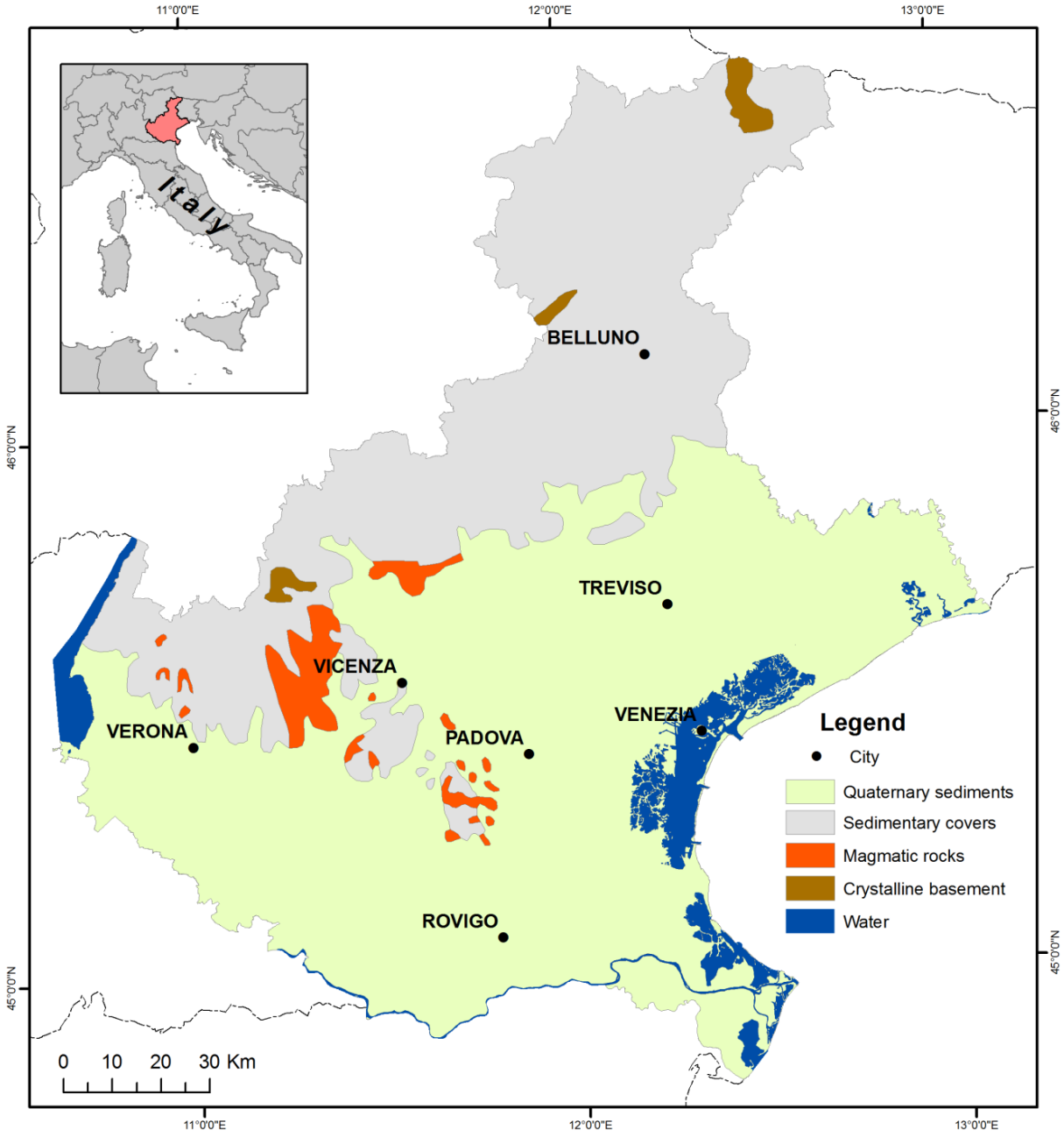

Figure 1.1 Schematic lithostratigraphic map of the Veneto Region**.**

The stratigraphic succession of the Veneto Region, completely included in the Subalpine Domain, is formed by a Paleozoic crystalline basement and by sequences of sedimentary and volcanic covers (from Permian to Quaternary) (Figure 1.1). The crystalline basement, made up of metamorphic rocks (metasandstones, metabasalts, phyllites, metarhyolites), is the product of recrystallization and deformation processes undergone by sedimentary and volcanic rocks. The basement outcrops are confined in the Recoaro (western sector of Veneto Region), Comelico and Agordo (northern sector) areas.

The extended sedimentary covers (see Figure 1.1) are characterized by the presence of Paleozoic rocks (volcanic, sandstone, limestones and marls), Mesozoic rocks (mainly dolomites, limestone and marls) and Tertiary sequences (sandstones and conglomerates) in flysch and molasses facies.

The volcanic rocks, mainly outcropping on Recoaro area and Euganean Hills, represent the evidences of two different magmatic cycles. The first cycle (Triassic, Recoaro area) refers to early products of rhyolitic, rhyodacitic and dacitic composition, followed by rhyolitic-dacitic flows and products of andesitic and basaltic compositions. The second cycle (Paleogene, Euganean Hills) is related to an intense effusive activity, characterized by the presence of basalt lava flows, hyaloclastite, breccias and volcanic dikes.

The Subalpine Domain is covered by Quaternary sediments originated by erosion and transport processes. These sediments include moraine deposits and sequences of alluvional materials constituted by fluvial, lake and marsh deposits.

1.3 Reference geological map and sampling strategy

The geological map of Veneto at 1:250,000 scale [*Antonelli et al.*, 1990] was used as a guide for the natural radioactivity survey. The Veneto Region (18,264 km²) was classified into the Southern Alpine sector and Hill areas (SAH), covering approximately 39% of the territory, and into a wide River Plain area (RP) for the remaining 61% of the territory, constituted by Quaternary alluvial deposits of the Po, Adige, Brenta, Piave and Tagliamento rivers.

Figure 1.2 Collection of fresh rock sample from representative outcrop.

The 41 CU in the SAH areas were investigated by collecting 709 rock samples, following the sampling strategy described in [*Callegari et al.*, 2013], and obtaining an overall average of one data per 25 km^2. In particular outcrops representative of each CU were explored collecting fresh rock samples (Figure 1.2).

The quaternary deposits of the RP areas were investigated by airborne γ-ray spectrometry (AGRS) measurements [*Guastaldi et al.*, 2013] performed in approximately 75 h of effective flight, which correspond to approximately 7,000 km line. Figure 1.3 shows the locations of the collected rock samples and the effective flight lines performed during the AGRS survey.

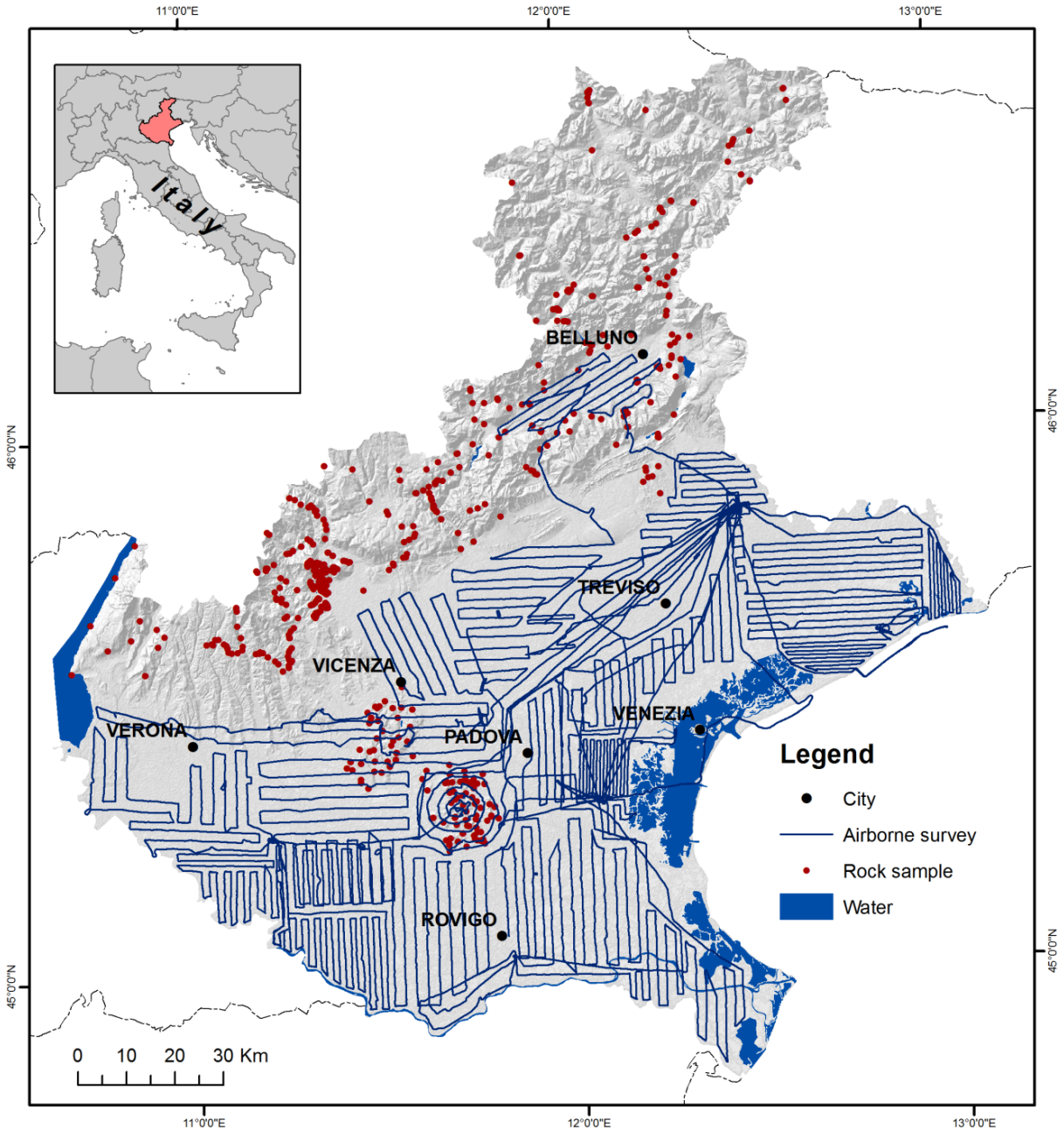

Figure 1.3 The locations of the collected rock samples and the effective flight lines: the maximum line spacing is approximately 2.5 km.

1.4 HPGe laboratory measurements and data analysis

The activity concentrations of ^{40}K, eU (equivalent uranium) and eTh (equivalent thorium) in 709 representative rock samples were measured using the MCA-Rad system (Figure 1.4), a gamma-ray spectrometer equipped with two HPGe p-type detectors having a 60% relative coaxial efficiency and an energy resolution of approximately 1.9 keV at 1332.5 keV (60Co) [*Xhixha et al.*, 2013]. The MCA_Rad system is accurately shielded with 10-cm thickness of copper and 10-cm thickness of lead by reducing the laboratory background of approximately two orders of magnitude. The absolute peak energy efficiency of the MCA_Rad system is calibrated using certified reference materials (RGK_1, RGU_1 and RGTh_1) traceable by the International Atomic Energy Agency (IAEA) [*Xhixha et al.*, 2015]. The total uncertainty for the absolute peak energy efficiency is estimated to be less than 5%. Prior to measurement, each rock sample was crushed, homogenized and sealed in a cylindrical polycarbonate container of 180 cm^3 volume. Then, the samples were left undisturbed for at least four weeks to establish radioactive equilibrium in the ^{226}Ra decay chain segment. Each sample was measured for 3600 seconds with a statistical uncertainty generally less than 10% for eU. Less than 2% of the measurements are below the minimum detection activity of ~2.5 Bq/kg.

The activity concentrations of ^{40}K, eU, eTh of the 41 CU were characterized by means of the 709 rock samples. The dataset is composed of a relevant fraction of the Minimum Detectable Activity (MDA) values, corresponding approximately to 9.4 Bq/kg for ^{40}K, 2.5 Bq/kg for eU and 3.7 Bq/kg for eTh, mainly found in the carbonate rocks. The distribution function for each dataset was graphically studied using univariate statistics by means of both frequency histograms and percentage-probability P-P plots to gain a first insight into the data structure. The Kolmogorov-Smirnov statistical test was applied to discriminate the normal and lognormal distributions, providing a p-value (usually $p < 0.05$) adopted as the figure of merit for rejecting the null hypothesis. The MDA values were properly treated on the basis of the statistical arguments described in [*Helsel*, 1990]. We verified that the distributions of ^{40}K, eU and eTh are generally well fitted by a lognormal function (Figure 1.7). The total activity was calculated for each CU and the uncertainty propagation was evaluated using a Monte-Carlo method [*BIPM et al.*, 2008].

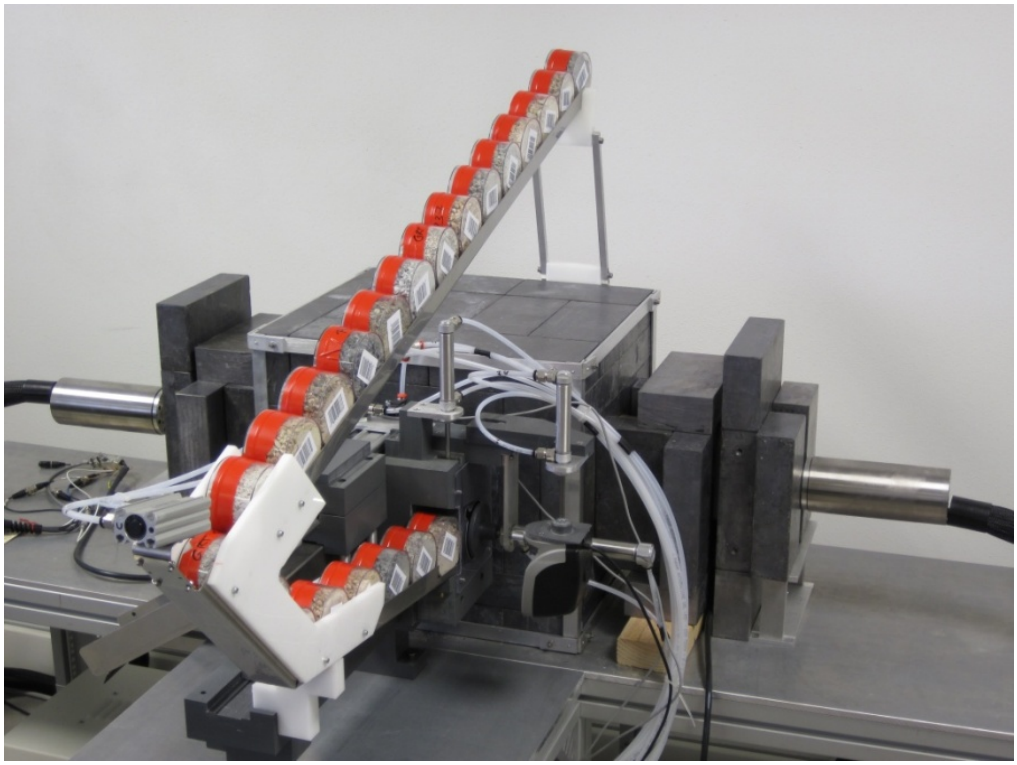

Figure 1.4 View of the MCA_Rad system.

1.5 Airborne γ-ray data and data analysis

The AGRS measurements were performed using a modular instrument, called AGRS_16.0L (Figure 1.5), composed of four NaI(Tl) detectors (10 cm × 10 cm × 40 cm each) with a total volume of approximately 16 Liters mounted on an autogyro [*Guastaldi et al.*, 2013] (Figure 1.6). The system is further equipped with an "upward-looking" NaI(Tl) detector of 1 L, partially shielded from the ground radiation and used to account for the atmospheric radon correction. The position of the AGRS_16.0L system is recorded using a GPS antenna, and the height above the ground is calculated by applying the Laplace formula, starting from the pressure and temperature values measured by dedicated sensors.

The radiometric data acquired during the AGRS survey was analyzed offline by first integrating the measured events in 12s interval γ-spectra. The γ-spectra are then calibrated and analyzed using the Full Spectrum Analysis with Non-Negative Least Squares constraints (FSA-NNLS) as described in [*Caciolli et al.*, 2012]. The activity concentrations of ^{40}K, eU and eTh at ground level were determined by applying several corrections to the measured signals, as described in [*Guastaldi et al.*, 2013] (see Chapter 3): cosmic background corrections, topography corrections, variation in flying altitude and height corrections, atmospheric radon corrections. Finally, the approximately $19 \cdot 10^3$ radiometric data of the ^{40}K, eU and eTh concentrations obtained, were used to calculate the total activity concentration.

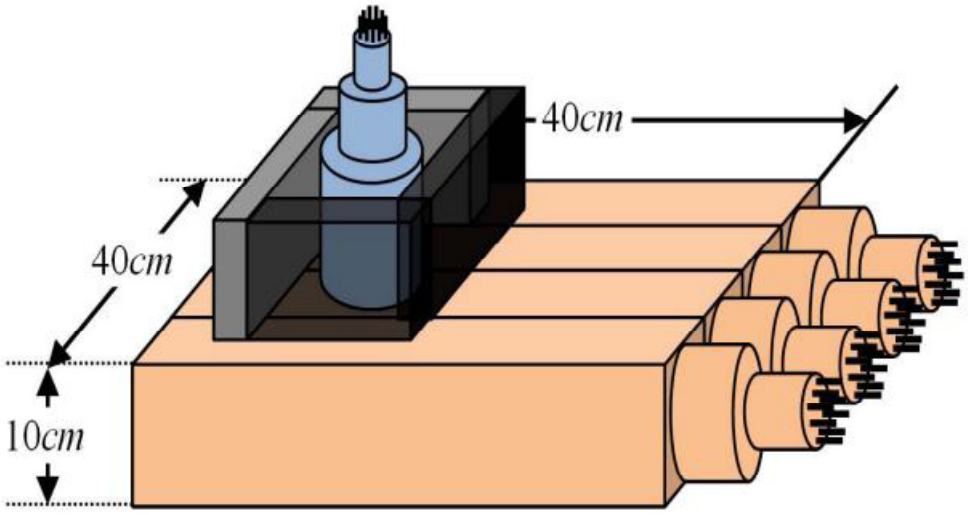

Figure 1.5 Schematic representation of the NaI(Tl) detector constituting the AGRS_16L.

Figure 1.6 The AGRS_16L mounted on the autogyro used for the airborne γ-ray survey.

1.6 Mapping radiometric data

The frequency distribution of the total activity concentration of the overall geo-dataset obtained by laboratory and airborne γ-ray measurements are shown in Figure 1.7. The map of the total activity concentration is obtained spatializating the radioactivity content measured in representative samples of the 41 CU in the SAH areas and in the airborne γ-ray surveys in the RP area. In particular, the median value of the total activity concentration for each CU is assigned to the corresponding polygons in the SAH areas [*Callegari et al.*, 2013]. For each

radionuclide (^{40}K, eU and eTh) in the RP areas, the omnidirectional Experimental Semi-Variograms (ESV) composed by 12 lags of 1 km were computed and modelled. To check the goodness of the ESV models, a cross validation procedure was used. The spatialization of the activity concentrations of ^{40}K, eU and eTh were rasterized in a 200 m × 200 m grid and used to calculate the total activity concentration.

The legend of the map was constructed following the arguments reported in [*C Reimann*, 2005]. The total activity concentrations were grouped into seven classes of percentiles, calculated on the total dataset of 19,735 records. In particular, the intervals of the classes were appropriately identified as the 5th, 20th, 50th, 80th, 95th and 100th percentiles.

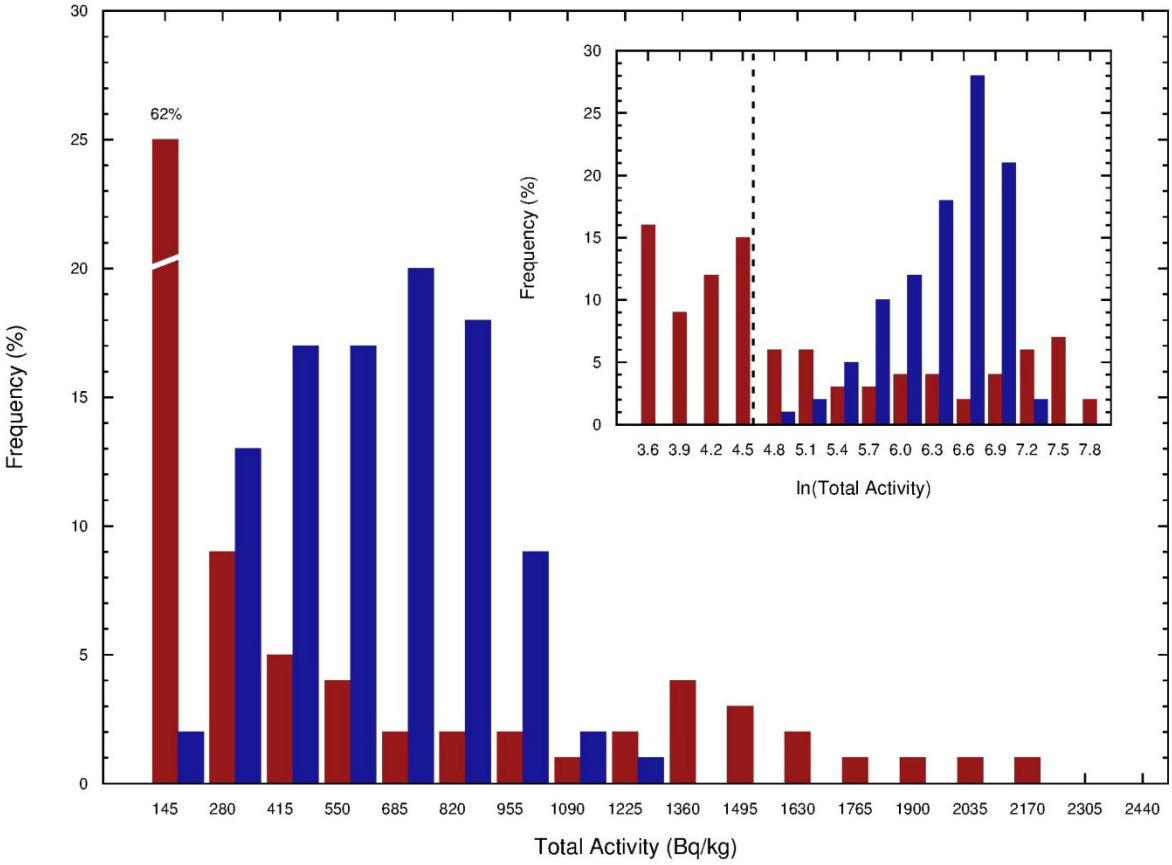

Figure 1.7 The frequency distributions of the total activity concentration in rock samples (blue) and airborne γ-ray data measurements (red). The samples on the left of the dashed line are characterized by at least one concentration of K, U and Th below the MDA.

1.7 Final remarks

We presented the first detailed investigation of the terrestrial natural radioactivity of the Veneto Region (Italy) (Annex A), obtained on the basis of γ-ray spectroscopy measurements. In particular the activity concentrations of SAH areas refer to rock reservoirs, while the radiometric data collected by AGRS surveys come from the top soil of RP areas.

Following the lithostratigraphic map at 1:250,000 scale [*Antonelli et al.*, 1990], the 41 CU of the SAH areas were characterized with respect to the total activity concentration by means of 709 measurements on rock samples performed using a HPGe γ-ray spectrometer. Over 50% of the SAH areas primarily consists of limestones and dolomites, characterized by a low total activity, often resulting in MDA values. The highest values of the total activity in the SAH areas are found in the magmatic rocks of the Euganean Hills and the Recoaro area, together with the crystalline basement.

The quaternary sediments of the RP area were investigated by means of airborne γ-ray surveys, accounting for 75 h of effective time of flight. The extended area with medium-high values of total activity concentration could be related to anthropogenic activities [*Wetterlind et al.*, 2012] and selective fluvial depositions of the main river basins. In particular, we observed that the S-E area surrounding the Euganean Hills is characterized by enrichment in the radionuclides, probably due to the erosion and transport processes undergone by magmatic rocks.

The content of this chapter is based on the following publication:

Strati V., Baldoncini M., Bezzon G. P., Broggini C., Buso G. P., Caciolli A., Callegari I., Carmignani L., Colonna T., Fiorentini G., Guastaldi E., Kaçeli Xhixha M., Mantovani F., Menegazzo R., Mou L., Rossi Alvarez C., Xhixha G. and Zanon A. *Total natural radioactivity, Veneto (Italy)*. Journal of Maps, 11(4) (2015) 543 - 551.
DOI: 10.1080/17445647.2014.923348

Chapter 2

Advanced analysis and modeling algorithms for spatial γ-ray data of Variscan Basement (Northeastern Sardinia)

The map of uranium distribution of Variscan Basement of Northeastern Sardinia comes from a very refined radiometric investigation consisting of 535 γ-ray spectroscopy measurements covering an area of approximately 2100 km^2, corresponding to 1 sample per 4 km^2. The investigated area is part of one of the largest batholiths in south-western Europe, the Corsica-Sardinia Batholith, and it represents a benchmark for the study of the Variscan magmatic processes in the Late Paleozoic.

In this study geostatistical innovations are applied for the spatial interpolation of the γ-ray measurements. The particular aspect of this survey consists in the input dataset that includes HPGe laboratory measurements and in situ measurements performed with NaI(Tl) portable detectors. Due to the features of the detectors and to the measurement methods, these two types of data are characterized by different sources of uncertainty. Indeed the in situ measurements, affected by a considerable 'noise' (e.g. geometry of the investigated area, atmospheric radon, soil moisture content, weathering) resulting in a overall uncertainty (~20%) greater than that one of the HPGe measurements (~5%), performed in laboratory under controlled conditions. Thanks to technological development affecting a lot of experimental fields, e.g. mineral exploration [*Deraisme and Strydom*, 2009], spatial data are more frequently gathered using different measurement instruments with different properties. For this reason, the questions arise on how to treat this heterogeneous data in the spatial interpolation and producing reliable estimate are a matter of interest for the world geostatistical community.

I took the lead in the analysis of the data focusing on the treatment of both input and output uncertainties. In particular I handled this specific aspect by applying the method of Kriging with Variance of Measurements Error to combine gamma ray data collected with these two γ-ray techniques, characterized by different overall uncertainties. During the estimation process difference weights are assigned on the base of the degree of confidence associated to the measurements. Moreover the use of this geostatistical method implied a rigorous study of the data distributions considering normal and lognormal probability density functions together with chi squares. This refined analysis led to the realization of an original cartographic product that includes the uranium distribution map together with the uncertainties of the estimates. In particular it stimulated a focus in the area of Arzachena pluton where the link between uranium abundances and petrological associations was correlated to the behavior of this element during the magmatic processes.

Besides having a strong potential scientific impact (e.g. radiogenic heat flux and geoneutrino science) and societal benefits (i.e. Radon risk mapping) the uranium distribution map represents a useful support for further studies regarding the main geophysical, geochemical and geodynamic processes which affect the continental crust as well as for the investigation of Radon-prone areas

2.1 Background

The Variscan Basement of Northeastern Sardinia (VBNS) is a benchmark for the study of 'hot' collisional chains characterized by a high temperature-low pressure (HT-LP) gradient. Several processes might have enhanced the Variscan geotherm, such as i) shear heating [*Casini et al.*, 2015a; *Maino et al.*, 2015], ii) the advection of hot, mantle-derived melts, iii) the break-off of the mantle lithosphere [*X-H Li et al.*, 2014] or iv) the selective enrichment of radiogenic heat-producing elements, such as U, Th and K, in the crust [*Lexa et al.*, 2011]. The widespread late-Variscan magmatism in the Corsica-Sardinia Batholith (C-SB) has been occasionally explained in terms of enhanced radiogenic heating. The models that describe the efficiency of the processes depend strongly on the uranium content of the fertile crust [*Bea*, 2012]. The heterogeneous distribution of uranium throughout the VBNS might be a proxy for investigating the applicability of thermal models based on the selective enrichment of radiogenic elements in the crust [*Mohamud et al.*, 2015] [*Tartèse et al.*, 2011]. In addition, the outcrops in VBNS are the most accessible intrusive bodies for studying the geoneutrino signal in the Borexino experiment [*Borexino Collaboration*, 2015], which is particularly sensitive to the U and Th contents and distributions in the Variscan continental crust [*Coltorti et al.*, 2011].

Finally, this study has implications related to the public health, as recent investigations [*Bochicchio et al.*, 2005] showed that the Sardinia region is characterized by high values of radon gas, monitored in 124 dwellings. Since for good bedrock exposure, as in the case of VBNS, the correlation between indoor radon concentrations and uranium content of the underlying rocks increases, the results of this study potentially constitute a baseline for future mapping of radon-prone areas.

We present a map (Annex B) of the eU distribution (this notation indicates equivalent uranium, as we assume secular equilibrium in the ^{238}U decay chain) in the VBNS at a scale of 1:100,000 as support for further studies regarding the main geophysical, geochemical and geodynamic features of the continental crust in this region. This study is included in the framework of a research project which has already led to the realization of the total natural radioactivity map of the Tuscany region [*Callegari et al.*, 2013] and Veneto region [*Strati et al.*, 2015] (see Chapter 1).

The spatial model, together with its uncertainties, was obtained using the Kriging with Variance of Measurement Error method for 535 gamma-ray spectrometry measurements. The eU distribution is discussed in the geodynamic framework proposed by [*Casini et al.*, 2015a],

taking into account the petrological features of the C-SB, the compositional variation and the emplacement timing of Variscan granitoids. Finally, we focus on the eU distribution measured in the granitoids of the Arzachena pluton, linking it to the emplacement mechanism proposed in [*Casini et al.*, 2012].

2.2 Geological setting

The Variscan belt of Western Europe resulted from the collision of Northern Gondwana and Laurussia in a time interval spanning from the Late Devonian to the Early Permian (~380-270 Ma). The European Variscan crust, including the Corsica-Sardinia massif, experienced several episodes of plutonic and volcanic activity with different petrochemical affinities [*Finger et al.*, 1997] [*Corsini and Rolland*, 2009].

The C-SB, with its ca. 12,000 km^2 area, constitutes one of the largest batholiths in south-western Europe, emplaced in approximately 40 Ma (Late Mississippian Pennsylvanian-Early Permian). Three main magmatic suites can be recognized: a magnesium-potassium complex exposed only in northern Corsica, a peraluminous calc-alkaline complex [*Casini et al.*, 2012] [*Rossi and Cocherie*, 1991] and finally, a late to post-orogenic alkaline suite in the VBNS [*Bonin*, 2007]. The 2,100 km^2 of the VBNS (Figure 2.1) are characterized by several calc-alkaline plutons and a few minor alkaline complexes emplaced within migmatites and amphibolite-facies of metamorphic rocks [*Casini et al.*, 2015b]. According to [*Cruciani et al.*, 2013], the migmatites outcropping in the study area are related to high-pressure metamorphism occurred in the Internal Nappes of the Sardinia Variscides at the age of the initial continent–continent collision.

Both migmatites and the calc-alkaline plutons have been interpreted in terms of extensive crustal melting related to the establishment of an anomalous thermal gradient [*Anderson*, 2006]. One of the main contributions to the high geothermal gradient, which is required to induce anatexis processes, originates from the enrichment of radiogenic heat-producing elements caused by several genetic processes, such as subduction of continental crust, crust-scale migmatization [*X-H Li et al.*, 2014], melt dehydration and segregation [*Gerdes et al.*, 2000]. Understanding heat production and transfer mechanisms is relevant for modeling thermal-kinematic and exhumation processes [*Lexa et al.*, 2011].

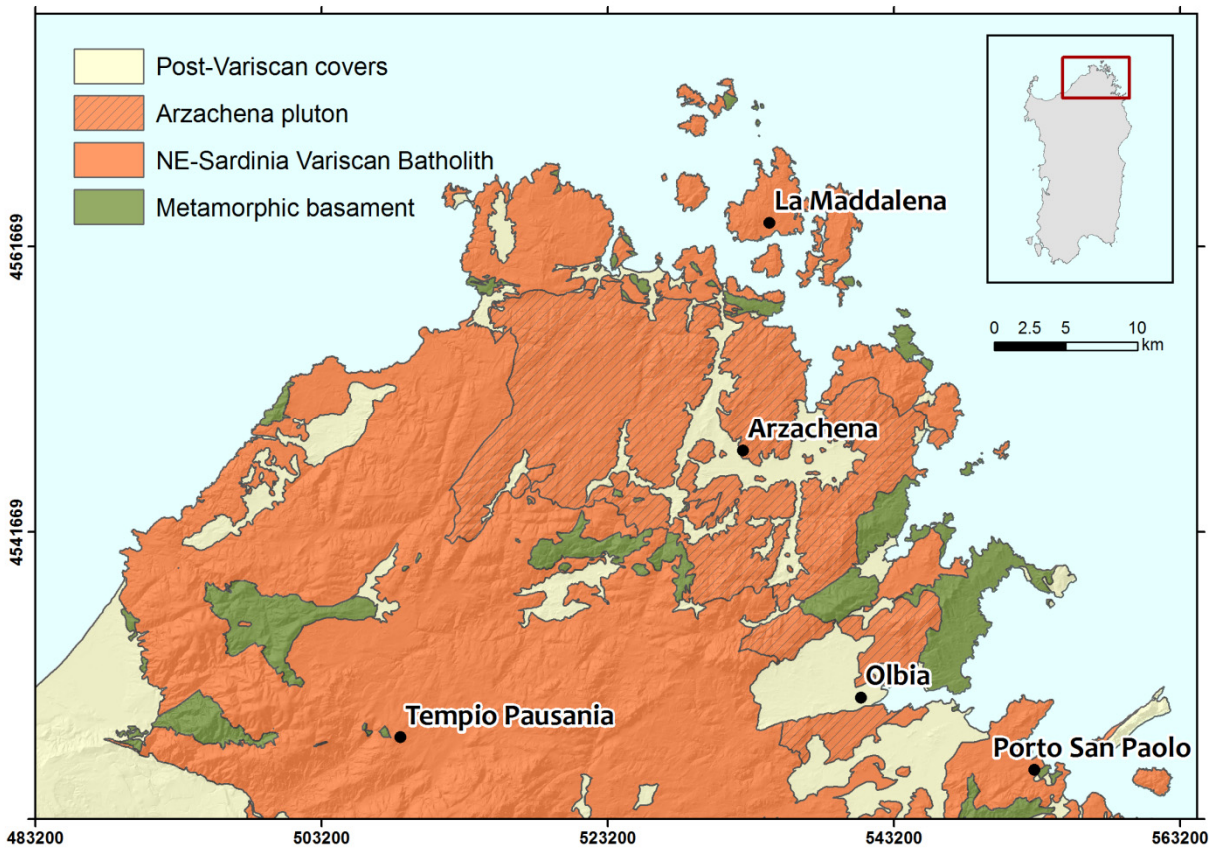

Figure 2.1 Geological sketch map of the VBSN (cartographic reference system WGS84 UTM ZONE 32N), modified from [*Casini et al.*, 2015b] **.**

2.3 Methods

The 535 input data points used for producing the Main Map come from 167 rock sample measurements and 368 *in situ* measurements. The surveys were planned based on the Geological map of Sardinia at a scale of 1:200,000 [*Barca et al.*, 1996] and the structural map of Variscan Northern Sardinia at a scale of 1:100,000 [*Casini et al.*, 2015b].

The eU abundances in the rock samples collected from fresh outcrops (Figure 2.2) were measured using the MCA-Rad system (see section 1.4).

In this survey, a total of 368 *in situ* gamma-ray measurements were performed on granitic outcrops using a portable NaI(Tl) detector mounted in a backpack to allow flexible operation (Figure 2.3), with an acquisition live time of 300 seconds. The NaI(Tl) detector is of a cubic shape (10.2 cm × 10.2 cm × 10.2 cm) and has an energy resolution of 7.3 % at 662 keV(^{137}Cs) and 5.2% at 1,172 and 1,332 keV (^{60}Co). The instrument was calibrated following the method of Full Spectrum Analysis with the Non-Negative Least Squares (FSA-NNLS) constraint, as described in [*Caciolli et al.*, 2012]. According to the FSA-NNLS method, each spectrum was reconstructed from a linear combination of standard spectra for ^{238}U, ^{232}Th, ^{40}K, ^{137}Cs and for the background. The uncertainty of the method is estimated to be 5 % for ^{40}K and 7 % for ^{232}Th, with relatively higher uncertainty for ^{238}U of approximately 15%. In [*Caciolli et al.*, 2012], the coefficient of correlation (0.87 ± 0.12) between the eU values obtained by NaI(Tl) and HPGe is compatible with the unity at the 1 sigma level. Despite this

strong agreement between the two acquisition methods, it is well known [*IAEA*, 2003] that in situ gamma ray measurements are susceptible to many sources of 'noise': the geometry of the investigated area, the presence of atmospheric radon, the soil moisture content, the weathering and the outcrop exposure can affect the gamma signal, decreasing the precision of the survey.

Because in our study we include the field measurements, relevant precautions were taken to ensure the reliability of our data. Indeed, we avoided acquiring data immediately after rainfall and preferred flat outcrops far from man-made constructions (Figure 2.3).

In the U decay chain, disequilibrium occurs when one or more isotopes are completely or partially removed or added to the system. Because gamma ray spectroscopy is a method that detects the gamma emitter daughters of uranium, secular equilibrium of the decay chains is commonly assumed and is reported as the equivalent uranium (eU).

Figure 2.2 Collection of fresh rock sample from representative outcrop.

Figure 2.3 Field measurements using the portable NaI(Tl) detector**.**

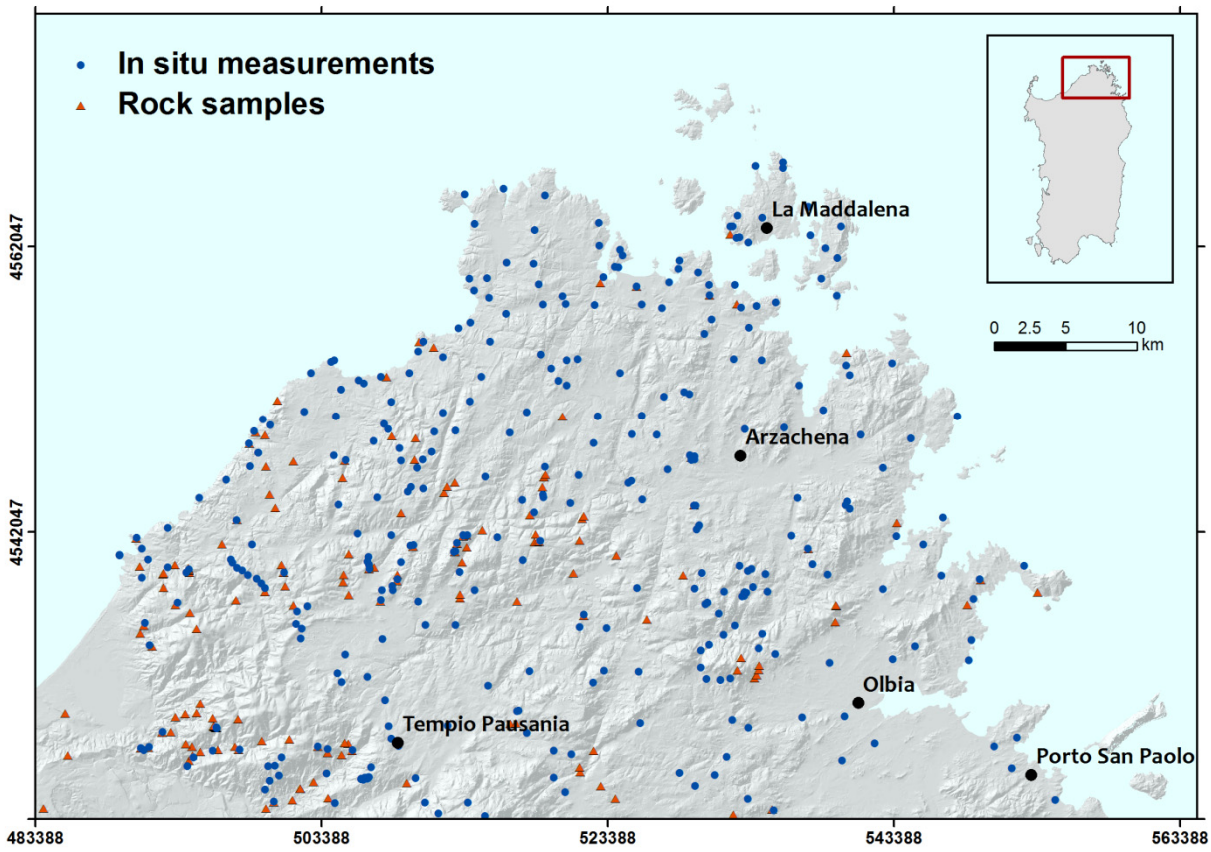

Figure 2.4 The locations of the 167 collected rock samples and the 368 in situ measurements (cartographic reference system WGS 84 UTM 32N).

2.4 Mapping radiometric data

The map of the eU distribution in VBNS, a raster with a 100 m × 100 m spatial resolution, was obtained using all 535 measurements acquired by HPGe and NaI(Tl) using the Kriging method (Figure 2.4). The frequency distribution and the principal statistical parameters of the input data are reported in Figure 2.5.

The exploratory statistics analysis highlights that the HPGe and NaI(Tl) data are characterized by frequency distributions (Figure 2.6) described by the statistical parameters reported in Table 2.1. The chi-squared test was performed to evaluate the goodness of fit for HPGe data, NaI(Tl) data and for the whole dataset. In Table 2.1 are reported the values of the normalized chi-square calculated as follows:

$$\chi^2 = \frac{1}{\nu}\sum_{i=1}^{k}\frac{(O_i - E_i)^2}{E_i}$$

where ν is the number of the degrees of freedom, k is the number of bins calculated according the Sturges' rule (given N the number of samples, $k = 1 + \log_2 N$), O_i is the observed frequency for bin i and E_i is the expected frequency for bin i calculated by:

$$E_i = F(x_2) - F(x_1)$$

where F is the cumulative distribution function being tested (normal or lognormal), and x_1, x_2 are the limits for bin i.

The distributions are affected by a sampling bias because each lithology was not investigated by the same amount of records in the two datasets: this is particularly clear in observing the tails of the distributions. In fact, the quartzites and amphibolites of the metamorphic basement are characterized by the lowest uranium concentrations (< 2 μg/g) and were mainly investigated with HPGe measurements because they are badly exposed and poorly suitable for in situ measurements. In contrast, the highest values in Figure 2.6 are found in the U-rich monzogranites (~ 9 μg/g) of the La Maddalena pluton [*Casini et al.*, 2015b], investigated mostly with in situ surveys.

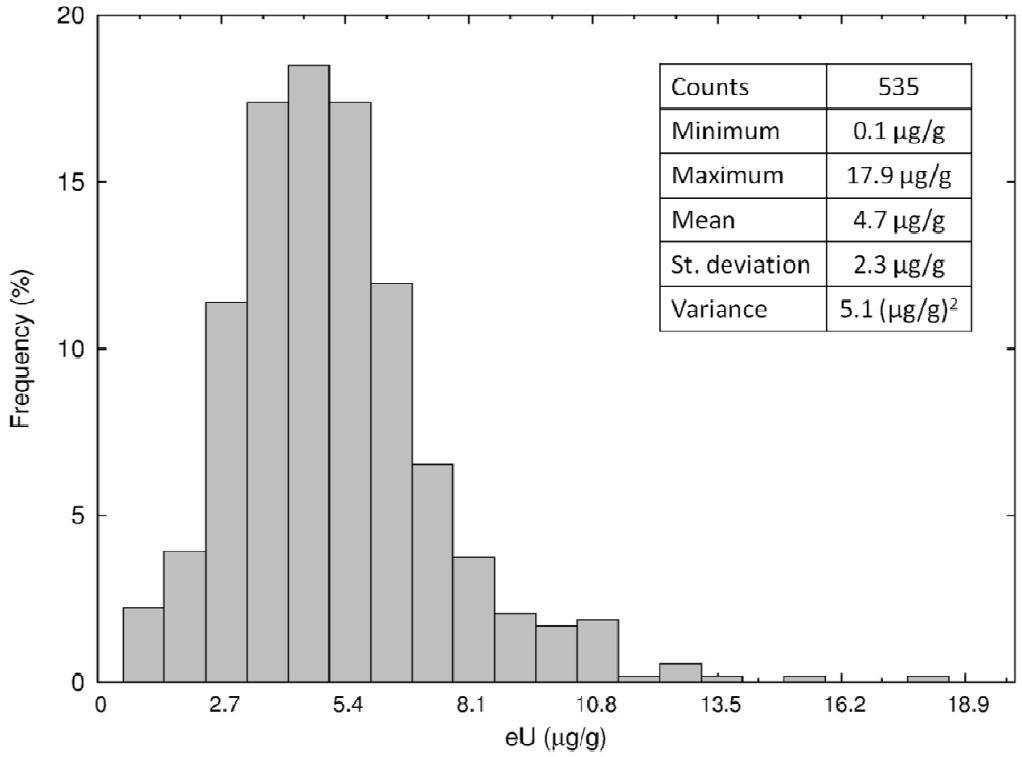

Figure 2.5 Frequency distribution and main statistical parameters of the input dataset**.**

Since the distribution of the input data shows a skewness value close to unity, the study of the spatial variability was performed without any normal transformation of the uranium abundances. The analysis of the directional Experimental Semi-Variograms (ESV) highlighted an isotropic experimental variability without any preferred directions. Therefore, an omnidirectional ESV made up of 9 lags of 2.2 km was computed and modeled using a trial-and-error procedure (Figure 2.7). The ESV was fitted using a nugget effect model and two spherical models. The value γ of the model at the distance *h* is described by the following system of functions:

$$\begin{cases} \gamma(h) = c_0 + c_1\left[\frac{3h}{2a_1} - \frac{1}{2}\left(\frac{h}{a_1}\right)^3\right] + c_2\left[\frac{3h}{2a_2} - \frac{1}{2}\left(\frac{h}{a_2}\right)^3\right] & for \quad h < a_1 \\ \gamma(h) = c_0 + c_1 + c_2\left[\frac{3h}{2a_2} - \frac{1}{2}\left(\frac{h}{a_2}\right)^3\right] & for \quad 0 \le h < a_1 \\ \gamma(h) = c_0 + c_1 + c_2 & for \quad h > a_2 \end{cases}$$

where the parameters c_0 is the nugget effect, a_1 and a_2 are the ranges of the first and second spherical model respectively, c_1 and c_2 are the sills of the first and the second spherical model respectively (Table 2.2). Since we are interested in small scale variability of U abundances, the parameters used for the ESV modeling were tuned for optimizing the fit in the first lags of the ESV. The nugget effect (1.7 $\mu g^2/g^2$), contributing approximately to 30% of the total amount of spatial variability, and the maximum distance of spatial variability equal to 4.8 km are in excellent agreement with the observed tendency of the experimental data. The goodness of fit of the ESV model was checked via a cross-validation procedure. The results are reported in Table 2.2, together with the parameter of the structures of variability used for the ESV modeling.

Table 2.1 Uranium average abundance U (μg/g), standard deviation σ (μg/g) and goodness of fit (normalized χ2) obtained with normal and lognormal probability density functions applied to all data and both datasets (i.e., HPGe and NaI(Tl)).

Dataset	Number of records	Normal distribution		Lognormal distribution	
		U ± σ (μg/g)	χ^2	U ± σ (μg/g)	χ^2
HpGe	167	3.5 ± 1.9	1.7	$2.9^{+3.3}_{-1.5}$	4.3
NaI(Tl)	368	5.2 ± 2.2	6.0	$4.8^{+2.4}_{-1.6}$	0.5
All data	535	4.7 ± 2.3	4.5	$4.1^{+3.3}_{-1.8}$	6.1

The estimation process, performed with Geovariances ISATIS® software, takes into account the overall uncertainties of the two methods of gamma-ray measurements as the known Variance of Measurements Error of the input data. In particular, we considered an overall uncertainty of 5% for each HPGe measurement and a conservative uncertainty of 20% in the case of the NaI(Tl) measurements. This methodology, known as Kriging with Variance of Measurement Error, allows for assigning different weights to the input considering the degree of confidence of the measurements, thus improving the quality of the estimations [*Deraisme and Strydom*, 2009]. The accuracy of the spatial model in terms of the variance normalized with respect to the estimated values is reported in the Main Map (Annex B) with the contour lines.

The frequency distribution and the main statistical parameters of the output model are reported in Figure 2.8. The chromatic variations in the color ramp of the legend were assigned to specific values of eU concentration. In particular, they correspond to the 20th, 35th, 45th, 55th, 65th, 75th and 80th percentiles calculated for the entire dataset of 535 measurements.

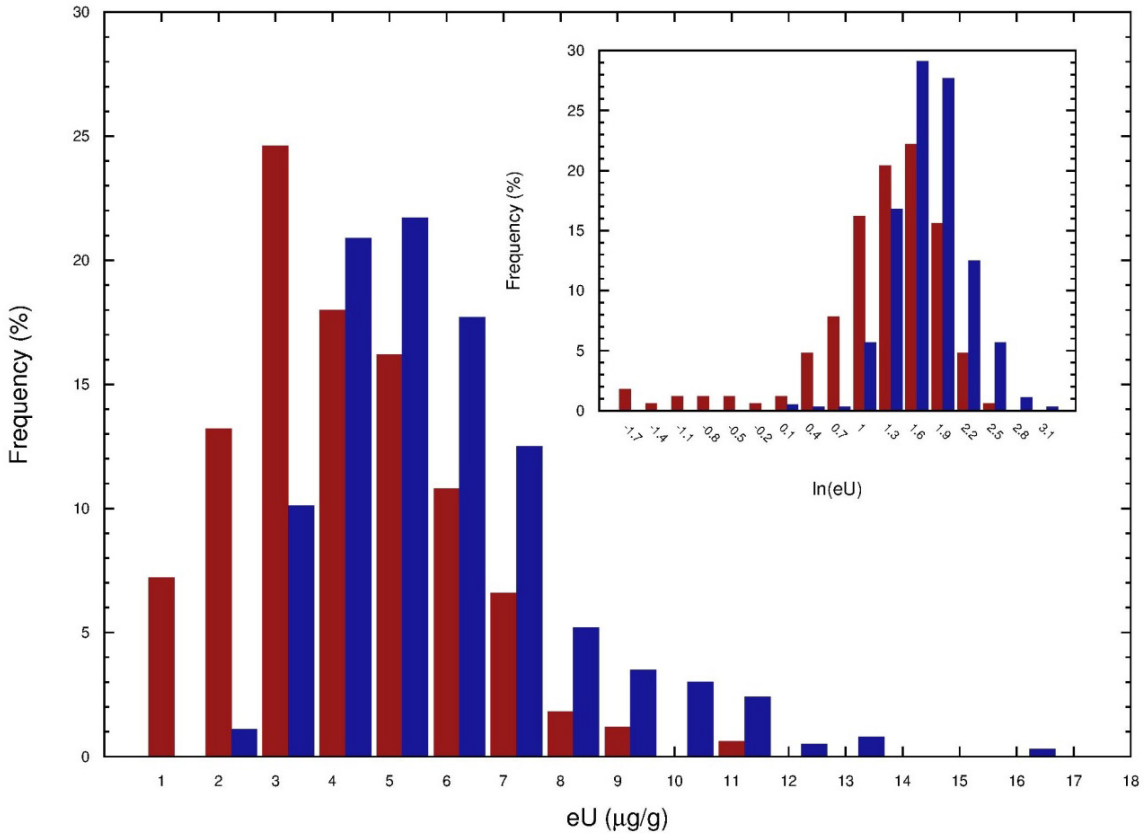

Figure 2.6 The frequency distributions of the eU abundances (µg/g) in rock samples (red) and in situ measurements (blue).

Table 2.2 Parameters of the structures of variability used for the model fitted on the ESV; results of the cross-validation procedure in terms of the Mean of Standardized Errors (MSE) and the Variance of Standardized Errors (VSE).

ESV model parameters			**Cross-validation results**	
Structures of variability	**Range (km)**	**Sill (µg/g)^2**	**MSE**	**VSE**
Nugget effect model	-	1.7	-0.04	0.74
First Spherical model	3.4	2.4		
Second spherical model	13.8	0.8		

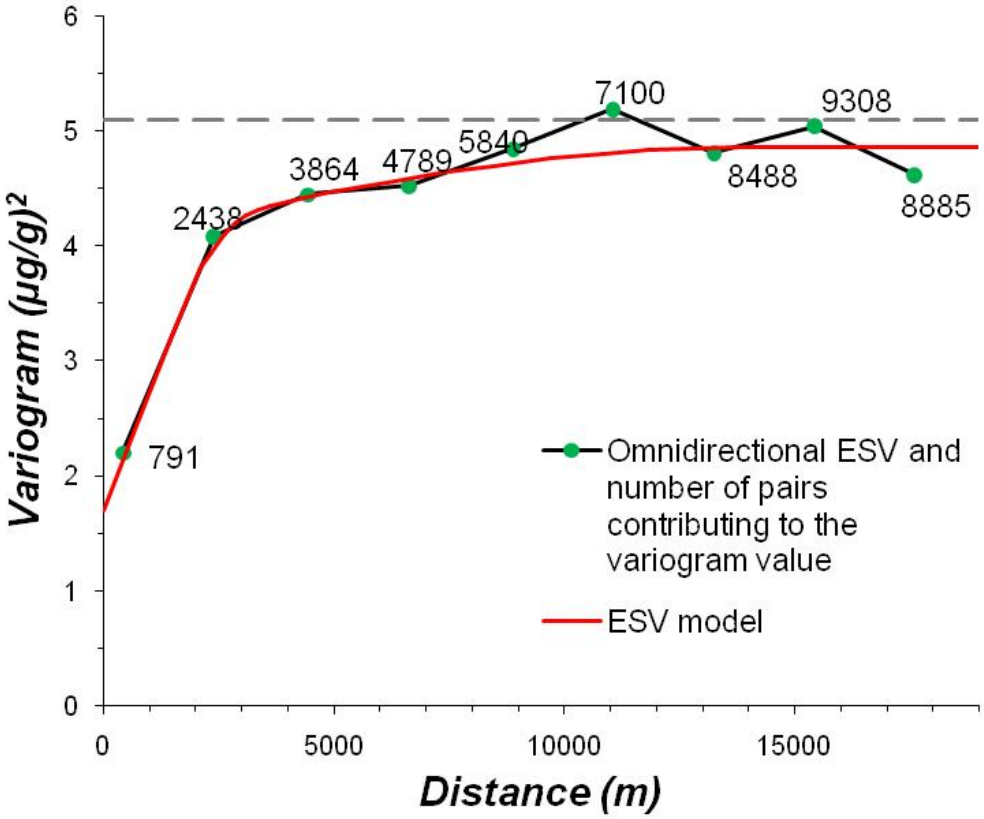

Figure 2.7 Model fitted for the ESV calculated with 9 lags of 2.2 km.

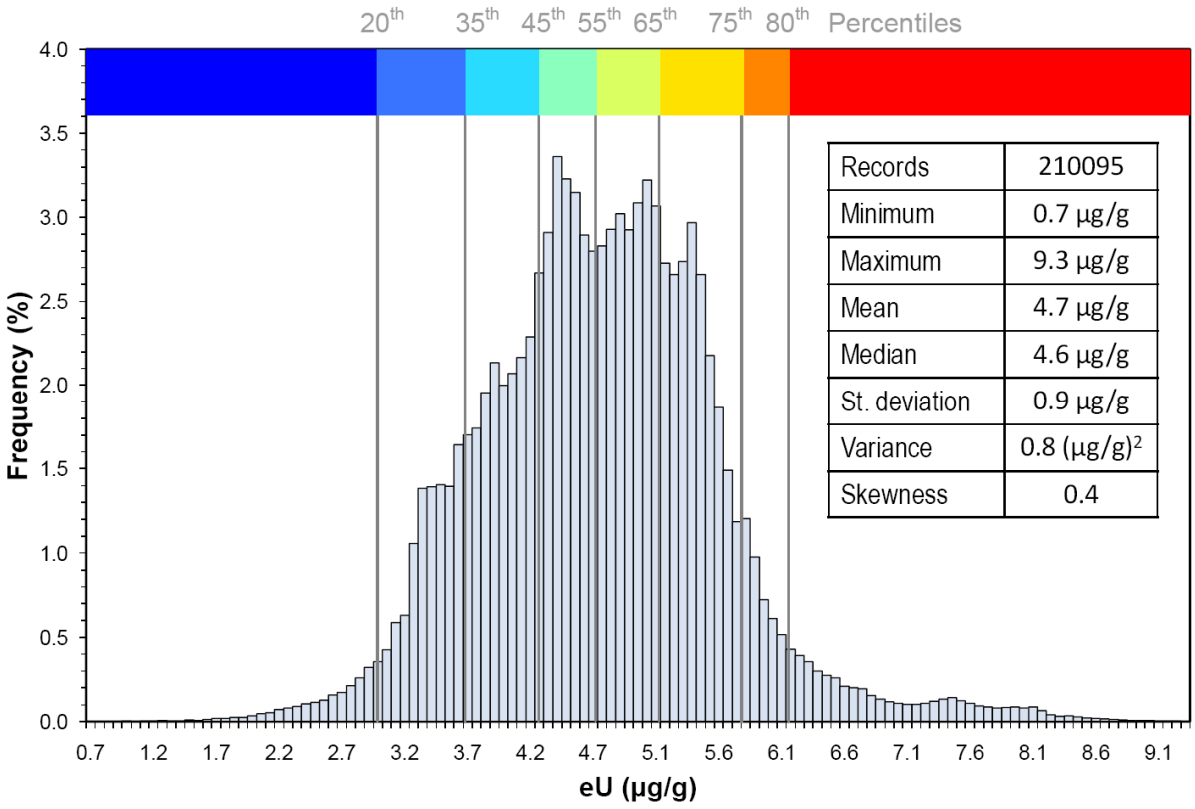

Figure 2.8 Frequency distribution of the output model and main statistical parameters, where the 210095 records correspond to the number of the pixels of 100 m resolution.

2.5 The Arzachena pluton

In this section, we present a specific focus on the eU distribution in the Arzachena pluton (AZN), a reference calc-alkaline massif of the VBNS.

The AZN is an elongated pluton that consists of three concentric granitic shells [*Oggiano et al.*, 2005]. The pluton shows reverse zonation: the more mafic terms (medium-grained granodiorite) are exposed in the core, along the southern margin of the pluton, whereas the external part is composed of felsic rocks, such as porphyritic biotite–monzogranite and fine-grained leuco-monzogranites. This last type of rock represents the more evolved magmatic products and is mainly localized in the peripheral zone of the pluton, exposed to the north [*Casini et al.*, 2012].

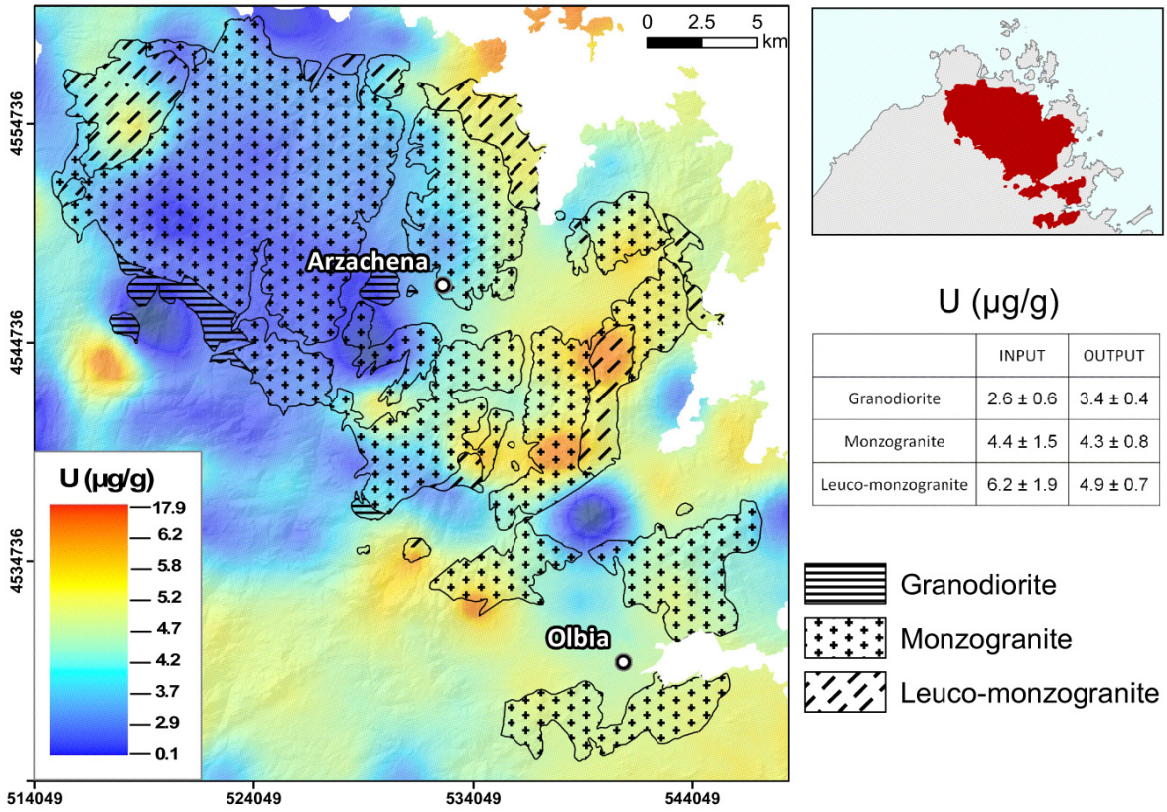

Figure 2.9 The eU distribution map in the Arzachena pluton with the cartographic boundaries of the three different magmatic bodies. The mean and 1σ uncertainty of eU abundances of the input data and the output model are reported for each petrological association (cartographic reference system WGS84 UTM ZONE 32N).

In Figure 2.9, we use the cartographic boundaries of the three granitic shells to distinguish and analyze the range of eU concentrations of the different petrological associations related to the magmatic differentiation during magma emplacement. The mean and 1σ uncertainty of the input data and of the spatial model are reported for the three rock types. The granodiorites are characterized by lower eU concentrations (3.4 ± 0.4 µg/g). Monzogranites and leuco-monzogranites are enriched in eU content, with average values of 4.3 ± 0.8 µg/g and 4.9 ± 0.7 µg/g, respectively. This distribution defines a clear geochemical trend characterized by eU values that increase in felsic rocks. The eU distribution within the

AZN supports a strong positive correlation between the presence of U-bearing accessory minerals (e.g., zircons, monazite and xenotime) and the evolution of magmatic systems [*Pérez-Soba et al.*, 2014]. Indeed, melting processes and melt extraction remove a large amount of radioactive elements from the magmatic system that are hosted by accessory minerals in which uranium can substitute other cations with a similar ionic radius and occasionally equal valences (e.g., Ca, trivalent REE, Zr and Y) [*Mohamud et al.*, 2015] [*Pagel*, 1982] [*Peiffert et al.*, 1996].

These results confirm the conceptual model proposed in [*Casini et al.*, 2012], which explains the distribution of Large-Ion Lithophile Elements (LILE) within AZN in terms of in situ progressive differentiation of anatectic melts sourced from a compositionally heterogeneous lower crust. The obtained eU distribution in the AZN agrees with the emplacement history and the pluton evolution described in the proposed termo-mechanical model.

2.6 Final remarks

In this study, we present a 1:100,000 scale map of the eU abundance distribution in the Variscan Basement (Annex B), which occupies a total area of 2100 km^2 in Northeastern Sardinia. The spatial model obtained performing Kriging on the 535 gamma-ray measurements is reported together with the uncertainties of the estimations.

Following a detailed statistical analysis performed on the input dataset consisting of 167 laboratory measurements (HPGe) and 368 in situ measurements (NaI(Tl)), the spatial variability of the eU abundance was studied with the computation and modeling of an omnidirectional ESV (9 lags of 2.2 km). The map was obtained using the Kriging with Variance of Measurement Error method, a geostatistical tool that allows for combining eU abundances with different levels of confidence associated with the two different gamma-ray spectroscopy methods.

The map shows the highest values in the granitoids of the La Maddalena pluton, where the eU content ranges between 6.2 and 9.3 μg/g. However, in the metamorphic basement, outcropping in the southwest of the study area (Figure 2.1), the presence of eclogites intruded in the migmatitic orthogneisses contributes to the lowest uranium abundances (< 2 μg/g).

We suggest that the distribution of the eU content is related to the Post-Variscan brittle structure, reported in [*Casini et al.*, 2015b], that affects the metamorphic units and the plutons of the VBNS. In particular, in the Tempio Pausania pluton (southwest of the study area), the major NE-SW faults correspond to anomalies in the eU distribution and mark an area with higher eU content (5 - 7 μg/g) compared to the adjacent sectors of the pluton with lower eU content (~ 3.5 μg/g).

In the AZN, the eU content increases in the more differentiated rocks. This behavior can be verified in the spatial model, even if the ranges of the estimated values for granodiorites, monzogranites and leuco-monzogranites are affected by the 'smoothing effect' typically associated with the Kriging method.

The presented map, integrated with available and more detailed geological maps, is a useful tool for studying the assembly of the intruded plutons and the relationships between the different petrological associations, based on the eU behavior during crustal magmatic processes. Indeed, the study of the eU distribution in the VBNS, particularly in the AZN, could help to refine existing models explaining the post-collisional magmatic processes of the southern European Variscides.

We emphasize that about 90% of the territory of the VBNS is characterized by eU concentrations higher than the average upper continental crust abundance (2.7 μg/g) [*Rudnick and Gao*, 2003]. Since uranium rich rocks are generally the main source of radon, the presented distribution is a primary criterion for identifying radon-prone areas. Although radon migration depends on many geophysical parameters (e.g. porosity, fractures and permeability of rocks), the assessment of radon gas emission from the underlying bedrock is strongly recommended for mapping the Radon risk, which could be relevant in the coastal areas where the tourism enhances the population density especially in the summer.

The content of this chapter is based on the following publication:

Kaçeli Xhixha M., Albèri M., Baldoncini M., Bezzon G. P., Broggini C., Buso G.P., Callegari I., Casini L., Cuccuru S., Fiorentini G., Guastaldi E., Mantovani F., Mou L., Oggiano G., Puccini A., Rossi Alvarez C., Strati V., Xhixha G. and Zanon A. *Uranium distribution in the Variscan Basement of Northeastern Sardinia*. Journal of Maps, (2015) 1-8.
DOI: 10.1080/17445647.2015.1115784

Chapter 3

A multivariate spatial interpolation of airborne γ-ray data using the geological map as constraining variable

Taking advantage of the correlation existing between two or more variables, the goal of a multivariate analysis is the improvement of the estimation of one under-sampled variable on the base of a well-sampled variable. However, sometimes primary and ancillary variables are sampled by different supports, measured on different scales, and organized in different sampling schemes, which makes the realization of a single optimized prediction model more difficult. In this framework the collocated cokriging technique was recently introduced to facilitate the integration process and it was demonstrated as the cokriging estimates at one point can be obtained enhancing the kriging estimates with the collocated secondary data [*Doyen et al.*, 2013]. This approach is also used for mapping soil organic matter [*Pei et al.*, 2010], rainfall, or temperature over a territory [*Goovaerts*, 1997; *Hudson and Wackernagel*, 1994]; ground based radiometry data [*Atkinson et al.*, 1992]; estimating environmental variables, such as pollutants or water tables [*Desbarats et al.*, 2002]; and mapping geogenic radon gas in soil [*Buttafuoco et al.*, 2009]. However, the use of the continue information included in a geological map as secondary variable is poorly explored and moreover some specific questions arise. How to consider qualitative information of the geological map as a quantitative constraining variable? How to assign the progressive number to the geological variables? Does the frequency distribution of the secondary variable affect the final results?

This Chapter concerns a study case of remote sensing of environmental radioactivity achieved through the same experimental setup used in the extensive survey in the Veneto region (see Chapter 1). The target area is the Elba island, an island of 224 km^2 in Tuscany (Italy), characterized from the geological point of view by a high lithologic variability and at the same time by an excellent exposure of outcropping rocks. For the first time the collocated cokriging (CCoK) is applied as a multivariate estimation method for interpolating the natural abundances of K, eU, or eTh measured via airborne γ-ray spectrometry whereas the secondary variable refers to the continuous distribution of the geological formations, i.e. the geological map at 1:10000 scale. I took part in the geostatistical analysis and in the realizations of the radiometric maps as well as in the discussions arisen from the interpretation of the results here reported. After studying the spatial autocorrelation among the two variables, I faced the practical problems related to the application of the CCoK described previously and I participated to the tests performed in order to verify the non-dependency of the estimated results from the random numbering of the geological formations. The radiometric maps

showed as the internal variability of the radiometric data is not biased by the multivariate interpolation, as demonstrated by the evidences and anomalies observed and confirmed also in literature by published studies performed in the study area.

3.1 Background

Airborne γ-ray spectrometry (AGRS) is a fruitful method for mapping natural radioactivity, both in geoscience studies and for purposes of emergency response. One of the principal advantages of AGRS is that it is highly appropriate for large scale geological and environmental surveys [*Bierwirth and Brodie*, 2008; *Minty*, 2011; *Rybach et al.*, 2001; *Sanderson et al.*, 2004]. For fixed conditions of flight a challenge is to increase the amount of geological information, developing dedicated algorithms for data analysis and spatial interpolation. The full spectrum analysis (FSA) with the non-negative least squares (NNLS) constraint [*Caciolli et al.*, 2012] and noise-adjusted singular value decomposition (NASVD) analysis [*Minty and McFadden*, 1998] introduces notable results oriented to improve the quality of the radiometric data. On the other hand, the multivariate interpolation has the great potential to combine γ-ray data with the preexisting information contained in geological maps for capturing the geological local variability.

The Elba Island (Italy) is a suitable site for testing a multivariate interpolation applied to AGRS data because of its high lithological variability, excellent exposure of outcropping rocks and detailed geological map. In this study the collocated cokriging (CCoK) was used in a non-conventional way for dealing with the primary (AGRS data) and secondary (geological data) variables when the variable of interest was sampled at a few locations and the secondary variable was extensively sampled. Using this approach, the maps of natural radioactivity of Elba Island were obtained.

3.2 Geological setting

Elba is the biggest island of the Tuscan Archipelago and is located in the northern part of the Tyrrhenian Sea, between Italy and Corsica Island (France). It is one of the westernmost outcrop of the Northern Apennines mountain chain (Figure 3.1).

The geological distinctive features of this island are linked to its complex stack of tectonic units and the well-known Fe-rich ores, as well as the well-exposed interactions between Neogene magmatic intrusions and tectonics [*Dini et al.*, 2002b; *Musumeci and Vaselli*, 2012]. The structure of Elba Island consists of thrust sheets stacked during the late Oligocene to middle Miocene northern Apennines deformation. Thrust sheets are cross-cut by late Miocene extensional faults [*Keller and Coward*, 1996; *Smith et al.*, 2010].

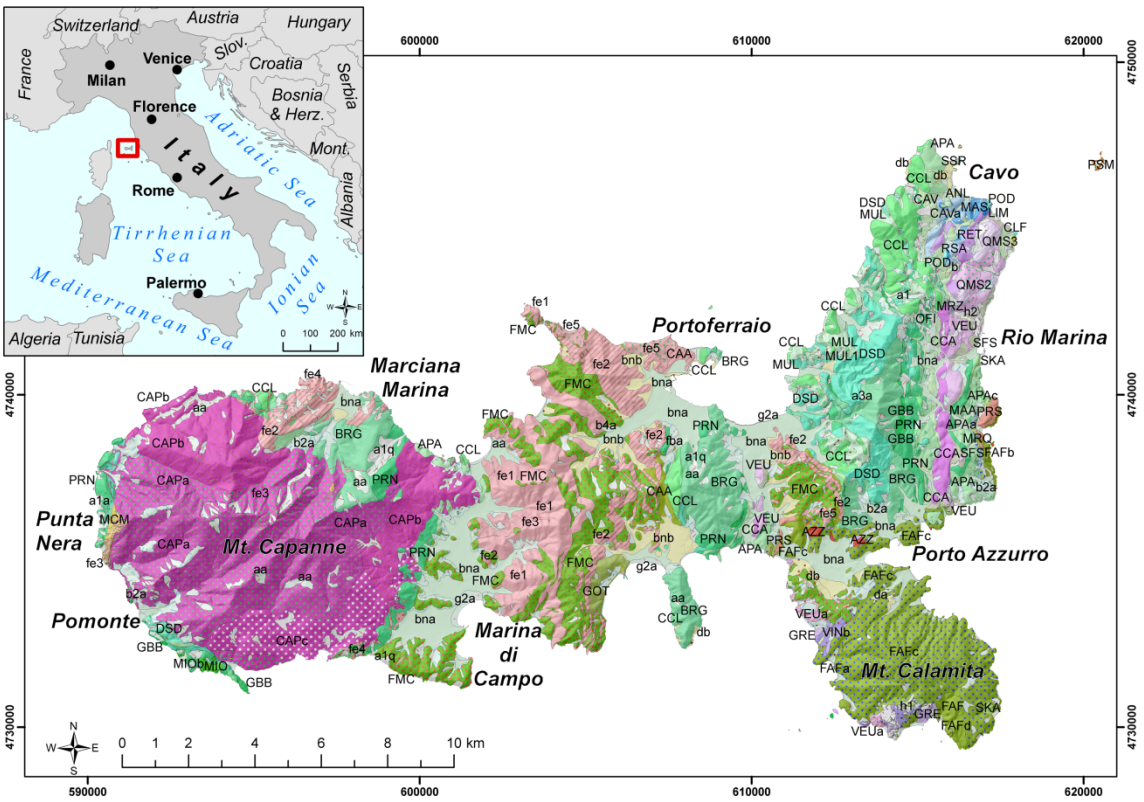

Figure 3.1 Geological map of Elba Island [*CGT*, 2011]: the western sector is mainly characterized by intrusive igneous rocks (magenta), the central and eastern sectors are characterized by a wide lithological variation (green, purple, and pink), while the southeastern outcrop is constituted almost exclusively of metamorphic rocks (Mt. Calamita). For the legend of the geologic map, see http://www.geologiatoscana.unisi.it.

The tectonics of Elba Island is composed of a structural pile of five main units called by [*Trevisan*, 1950] as “Complexes" and hereafter called "Complexes of Trevisan” (TC): the lowermost three belong to the Tuscan Domain, whereas the uppermost two are related to the Ligurian Domain. [*Bortolotti et al.*, 2001] performed 1:10,000 mapping of central-eastern Elba and proposed a new stratigraphic and tectonic model in which the five TC were reinterpreted and renamed. TCs are shortly described below.

The Porto Azzurro Unit (TC I) (Mt. Calamita Unit Auct.) consists of Paleozoic micaschists, phyllites, and quartzites with local amphibolitic horizons, as well as Triassic-Hettangian metasiliciclastics and metacarbonates. Recently [*Musumeci et al.*, 2011] point out Early Carboniferous age for the Calamita Schist by means of U-Pb and ^{40}Ar-^{39}Ar radioisotopic data. In particular, in the Porto Azzurro area and the eastern side of Mt. Calamita, the micaschists are typically crosscut by the aplitic and microgranitic dykes that swarm from La Serra-Porto Azzurro monzogranitic pluton (5.1-6.2 Ma, [*Dini et al.*, 2002a] and references therein). Magnetic activities produced thermometamorphic imprints in the host rocks [*Garfagnoli et al.*, 2004; *Musumeci and Vaselli*, 2012].

The Ortano Unit (lower part of TC II) includes metavolcanics, metasandstone, white quartzites and minor phyllites. The Acquadolce Unit (upper part of TC II) is composed of locally dolomitic massive marbles, grading upwards to calcschists [*Pandeli et al.*, 2001]. This lithology is capped by a thick siliciclastic succession. Ortano and Acquadolce units

experienced late Miocene contact metamorphism under low to medium metamorphic grade conditions [*Duranti et al.*, 1992; *Musumeci and Vaselli*, 2012].

The Monticiano-Roccastrada Unit (lower part of TC III) includes basal fossiliferous graphitic metasediments of the Late Carboniferous-Early Permian, unconformably overlain by the detrital Verrucano succession (Middle-Late Triassic) [*Bortolotti et al.*, 2001]. The Tuscan Nappe Unit (central part of TC III) is represented by calcareous-dolomitic breccias and overlying carbonatic outcrops northwards. Most of Grassera Unit (upper part of TC III) is composed of varicolored slates and siltstones with rare metalimestone or meta-chert intercalations; basal calcschists also occur.

The Ophiolitic Unit (TC IV) is composed of several minor thrust sheets or tectonic sub-units, which are characterized by serpentinites, ophicalcites, Mg-gabbros, and Jurassic-Lower Cretaceous sedimentary cover [*Bortolotti et al.*, 2001].

The Paleogene Flysch Unit (lower part of TC V) mainly consists of shales, marls with limestone, sandstone, and ophiolitic breccia intercalations including fossils of the Paleocene-Eocene age. The Lower-Upper Cretaceous Flysch Unit (upper part of TC V) consists of basal shales and varicolored shales. These lithologies vertically pass to turbiditic siliciclastic sandstones and conglomerates, which in turn alternate with marlstones and marly limestones. Both Flysch Units were intruded by aplitic and porphyritic dykes and laccoliths approximately 7-8 Ma ago [*Dini et al.*, 2002b].

The geological structure of the island allows a nearly complete representation of lithologies present in the Northern Apennines mountain chain (Figure 3.1). This feature makes Elba Island a complex system in terms of both geological formations and lithologies. Therefore, it is a formidable research site for applying a multivariate interpolation of radiometric data in relationship to lithologic properties.

3.3 Experimental setup, survey and data

The airborne survey performed with the AGRS_16 L (see section 1.5) was planned to be as perpendicular as possible to the main N-S strike of the geological structures of the area (Figure 3.1). The flight lines were designed in a spiral structure, constrained by the morphology of the terrain (elevations 0÷1010 m a.m.s.l.), starting from the shore and following the heights of the mountains in the counterclock direction (Figures 3.6, 3.7, 3.8). The unique region not properly covered by the airborne γ-ray survey is the top of Capanne Mt., because of the cloudy weather conditions. Averaging the flight altitudes recorded every two seconds we have 140 ± 50 m (standard deviation). The survey parameters were designed for a cruise speed of approximately 100 km/h, with space lines at most 500 m from one another. For our flight conditions, the detection system is able to measure the signal (97%) coming from a spot area of approximately 600 m radius, even if 90% comes from the half of this radius. In this study, the effect of attenuation of the signal from the biomass [*Carroll and*

Carroll, 1989; *Schetselaar*, 2000] was neglected since Elba Island is covered by a large extension of rock outcrops and scattered vegetation of Mediterranean scrub.

The signal was acquired in list mode (event by event) using an integrated electronic module with four independent signal-processing channels and then analyzed offline in 10s intervals. This time interval was chosen such as to optimize the loss in spatial resolution and to reduce the statistical uncertainty to less than 10%. The γ-spectra were calibrated and analyzed using the Full Spectrum Analysis with Non-Negative Least Squares (FSA-NNLS) approach as described in [*Caciolli et al.*, 2012]. According to the FSA method the spectrum acquired during the offline analysis was fitted as a linear combination of the fundamental spectra derived for each radioelement and for background from the calibration process. The abundances were determined applying the non-negative least squares to minimize the χ^2: the NNLS algorithm reduces the presence of non-physical results, which can lead to systematic errors [*Caciolli et al.*, 2012].

Several corrections were applied to the signal measured at different flight altitudes to determine the concentrations of K, eU (equivalent uranium) and eTh (equivalent thorium) at the ground: a) aircraft and cosmic background correction; b) topology correction; c) flying altitude and height correction and d) atmospheric radon correction. The dead time correction was found to be negligible due to relatively low count rates measured during the flight. The background correction was taken into account during the calibration process where the fundamental spectra of the background due to the aircraft and cosmic radiation is estimated. The numeric regional topographic map at 1:10,000 scale of the ground surface was accounted for the digital elevation model, which has a 10 m spatial resolution. The effects of the steep Elba Island's topography (ranging between 0 m to 1010 m a.m.s.l.) were corrected following the method described in [*Schwarz et al.*, 1992]. Finally, to compute the concentration at the ground surface, the signal was further corrected by an empirical factor obtained by measuring the signal at several altitudes over a flat surface well characterized by ground measurements. The altitude and topography corrections introduced a total systematic uncertainty on the order of 10% in the final results.

Further corrections were required for eU concentration because the signal coming from ground uranium is increased by the radon gas in the air. It was evaluated by using the method of the 'upward-looking' detector, following the procedure described in [*IAEA*, 1991]. The atmospheric radon concentration is estimated by analyzing the spectrum acquired with the 'upward-looking' detector, which was calibrated by flying over the Tyrrhenian sea at the beginning and the end of the survey. The radon concentration was calculated for each time interval and was almost stable during the entire flight (0.2 ± 0.1 μg/g). Since the ground abundance of eU varies from 0.2 μg/g up to 28.0 μg/g over all of Elba Island, the uncertainty concerning the atmospheric radon subtraction for each single measurement varies from 2% up to 100%: indicatively in average the relative uncertainty was 23%.

The relative uncertainties for K, eU, and eTh abundances in the final results are summarized in Table 3.1. The activity concentrations of 1 μg/g U (Th) corresponds to 12.35 (4.06) Bq/kg and 1% K corresponds to 313 Bq/kg. The systematic relative uncertainties were estimated by combining the contributions from the altitude and topography corrections and the calibration process. For the eU it includes the uncertainty related to atmospheric radon correction. The data used as input in the CCoK interpolation were taken into account without experimental uncertainties and that their positions are related to the center of the spot area.

Table 3.1 Experimental relative uncertainties for the measured abundances of K, eU, and eTh.

Radionuclide	Statistical	Systematic
K	7%	14%
eU	8%	~30%
eTh	8%	15%

3.4 Collocated cokriging: theoretical background

Geostatistical interpolation algorithms construct probability distributions that characterize the present uncertainty by the coregionalization among variables [*Wackernagel*, 2003]. The CCoK is an interpolation method widely used when applying a linear coregionalization model (LCM) to a primary under-sampled variable $Z_1(x)$ and a secondary widely sampled variable $Z_2(x)$ continuously known at all grid nodes [*Goovaerts*, 1997].

[*Xu et al.*, 1992] advanced a definition in which the neighborhood of the auxiliary variable $Z_2(x)$ is arbitrarily reduced to the target estimation location x_0 only. They formulated CCoK as a simple cokriging linked to the covariance structure [*Chiles and Delfiner*, 1999]:

$$\rho_{12}(h) = \rho_{12}(0)\rho_{11}(h) \qquad (3.1)$$

where $\rho_{11}(h)$ is the correlogram of the primary variable $Z_1(h)$ and $\rho_{12}(h)$ is the cross-correlogram, which quantifies the spatial correlation between the primary (Z_1) and the secondary (Z_2) data at a distance h.

Assuming $Z_1(x)$ to be known, the value of the primary variable Z_1 at target location x_0 is independent of the value of the secondary variable Z_2 if Z_1 and Z_2 have a mean of zero and a variance of one. In this case, which is called a "Markov-type" model, the cross covariance functions are proportional to the covariance structure of the primary variable [*Almeida and Journel*; *Xu et al.*, 1992]. A strictly CCoK estimator $Z^{**}_{1_{CCoK}}$ at target location x_0

depends on both the linear regression of the primary variable Z_1 and the simple kriging variance σ_{SK}^2, for $\rho = \rho_{12}(0)$ as follows [*Chiles and Delfiner*, 1999].

$$Z_{1_{CCoK}}^{**}(x_0) = \frac{\left(1-\rho^2\right) Z_1^*(x_0) + \sigma_{SK}^2 \rho Z_2(x_0)}{\left(1-\rho^2\right) + \rho^2 \sigma_{SK}^2} \tag{3.2}$$

where Z_1^* is the kriging estimation of Z_1 at the target location x_0 and the accuracy of the CCoK estimation is given by

$$\sigma_{CCoK}^2 = \sigma_{SK}^2 \frac{\left(1-\rho^2\right)}{\left(1-\rho^2\right) + \rho^2 \sigma_{SK}^2} \tag{3.3}$$

3.5 Interpolating airborne γ-ray data on geological constraints

In this study, the CCoK was used as a multivariate estimation method for the interpolation of airborne γ-ray data using the geological map information. The primary variable $Z_1(x)$ refers to the discrete distribution of the natural abundances of K, eU, or eTh (equivalent thorium) measured via airborne γ-ray spectrometry, whereas the secondary variable $Z_2(x)$ refers to the continuous distribution of the geological formations (i.e., the geological map). In this work, these two sets of information are independent of one another. The data gained through airborne γ-ray spectrometry define a radiometric spatial dataset integrating the sample point positions with the natural abundances of K (%), eU (μg/g), and eTh (μg/g), together with their respective uncertainties.

The geological map at a 1:10,000 scale [*CGT*, 2011], obtained from a geological field survey, covers the entire area in detail. Moreover, the geological map lists 73 different geological formations, defining in this way a categorical variable. For such a large number of variables, the approach based on categorical variables [*Bierkens and Burrough*, 1993] [*Goovaerts*, 1997] [*Hengl et al.*, 2007] [*Journel*, 1986] [*Pardo-Igúzquiza and Dowd*, 2005] [*Rossi et al.*, 1994] requires a long time for processing and interpretation. Therefore, the geological qualitative (categorical) map has to be considered as a quasi-quantitative constraining variable. In order to study the frequency of sampling the geological formations names were sorted in alphabetical ascending order and then to each one a progressive number was assigned. The frequencies were arranged for obtaining normal distributions of the secondary variable (geology). As is shown in the following section, this procedure didn't affect the final interpolation results. Thus, the airborne γ-ray measures were spatially joined to the geological map. This migration of geological data from the continuous grid (the

geological map) to the sample points (the airborne γ-ray measuring locations) was performed to yield a multivariate point dataset to be interpolated by CCoK. As shown in Table 3.2, K (%) and eTh (µg/g) abundances have a quasi-Gaussian distributions, whereas eU (µg/g) abundance distribution tends to be positively skewed. The linear correlation is high between pairs of abundance variables (Figure 3.2). Based on the previous assumptions, the linear correlation coefficient between radioactivity measures and values arbitrary assigned to geological formations is meaningless.

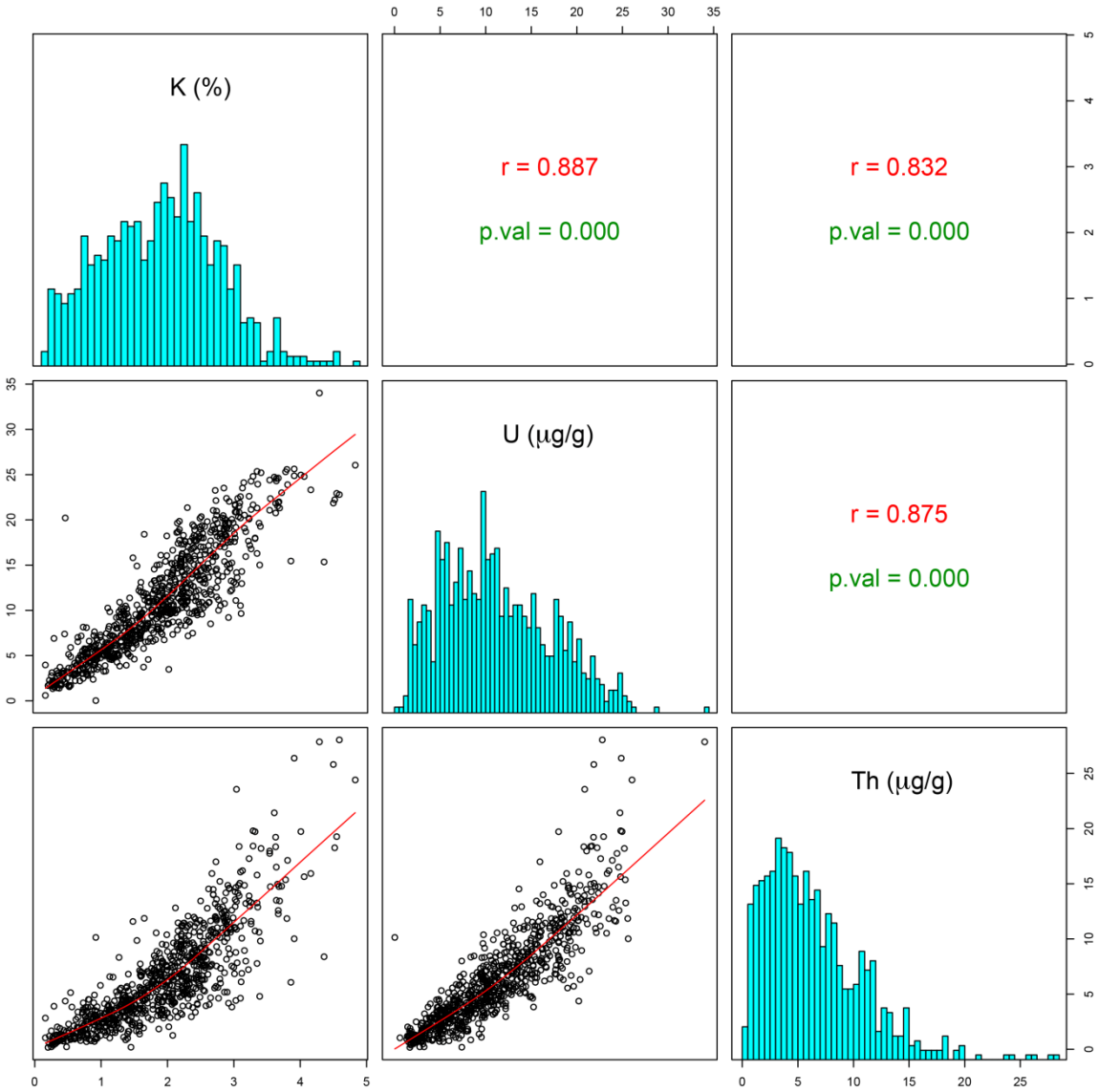

Figure 3.2 Correlation matrix of abundance variables: the lower panel shows the bi-variate scatter plots for each pair of variables and the robust locally weighted regression, red line; cells on the matrix diagonal show the univariate distributions of abundances; the upper panel shows both Pearson's linear correlation coefficient value for each bivariate distribution and the statistical significance testing scores (p-value) for each correlation test.

Table 3.2 Descriptive statistical parameters of airborne γ-ray data.

Parameter	K (%)	eU (µg/g)	eTh (µg/g)
Count	806	805	807
Minimum	0.2	0.2	0.03
Maximum	4.8	28.0	34.0
Mean	1.9	6.4	11.1
Std. Dev.	0.9	4.4	5.9
Variance	0.8	19.7	35.2
Variation Coeff.	0.5	0.7	0.5
Skewness	0.2	1.3	0.5

The CCoK interpolation models, both for the direct spatial correlation and the cross-correlation of these regionalized variables, were obtained by calculating experimental semi-variograms (ESV) and experimental cross-semivariograms (X-ESV), and interpreting the models by taking into account factors conditioning the spatial distribution of these regionalized variables. The distributions of radioelements of the input dataset show a positive skewness of 0.2, 0.5 and 1.3 for K, eTh and eU respectively (Table 3.2). In the case of skewness values less than 1, several authors [*Rivoirard*, 2001; *Webster and Oliver*, 2001] suggest to not perform any normal transformation of the data. Considering that the measurement of eU is contaminated by radon, which increases the experimental uncertainty, any refinement of data processing was considered redundant. In addition, supported by well-structured ESVs and X-ESVs for the raw datasets, any normal transformation for K, eU and eTh was not performed.

Table 3.3 Parameters of linear coregionalization models fitted on omnidirectional variograms calculated with 8 lags of 200 m: groups of primary (radionuclides) and secondary variables; number and types of systems of functions fitted on experimental variograms; range distances for each system of function; matrices of each structure of variability of linear coregionalization model (LCM) fitted for different groups (model values for EVSs in each matrix diagonal cells, model values for XESVs in lower left panel of each matrix; variability values of the parametric geology, in the right column, are unitless); cross-validation results of the fitted LCM (only the primary variables scores are listed; MSE: mean of standardized errors; VSE: variance of standardized errors) for all groups of variables**.**

Group of variables	Number and Type of Structures of variability		Range (m)	LCM matrices		Cross-validation	
						MSE	VES
K & geology	1	Nugget Effect Model	-	0.01 $\%^2$	-	-0.0016	0.68
				0.3 $\%^2$	15		
	2	Spherical Model	400	0.1 $\%^2$	-		
				-0.6 $\%^2$	87		
	3	Spherical Model	1500	0.3 $\%^2$	-		
				-1.2 $\%^2$	105		
eU & geology	1	Nugget Effect Model	-	2.5 µg/g^2	-	-0.00016	0.73
				0.1 µg/g^2	87		
	2	Spherical Model	1500	5.7 µg/g^2	-		
				-5.7 µg/g^2	120		
eTh & geology	1	Nugget Effect Model	-	0.4 µg/g^2	-	-0.0008	0.65
				-0.1 µg/g^2	15		
	2	Spherical Model	400	2.1 µg/g^2	-		

				-0.4 μg/g^2	87		
	3	Spherical Model	1500	11.2 μg/g^2	-		
				-10.6 μg/g^2	105		

The directional X-ESVs show erratic behavior. Therefore, the experimental co-variability was modeled as isotropic, and an omnidirectional LCM was fitted using a trial-and-error procedure. As shown in Table 3.3, the Gaussian distribution has the mean of standardized errors close to zero and the variance of standardized errors close to unity, which allowed the use a cross-validation method. The quality of the model [*Goovaerts*, 1997] was double-checked by comparing the errors made in estimating airborne γ-ray measures at sample locations with the theoretical standard Gaussian distribution.

Each group of variables shows the same spatial variability of the geology in the coregionalization matrices because the same parametric variable is still used for all models in the estimation of abundance distribution maps of radioactive elements (Table 3.3). The result shows a well-structured spherical variability for all groups of variables (Figures 3.3, 3.4 and 3.5).

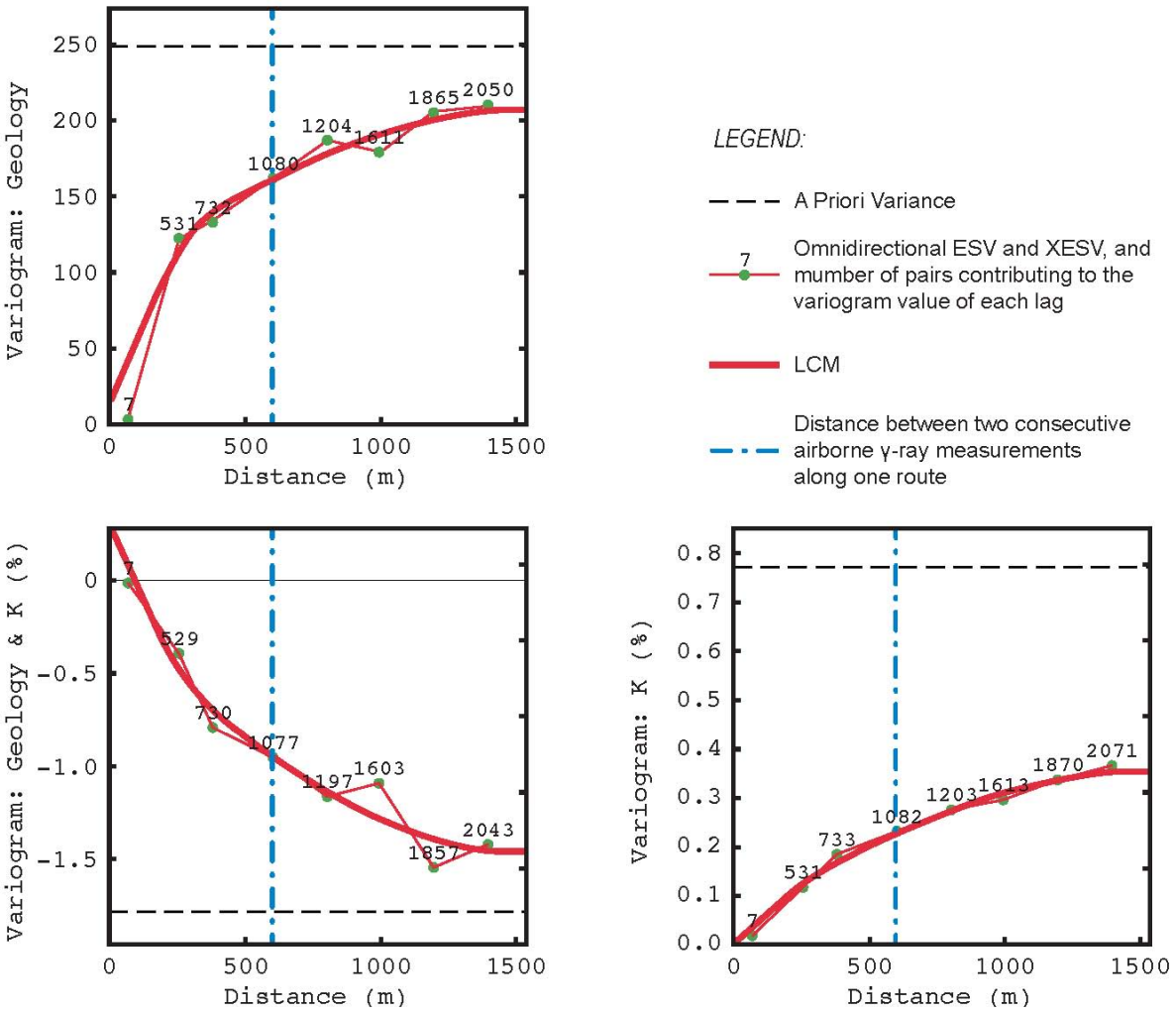

Figure 3.3 Omnidirectional Linear Coregionalization Model fitted for the experimental semi-variograms (ESV, on diagonal cells of the matrix) and cross-semivariograms (XESV lower left corner cell) for Geology and K.

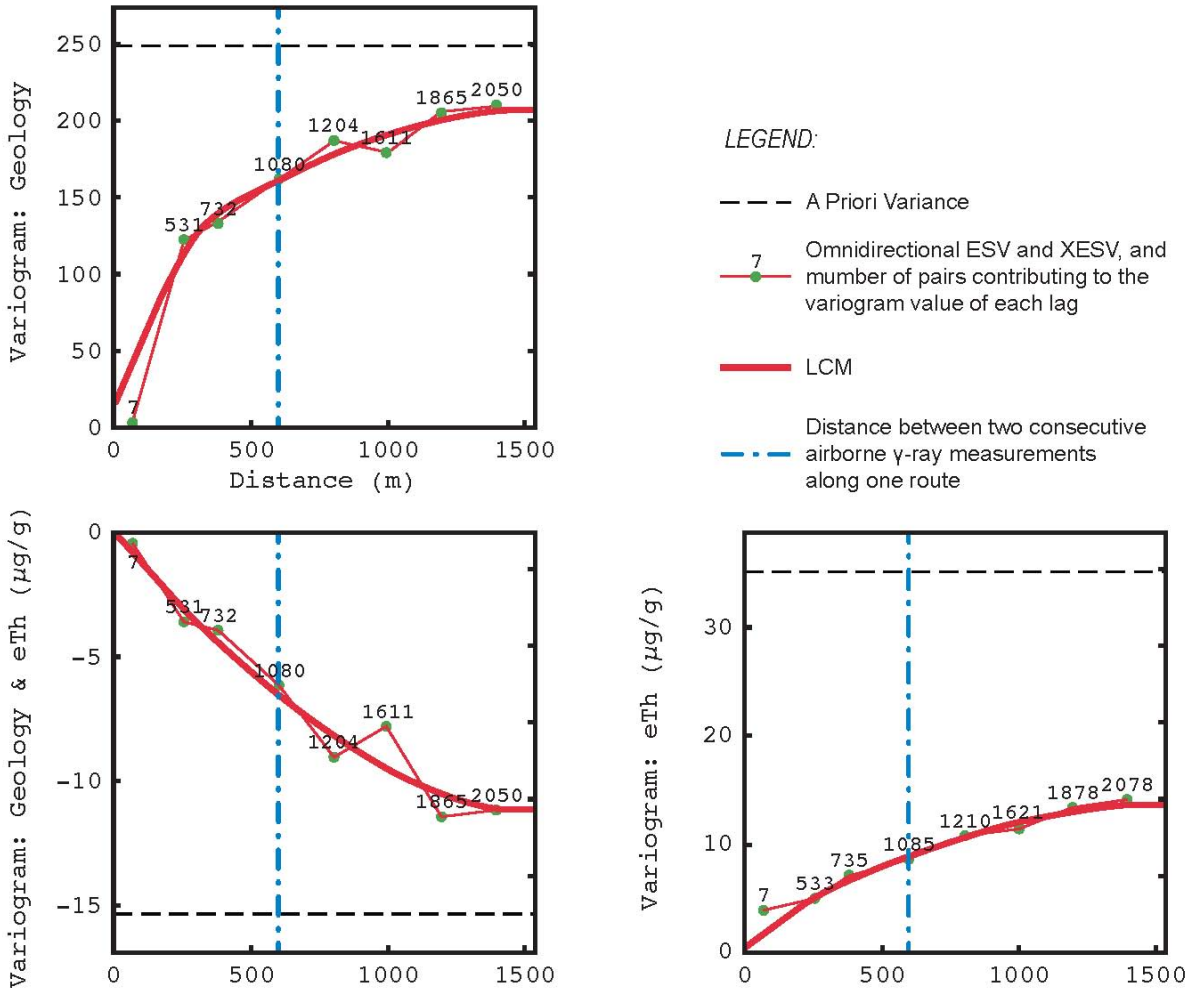

Figure 3.4 Omnidirectional Linear Coregionalization Model fitted for the ESV and XESV for Geology and eTh.

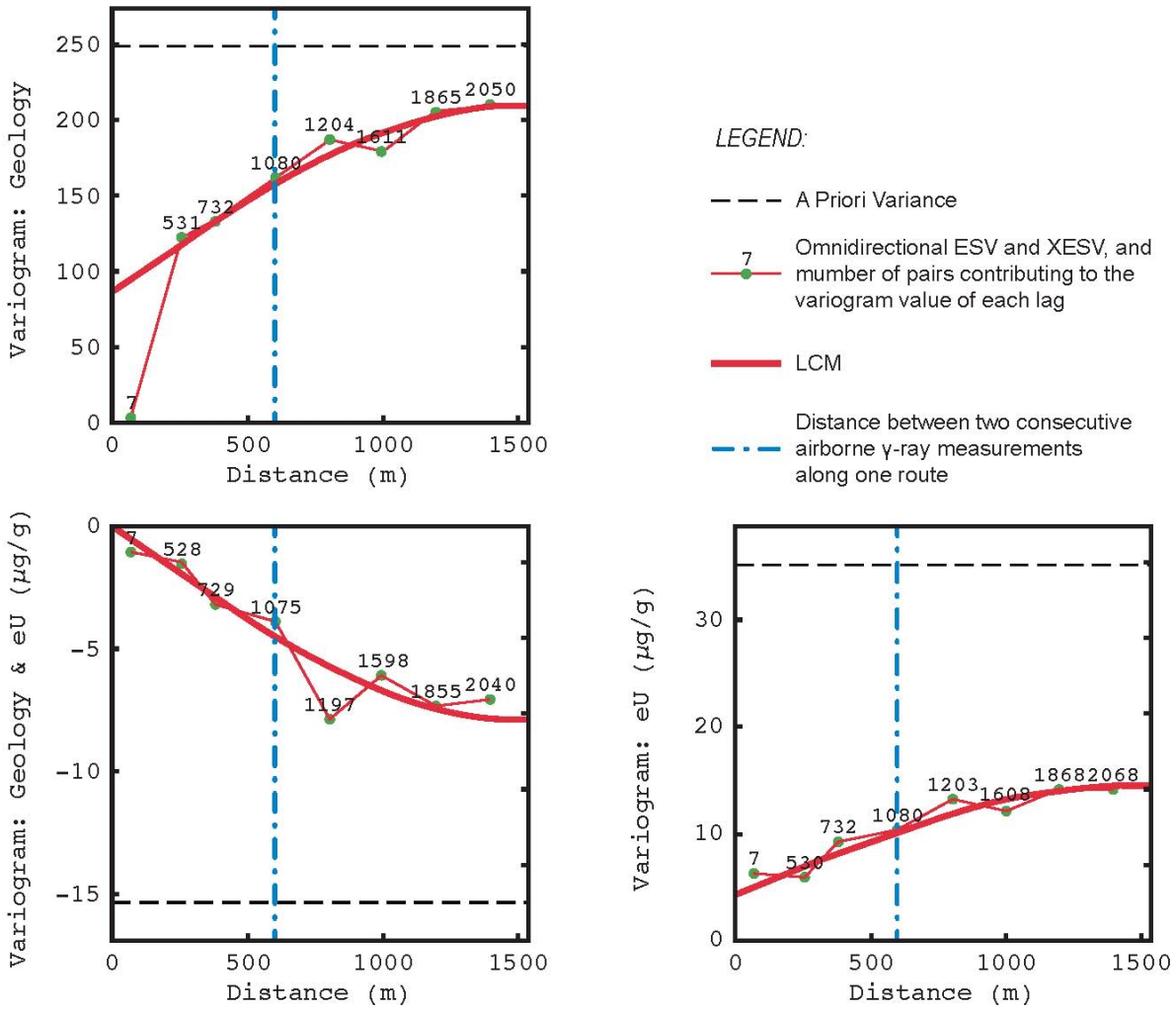

Figure 3.5 Omnidirectional Linear Coregionalization Model fitted for the ESV and XESV for Geology and eU.

3.6 Results and discussions

On the 3rd of June, 2010, the autogyro flew over Elba Island (224 km^2): during approximately two hours of flight, the ARGS system collected 807 radiometric data with an average spot area of approximately 0.25 km^2 (source of 90% of the signal). The average altitude of the flight was 140 ± 50 m.

Performing the post-processing described in section 3.3, homogenous K, eU, and eTh abundances were associated to each spot area. Considering that 96% of the total 2574 geological polygons covering the surface of Elba Island have an area less than 0.25 km^2, it was observed that many of the airborne γ-ray measurements refer to the contributions coming from several geological formations with different lithological compositions. However, these polygons cover only 25% of the surface of Elba Island. The high density of radioactivity data and the highly refined geological map allowed to construct a well tested LCM: the cross-validation results are shown Table 3.3. Based on this consistent framework, the multivariate

analysis produced data characterized by a good assessment of spatial co-variability.

According to the flight plan, the autogyro crossed its own route resulting in a very low variability in the first lags of the omnidirectional co-regionalization model (e.g. ESV of K in Figure 3.3). The ESV models referred to AGRS measurements show regular structures with low variability at small distances and generally higher variability at the spherical parts. Indeed, the nugget effect of K abundance contributes almost 2% of the total amount of spatial variability, providing evidence of autocorrelation. The same features are found for the eTh and eU abundances, whose variances at small distances contribute 3% and 30% of the total spatial variation, respectively.

Moreover, a low spatial variability is clear below 600 m (indicating the spot area radius, indicated by the blue dashed line in Figures 3.3, 3.4 and 3.5), which corresponds to data obtained by partially overlapping spot areas. The maximum distance of spatial autocorrelation for K, eU, and eTh is 1500 m (Table 3.3), this also due to their high statistical correlation (Figure 3.2). These features reconstructed the spatial resolution of the AGRS survey, confirming the consistency of the model and the AGRS data.

The variability of the parametric geology variogram at small distances shows a weak variability discontinuity at lag $h = 0$, i.e., a nugget effect. This contributes almost 50% of the total spatial variability together with the first range of autocorrelation found at 400 m. This due to either the random values assigned to the categories of the geological map, where a significant difference can be found between the sample values of two adjacent geological formations or in the 600 m spot area radius (Figures 3.3, 3.4 and 3.5).

The X-ESVs constructed for radioelement-geology couples generally show well-defined co-variability structures. Indeed, both the spherical components of the model are well structured and the contribution of the random part of the variability is always minimized (Figures 3.3, 3.4 and 3.5). Therefore, these choices ensure the consistency of the results achieved by the CCoK multivariate interpolator.

The estimated maps of the K, eTh, and eU abundances are shown in Figures 3.6, 3.7, and 3.8. These maps were calculated with a high spatial resolution (pixel size 10 m x 10 m) in accordance with the choice of the geological map at scale 1:10,000. The accuracy of the estimations in terms of the variance, normalized respect to the estimated values of the abundances (normalized standard deviation, NSD) is also reported. The percentage uncertainties of the abundances are higher when the absolute measures are smaller, with average NSDs of 27%, 28%, and 29% for K, eU, and eTh, respectively.

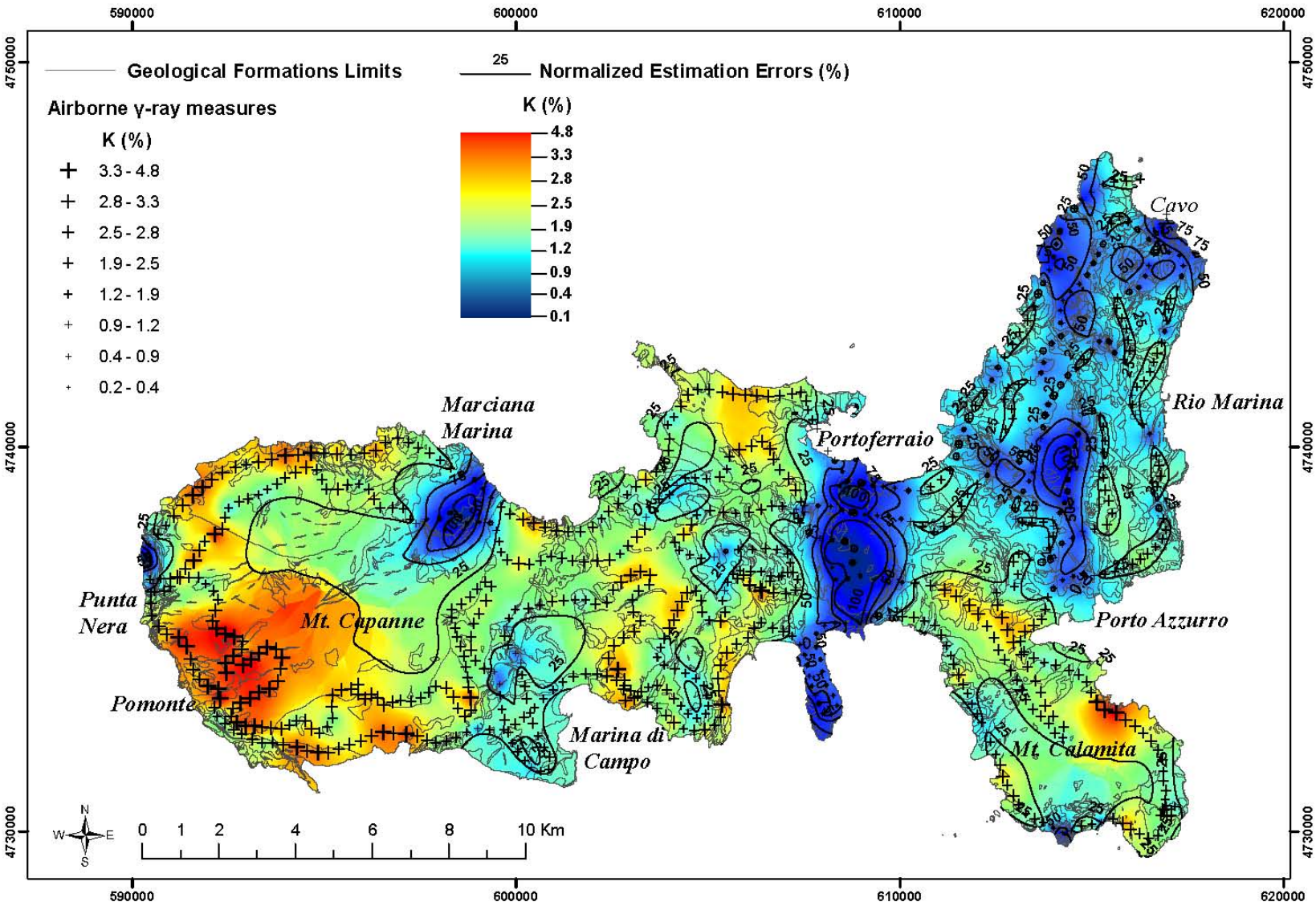

Figure 3.6 Estimation map of K (%) abundance and normalized estimation errors.

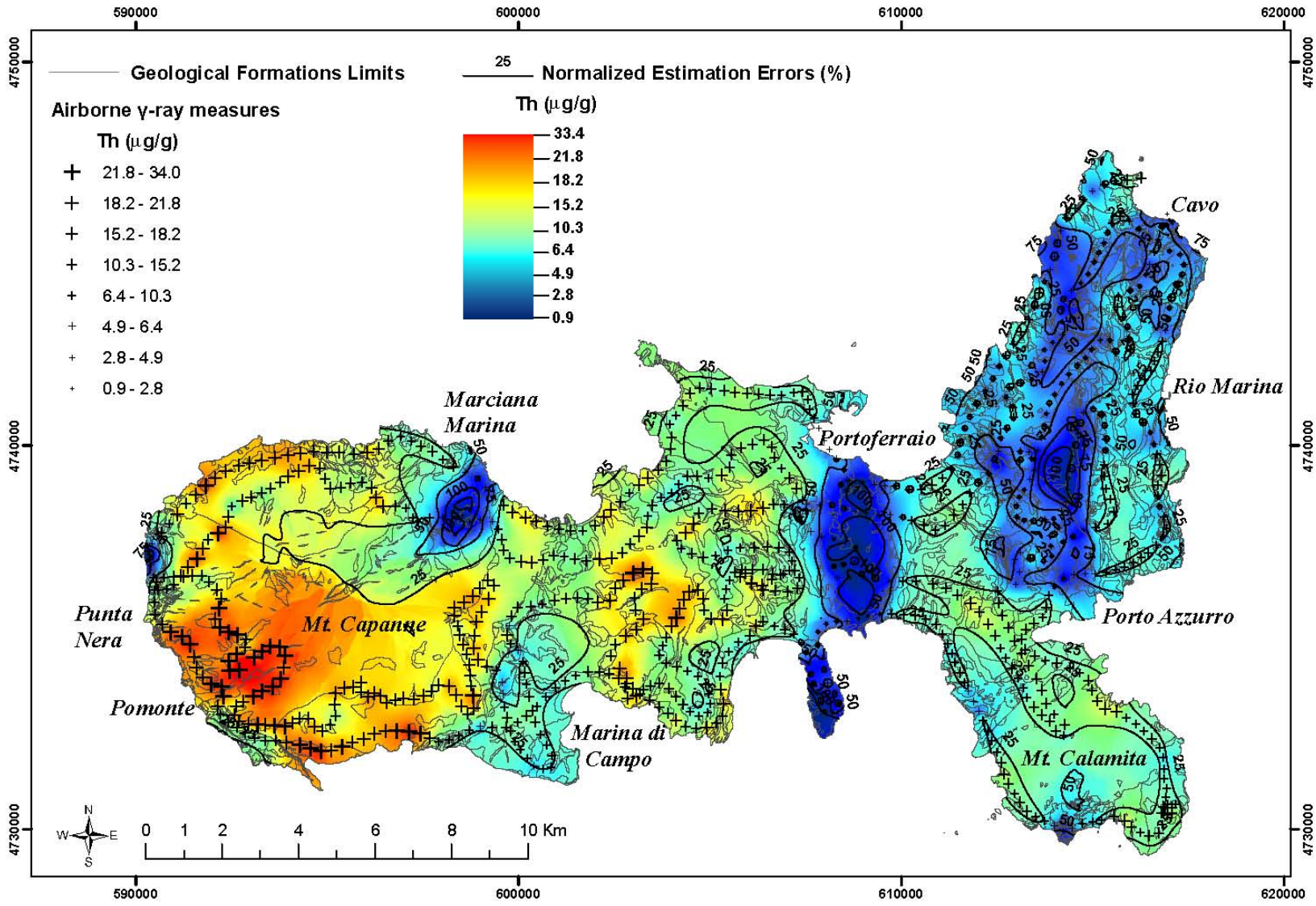

Figure 3.7 Estimation map of eTh (µg/g) abundance and normalized estimation errors.

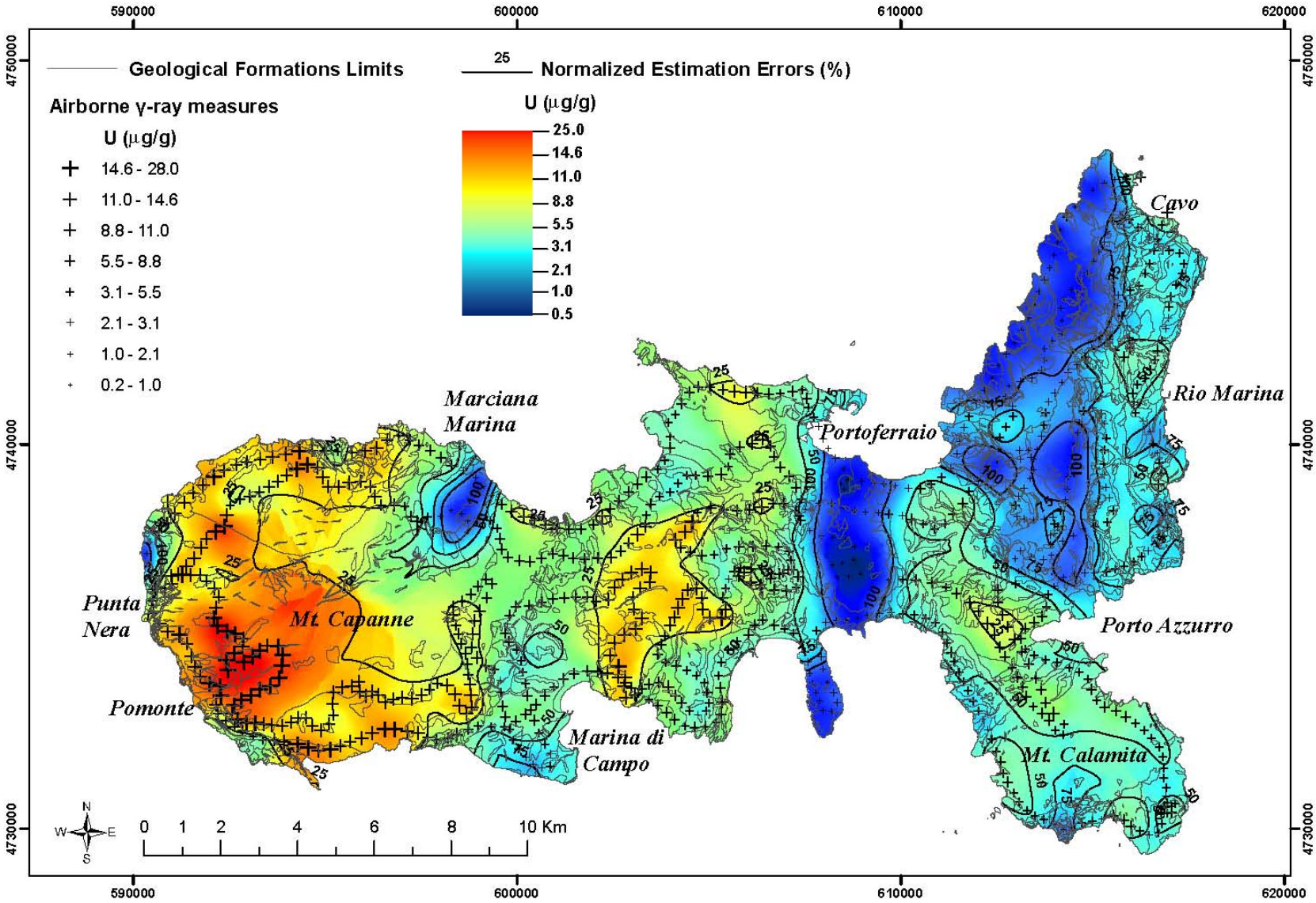

Figure 3.8 Estimation map of eU (μg/g) abundance and normalized estimation errors.

In the geostatistical approach described above, the problem of correlating a quantitative variable (radioactivity content) to a typical categorical extensive variable (geological map) was faced. As a first solution, the standard Gaussian distribution of the secondary variable (Geo1) was chosen in a range of values from -10^2 to 10^2. In order to test possible bias introduced by the choice of the interval of values, two different distributions in the range of values from 1 to 10^2 (Geo2) and from 1 to 10^5 (Geo3) were constructed. The main results of these tests are summarized in Table 3.4 and Figure 3.9; for the sake of simplicity, only the estimated maps of K abundance were compared. However, the entire procedure for every radioelement combined with the geological parametrical map was performed. The normalized differences between pairs of maps realized for different casual geological arrays through CCoK interpolations (Table 3.4 and Figure 3.10) confirm that the random assignment didn't introduce any systematic bias. Moreover, the normalized fluctuations of K abundances estimated by three different models are contained in a range of less than 5%. The quality of the models was not weakened by the assignment of random values to geological categories.

Table 3.4 Descriptive statistics of the CCoK estimation maps of K abundances (unit of measurement: mg/g) using three different parametric classifications of the geological map (Geo1, Geo2, and Geo3), the respective estimation errors maps (NSD), and their algebraic map differences (unit of measurement: %).

Type	Geological map	Min.	Max.	Mean	Std. Dev.
CCoK estim.	Geo1	0.15	48.80	19.37	0.79
	Geo2	0.15	48.80	19.37	0.79
	Geo3	0.16	48.24	19.36	0.79
NSD	Geo1	0.79	187.62	27.24	19.58
	Geo2	0.79	217.74	27.24	19.69
	Geo3	6.00	255.00	27.22	19.89
Differ. CCoK	(Geo1-Geo2)/Geo1	-0.33	0.56	-0.001	0.001
	(Geo1-Geo3)/Geo1	-1.84	1.60	-0.004	0.076
	(Geo2-Geo3)/Geo2	-1.72	1.49	-0.007	0.082
Differ. NSD	(Geo1-Geo2)/Geo1	-44.11	91.87	-1.01	-0.88
	(Geo1-Geo3)/Geo1	-85.19	90.55	-0.09	1.21
	(Geo2-Geo3)/Geo2	-34.67	49.03	0.10	0.81

The main features of the resulting radiometric maps of abundances for the natural radioelements overlay the prominent geological formations of Elba Island. Indeed, the relevant geological structures defined by the TCs, described in section 3.2, can easily be identified by comparing similar abundances of natural radioelements.

The radiometric maps of K, eTh, and eU abundances (Figures 3.6, 3.7 and 3.8) show high values in the western sector of the island, corresponding to the intrusive granitic complex on Mt. Capanne (indicated as the “CAPa” and “CAPb” geological formations in Figure 3.1). In 19 rock samples of Mt. Capanne pluton reported in [*Farina et al.*, 2010] the abundances of K, Th, and U are 3.6 ± 0.2 %, 20.8 ± 1.6 μg/g and 8.2 ± 5.1 μg/g respectively. The values match with those estimated in Figures 3.6, 3.7, and 3.8. Although the distributions of radioelements do not distinguish among the three intrusive facies, which are mainly

characterized by the widespread occurrence of euhedral K-feldspar megacrystspato, the area with high content of K, Th and U obtained by multivariate analysis follows the contour map of Mt. Capanne pluton reported in Figure 9a in [*Farina et al.*, 2010]. However, the highest content of K, Th and U are localized in the southwestern part of pluton with the maximum concentration in correspondence of the Pomonte valley, SW-NE oriented that is one of the most prominent morphological lineament of western Elba (Figures 3.6, 3.7, and 3.8). This is an important tectonic lineament crossing all the Mt. Capanne, abruptly separating two different morphological assets: the north-western part shows rough slopes and deep valleys, whilst the south-eastern one is characterized by gently landscape. The hypothesis of an enrichment of radioelements related to this tectonic lineament should be investigated by further airborne and ground surveys.

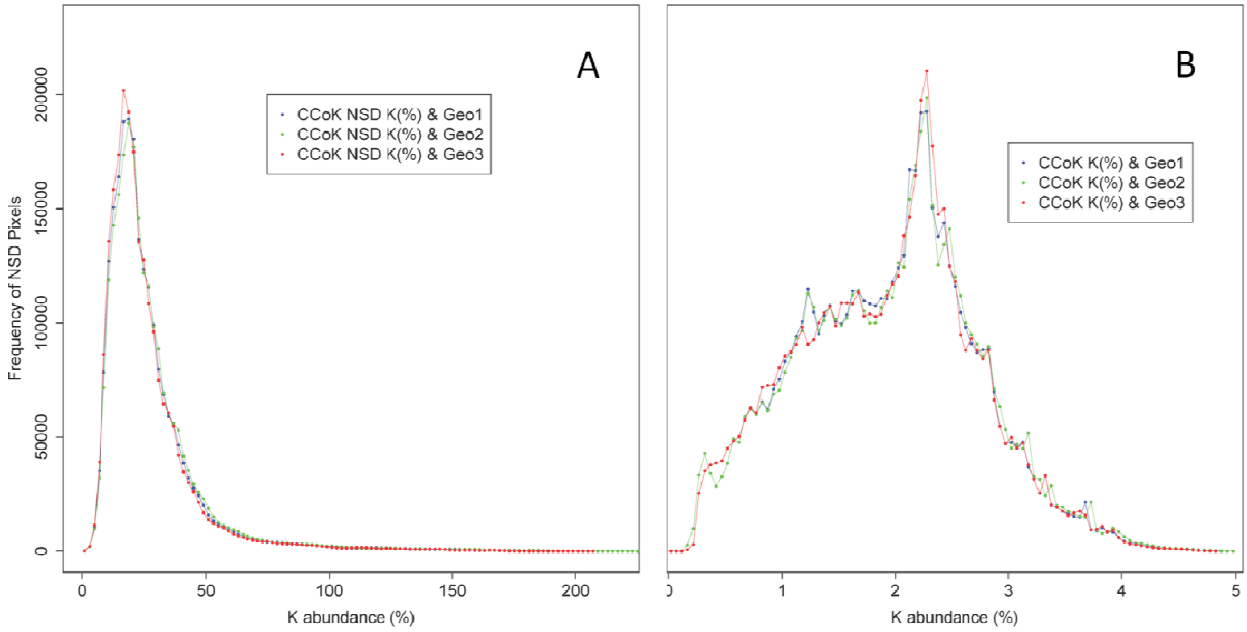

Figure 3.9 A) Frequency distributions of kriged maps of K abundances estimated by CCoK through three different reclassifications of the geological map of Elba Island. B) Frequency distributions of the normalized standard deviation maps (the accuracy of CCoK estimations).

As shown in Figures 3.6, 3.7, and 3.8 the geological formations belonging to TC II and TC III have low natural radioelement abundances. The main outcrops are located in the northeastern sector of Elba Island, between Porto Azzurro and Cavo and in the southern part of Portoferraio, where we find peridotites and pillow lavas (indicated as “PRN” and “BRG”, Figure 3.1). Finally, low abundance values are found in the area of Punta Nera Cape at the western edge of the Elba Island, where lithologies belonging to the Ophiolitic Unit crop out (TC IV).

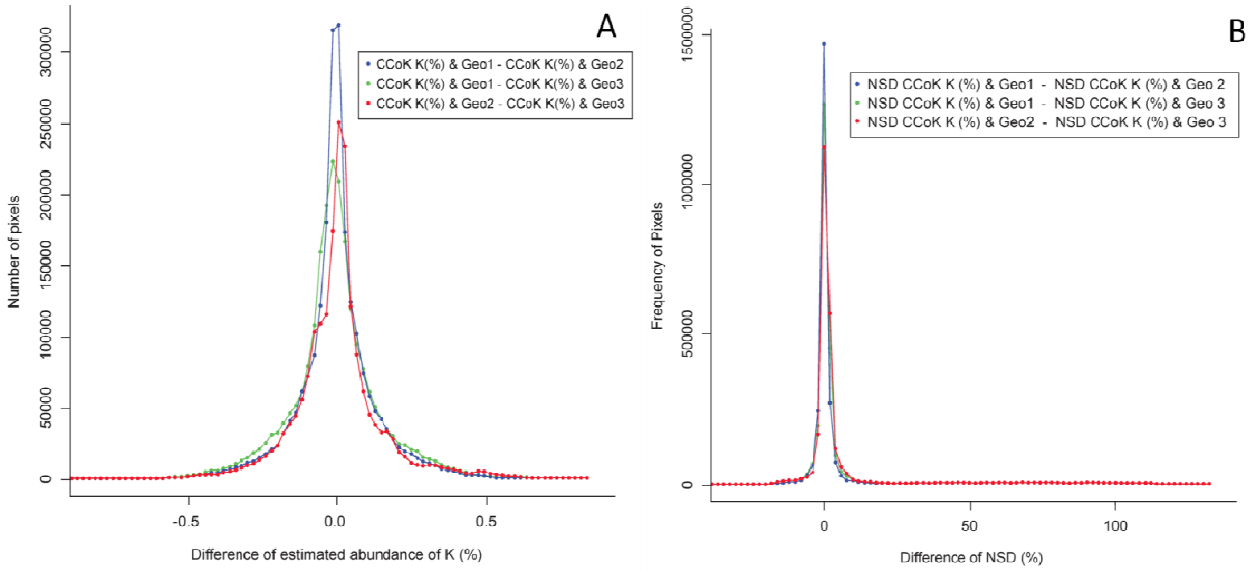

Figure 3.10 A) Frequency distributions of the differences between pairs of kriged maps of K abundances estimated by CCoK through three different reclassifications of geological maps of Elba Island. B) Frequency distributions of the differences between pairs of normalized standard deviation maps.

Although a unique number to each geological formation was assigned, the internal variability of the radiometric data is not biased by the multivariate interpolation. The main evidence of this feature can be observed inside the polygon including Mt. Calamita, which is identified by a unique geological formation "FAFc" (Figure 3.1). A clear anomaly of high K abundance is evident in the northeastern sector of the Mt. Calamita promontory, close to Porto Azzurro (Figure 3.6). This anomaly can be geologically explained considering two related factors. The intense tectonization and following fracturation of this sector allowed a significant circulation of magmatic fluids related to the emplacement of monzogranite pluton of La Serra-Porto Azzurro. Moreover, the presence of felsic dykes, metasomatic masses and hydrothermal veins are recently confirmed by [*Dini et al.*, 2008] and [*Mazzarini et al.*, 2011]. Although the adopted geological map doesn't report these lithological details, the quality of radiometric survey is such as to identify the location of the felsic dyke swarm. These dykes 30 - 50 cm thick represent the dominant lithology at the mesoscopic scale and their high frequency in FAFc geological formation contributes to increase the gamma-ray signal. These details are not compromised by the multivariate analysis. The spatial extension of high K content validates the geological sketch reported in Figure 1 by [*Dini et al.*, 2008].

The content of this chapter is based on the following publication:

Guastaldi E., Baldoncini M., Bezzon G.P., Broggini C., Buso G.P., Caciolli A., Carmignani L., Callegari I., Colonna T., Dule K., Fiorentini G., Kaçeli Xhixha M., Mantovani F., Massa G., Menegazzo R., Mou L., Rossi Alvarez C., Strati V., Xhixha G. and Zanon A. *A multivariate spatial interpolation of airborne γ-ray data using the geological constraints.* Remote Sensing of Environment (2013) 137(0): 1-11.
DOI:10.1016/j.rse.2013.05.027

Chapter 4

Geological characterization of the oil fields of Vlora-Elbasan region (Albania) supporting the assessment of Naturally Occurring Radioactive Materials (NORMs)

The Naturally Occuring Materials (NORMs) are natural origin materials containing radionuclides and subject to regulation. The materials modified by human made processes, such as those generated from oil and gas extractions, belong to this controlled category. Several environmental studies have shown that the release of produced water into the oil well's surroundings, into decantation plants and into oil spillage sites can result in serious soil, water and air contamination from BTEX (acronym for Benzene, Toluene, Ethylbenzene, and Xylenes), volatile organic compounds or crude oil [*Beqiraj et al.*, 2010; *Guri et al.*, 2013]. However, after a century of oil exploration in Albania with poor regulatory criteria, especially in the early beginnings, the risk of soil contamination from NORMs needs to be investigated. Moreover, the implementation in the Albanian legislation of the European recommendations regarding the "Basic Safety Standards for the protection against dangers arising from exposure to ionizing radiation [*CD2013/59/EURATOM*, 2014]" is highly desirable. According to this directive, the identification and monitoring of industrial processes involving NORMs should be conducted by countries to assess the radioactive exposure to workers or members of the public.

In this framework, can the radiological assessment go beyond for predicting future hazards, integrating a multi-method approach? The following case study consists in the assessment of NORMs in four Albanian oil fields located in the productive region Vlora-Elbasan through γ-ray spectrometry performed on collected samples of different matrix. The radiological evaluation of the oil fields was enhanced by a multidisciplinary approach and I was involved in the challenging issue of the geological characterization of the oil reservoirs. The goal of this investigation is not only a conventional monitoring, but its ambition is to make previsions on the radiological impact on the base of integration of geological, chemical and γ-ray data.

After a necessary understanding of the geological framework of the area, I occupied of the textural characterization of the soil samples and of the interpretations of the results in terms of radionuclides abundances and mineralogical analysis. In particular I compared the abundances measured in soils, oil-sands and sludges to published studies performed in different countries. Supported by the results of the mineralogical composition, I described the occurrences of NORMs in soils through geological hypotheses. This refined investigation and

the comparison with published European reference standard came to light that a radiological contamination was not found in the study area and that the radiation exposure to workers in the oil industry was negligible from increased gamma dose rates. Moreover the radiological characterization of oil-sands were used to discriminate the lithological features of different oil fields and to test geodynamic models. In particular from the obtained results, we emphasize that the NORMs originated from Kucova oil field show higher activity concentrations, due the terrigenous nature of the oil reservoir. This evidence emerged thanks to the multidisciplinary approach, the key-point of this study, can permit to make future previsions supporting the planning of the oil extraction.

4.1 Background

Petroleum exploration and production in Albania began in the second decade of the 20th century in the Vlora-Elbasan Region, which is characterized by Neogene clastic deposits. The primary oil extraction technique in Albania uses beam pumps, which exploit the pressure of the gas in the reservoir, forcing oil out and into the well. Recently, several secondary recovery techniques, such as water and steam injection, have been employed in pilot wells in the area, leading to an increase in the oil production rate. In the future, the use of unconventional methods of shale gas extraction such as "fracking" is not excluded. All these techniques may cause Naturally Occurring Radioactive Materials (NORMs) to rise to the surface as part of the flow back and production brine. In general in the oil and gas industry, specific attention is dedicated to the contamination of the oil equipment and of the oilfield area by NORMs (e.g., scale, sludge and produced water).

NORMs produced by the oil and gas industry are residues enriched with radium isotopes that originate from the uranium and thorium present in reservoir rocks. Indeed, whereas both uranium and thorium are present in hydrocarbon reservoir rocks and are essentially insoluble under reducing conditions, their progenies ^{226}Ra and ^{228}Ra concentrate in formation waters. For this reason, ^{226}Ra and ^{228}Ra are unsupported by the long-lived uranium and thorium parent radionuclides, and due to their half-lives of 1600 yr and 5.75 yr, respectively, they tend to accumulate in formation water. Produced water (i.e., water brought to the surface) may contain various cations in solution, such as barium, calcium, and strontium, as well as sulfate and carbonate anions, with which radium can consequently co-precipitate as radium sulfates or radium carbonates. This effect can lead to the subsequent formation of scales in oil and gas equipment, for which the ^{226}Ra and ^{228}Ra specific activities can be as high as 1500×10^4 Bq/kg and 280×10^4 Bq/kg, respectively, though highly variable concentrations are typically observed [*Xhixha et al.*, 2013]. Furthermore, sludge wastes (mixture of crude oil, oil-sand and soil) can also be generated, which show slightly lower activity concentrations with respect to scales, up to 350×10^4 Bq/kg and 205×10^4 Bq/kg, respectively, for ^{226}Ra and ^{228}Ra [*Xhixha et al.*, 2013]. However, no study up to now has been performed on oil-sands wastes produced during heavy oil extraction.

This study is the first investigation of the radioactivity concentration in soils, oil-sands, sludges, crude oil and produced water from the KUçova (KU), MArinza (MA), BAllsh (BA) and HEkali (HE) oilfields. This original dataset will provide baseline information concerning possible contaminations due to oil-sands. The geological framework and mineralogical analysis provide an exhaustive interpretation of the radiometric data. This analysis will allow the assessment of the environmental and human impact of the oil industry's activities on the four areas.

4.2 Geological setting

Albania is part of the Alpine Mediterranean Mountain belt and can be subdivided into two groups of tectonic units with NNW - SSE orientation: the Inner Units, characterized by intense deformation comprising ophiolites and metamorphic rocks, and the Outer Units, which are made up of regional thrusts involving sedimentary rocks of Triassic to Pliocene age [*Prifti and Muska*, 2013]. The main rocks characterizing the units of the two groups, according to the tectonic scheme, are shown in Figure 4.1. The Outer Units are affected by a major transfer zone, i.e., the Vlora-Elbasan lineament, along which most of the oil and gas fields occur [*Roure et al.*, 2010].

The onshore petroleum extraction in Albania is primarily located in the IONian unit (ION) and in the Durrës Basin, also referred to as the Peri-Adriatic Depression (PAD). The ION is an unbroken, elongate tectonic unit (ca. 60-70 km long x 60 km wide) that extends continuously southwards into Greece. In the ION, two main tectonics phases are recognized (i.e., Middle Miocene and Miocene-Pliocene), forming large anticlines and synclines cut by major high-angle reverse faults [*Robertson and Shallo*, 2000].

The exposure in the ION begins with evaporites and then passes upwards into shallow-marine platform carbonates (limestone and dolomites) of Late Triassic-Early Jurassic age. This succession culminates in a hardground (ancient lithified seafloor) overlain by pelagic carbonates and cherts (Middle–Late Jurassic to Eocene age, having a thickness of 2.5–4 km) and by terrigenous turbidites (Late Eocene-Early Miocene age, with thickness on the order of 4-6.5 km). Paleogene units are disconformably overlain by Neogenic sediments. The PAD is filled by molasses mega-sequences of conglomerates, sandstone and clastic limestones, with clays, shale, coal and gypsum at the top. The thickness of the molasses deposits increases from southeast to northwest, reaching a maximum of 5 km [*Silo et al.*, 2013].

According to [*Silo et al.*, 2013], we can recognize six hydrocarbons potential source rocks in the Mesozoic limestone stratigraphic column of the ION. The main ones are the Triassic bituminous dolomite at the bottom, the lower Jurassic schists and other Jurassic source rocks. We also find Cretaceous shales under thrust synclines, which in the future could be exploited as hydrocarbon generators.

The migration of crude oil from the Mesozoic limestone towards the Neogene reservoirs results from successive episodes driven by the aforementioned tectonic structures.

The oil currently explored in the Neogenic molasses sediments is the product of a secondary migration from underlying limestone (ION). The hydrocarbons are generally accumulated in stratigraphic traps of the PAD's clastic deposits. Because these phenomena evolved over geological time with different horizontal and vertical distributions, each reservoir displays its own characteristics due to the local geochemical conditions.

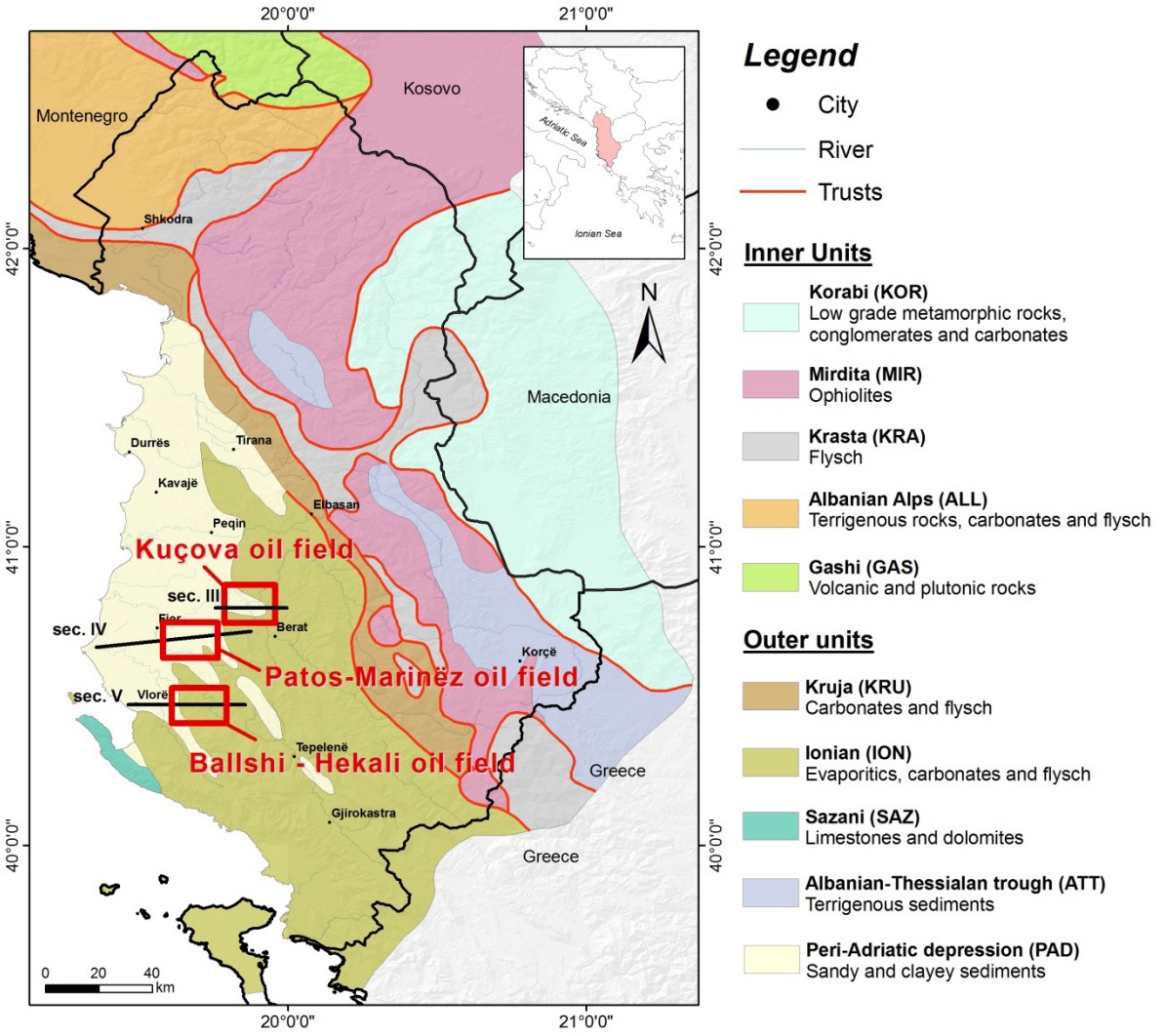

Figure 4.1 Simplified geological map of Albania modified from [*Havancsák et al.*, 2012].The labels refer to the geological units. The red squares represent the locations of the sampling areas; the solid black lines show the sections (not to scale).

4.3 Sample collection

4.3.1 Kuçova oilfield

The Kuçova (KU) oilfield is located in the central eastern part of the Durrës Basin and extends along a flat surface of approximately 14 km^2. The area is covered by alluvial sediments that were investigated with 21 soil samples (Figure 4.2-KU), collected at a depth of 0–10 cm, with the aim of characterizing the terrestrial component of the outdoor absorbed dose rate. According to the classification of USDA Soil Taxonomy, the textural

characteristics of the soil samples are overall sandy (percentage of sand > 50% for most of the samples) with medium amounts of silt (approximately 30%) and low amounts of clay (<20%).

The hydrocarbon reservoir is set in the Driza, Gorani, Kuçova and Polovina members of the Tortonian-Messinian molasses sediments (PAD). In particular, the oil being extracted is accumulated in sand lenses (Figure 4.3 sect. AA') (extending from 100 to 1500 m) sealed by shales [*Popescu*, 1994] with a high amount of clay [*Prifti and Muska*, 2013]. The depth of the reservoir has a range variable from the surface down to 1500 m.

The KU oilfield was discovered in 1928 and Bankers Petroleum Ltd., a Canadian company with the full rights to develop it, declared in 2013 approximately 297 million barrels of Original Oil in Place (OOIP). The oil extracted is characterized by API gravity values and sulfur content belonging to the ranges 14-22° and 4-5%, respectively [*Popescu*, 1994; *Prifti and Muska*, 2013]. During the periodical pipe cleaning process, we collected 10 samples of oil-sand from three different operative wells (500 – 1000 m depth) and 3 samples of sludge from the surrounding area. Furthermore, produced water and crude oil were collected in polyethylene bottles directly from the decantation plants.

4.3.2 Marinza oilfield

The Marinza (MA) oilfield, located in the southeastern part of the Durrës Basin, is the northern part of the Patos-Marinza oilfield system that extends for 5 km WE and 14 km NS. The wide plain is covered by alluvial sediments that were investigated for radiological assessment with 3 soil samples (Figure 4.2- MA) classified according to their texture as clay-loam with sand < 40% (less than Kuçova soil), clay at 35% and silt at 25%.

The Driza, Gorani, and Marinza members of the Tortonian-Messinian molasses formation (PAD) are the main hydrocarbon reservoirs. The multiple layers of unconsolidated fine grain sandstone are located at a depth ranging from 900 to 2000 m. The depositional environment is a marine environment with fluvial-channel and shore face deposits. In some cases, the underlying fractured carbonates (ION), which are located below a major unconformity (Figure 4.3 sect. BB'), can be oil reservoirs [*Popescu*, 1994; *Weatherill et al.*, 2013]. The Patos-Marinza oilfield was discovered in 1929 and the amount of OOIP is approximately 5.4 billion barrels, according to 2013 data reported by Bankers Petroleum Ltd.

The two separate fields (Patos in the south and Marinza in the north) have productive sands at different depths, i.e., 0 - 1200 m for Patos and 1200 - 1800 m for MA. The oil extracted is characterized by an API gravity value range of 3 - 33° and a sulfur content range of 2-7% [*Prifti and Muska*, 2013; *Weatherill et al.*, 2013]. We collected 1 sludge sample and 1 oil-sand sample for each of the two investigated wells (2000 and 2500 m depth) in the MA oilfield.

4.3.3 Ballsh-Hekali oilfield

The Ballsh-Hekali oilfield system is located in a hill area 29 km SE of Fieri. The radiological assessment of the two distinct fields, Ballsh (BA) and Hekali (HE), was performed by collecting 3 and 5 soil samples, respectively (Figure 4.2-BA and Figure 4.2-HE), whose textures are classified as sand or loamy sand with sand > 80%, clay < 10% and silt at 20%.

The reservoirs are restricted to Paleocene-Eocene carbonate rocks (ION) and have a depth range of 1000 - 3000 m. The geological structure consists of two superposed faulted anticlines (Fig. 4.3 sect. C-C'), and the oil stratigraphic column has a thickness greater than 550 m [*Popescu*, 1994]. The BA and the HE oilfields were discovered in 1966 and the OOIP is approximately 440 million barrels [*Popescu*, 1994]. The oil extracted is characterized by an API gravity value of 2-30°, with a sulfur content of 3-7.5% [*Prifti and Muska*, 2013]. For the radiological characterization, 2 samples of sludge were collected in an operative well of the BA oilfield.

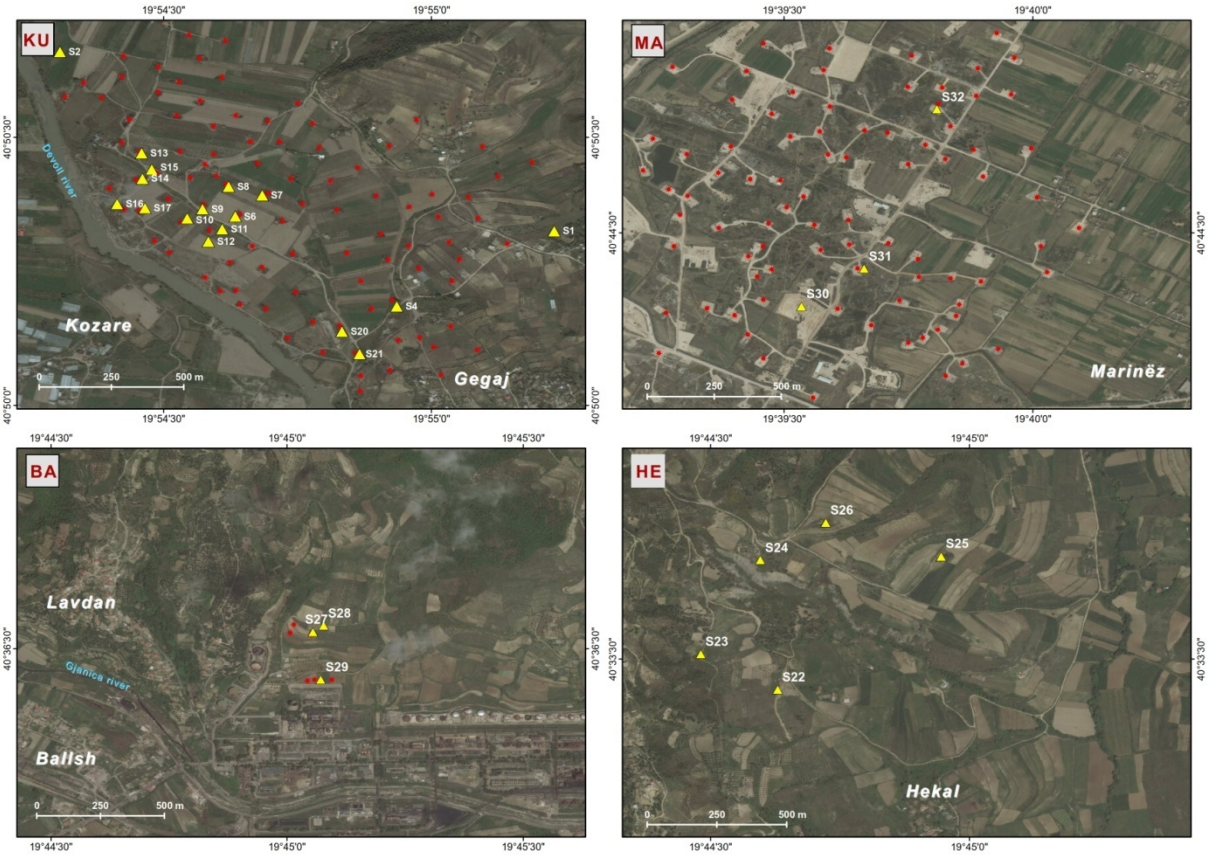

Figure 4.2 Approximate locations of the oils wells (red stars) and of the soil samples collected in the study area (yellow triangles).

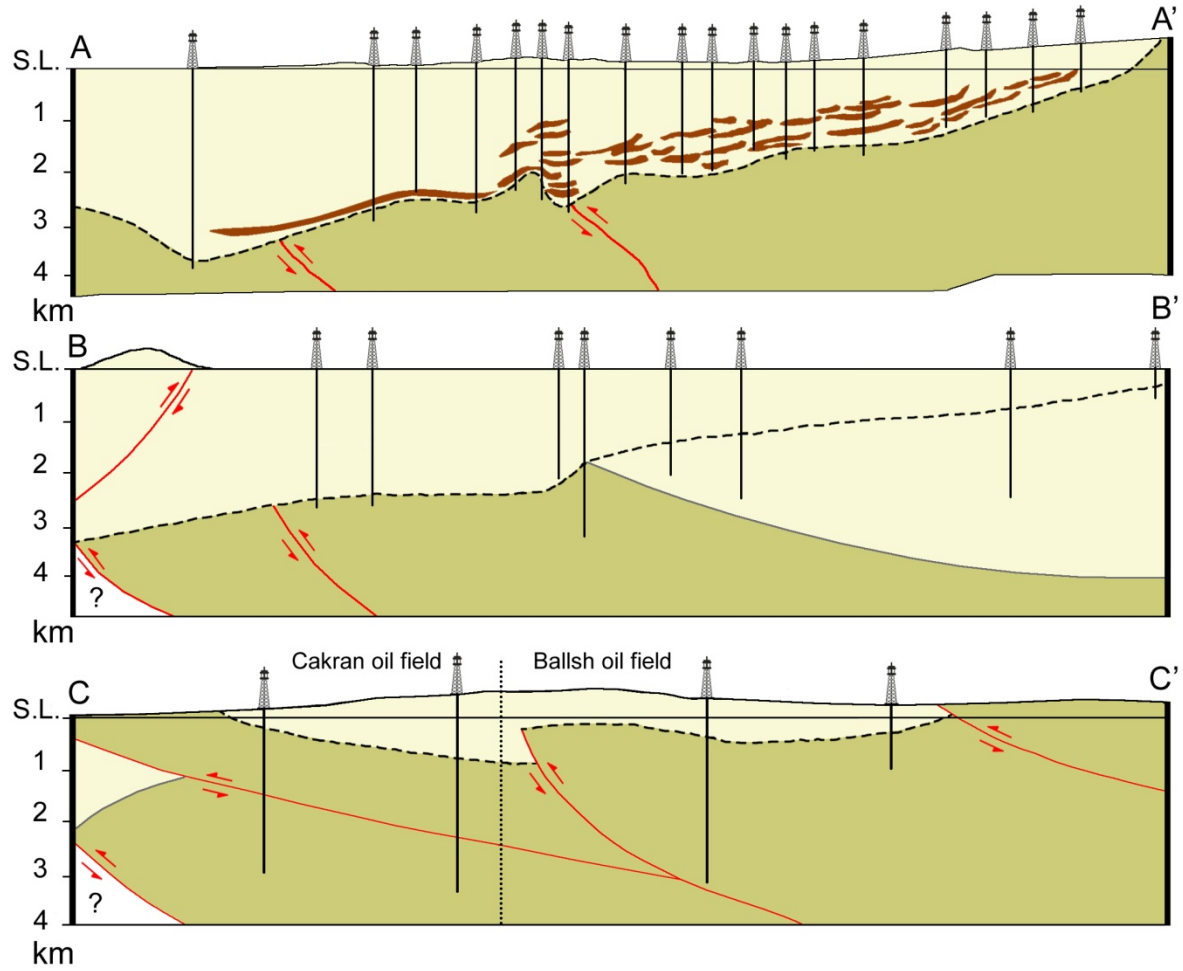

Figure 4.3 Cross sections a) A-A' in the KU oilfield, b) B-B' in the MA oilfield and c) C-C' in BA-HE oilfield (horizontal dimensions are not to scale), modified from [*Silo et al.*, 2013], obtained from the seismic lines shown in Figure 4.1. The colors of the sections are consistent with that of Figure 4.1 and correspond to the PAD (yellow) and ION (green) zones.

4.4 Sample preparations and measurements

4.4.1 HPGe gamma-ray spectrometry measurements

The samples were homogenized to a grain size of less than 2 mm and dried for at least 24 h at a temperature of 105°C until a constant weight was achieved. Produced water and crude oil were collected in polyethylene bottles directly from the decantation plants at the KU oilfield. The samples were then transferred in cylindrical polycarbonate boxes of 180 cm^3 volume, sealed hermetically and left undisturbed for at least four weeks prior to being measured with the MCA_Rad system (see section 1.4) to establish radioactive equilibrium in the ^{226}Ra decay chain segment.

The radionuclides studied in this work are ^{226}Ra, ^{228}Ra, ^{228}Th and ^{40}K by analyzing different gamma lines [*Santawamaitre et al.*, 2014]. The presence of ^{137}Cs in soils was also investigated as a proxy of Chernobyl fallout. The ^{226}Ra activity concentration was determined by analyzing the two main gamma emissions of the radon progenies, ^{214}Pb (at 352 keV) and

^{214}Bi (at 609 keV), and calculating the weighted average. ^{228}Ra was determined through its direct progeny ^{228}Ac, giving rise to gamma emissions at 338 keV and 911 keV. The ^{228}Th activity concentration was determined by analyzing the two main gamma emissions of radon progenies, ^{212}Pb (at 239 keV) and ^{208}Tl (at 583 keV). The activity concentrations of ^{40}K and ^{137}Cs were determined from their respective gamma emissions at 1460 keV and 662 keV. The acquisition time was set to 4 hours for soil, oil-sand and sludge samples and 24 hours for produced water and crude oil samples.

4.4.2 X-ray diffractometry measurements

Before undergoing mineralogical analysis, the samples were dried at 50°C for a few hours and gradually grounding on agate mortar to preserve the crystalline structure of the minerals. The XRD patterns of oriented and random samples were recorded using a GNR APD2000PRO diffractometer, with Cu Kα radiation and a graphite monochromator, operating at 40 mA and 40 kV. X-ray diffractometry of 5 samples was carried out with the divergence and scatter slits set at 1° and the receiving slit at 0.2 mm. The step size and the counting time were 0.03° (2θ) and 3s/step, respectively. A quasi-random orientation of powder samples was obtained by filling a side-entry aluminum holder. The XRD patterns were processed by the SAX Analysis software and the identification of minerals was based on the comparison with PDF-2 reference data supplied from the International Centre for Diffraction Data [*ICDD*, 2013]. A semi-quantitative analysis of the minerals identified by XRD was calculated based on chemical analysis, thermo gravimetric data related to volatile components and the Reference Intensity Ratio method.

4.5 Results and discussions

4.5.1 Activity concentrations in soil samples

The average concentration of results for the ^{40}K, ^{226}Ra and ^{228}Ra and ^{228}Th activity concentrations with ±1σ uncertainty (in Bq/kg) in soil, oil-sand and sludge samples are shown in Table 4.1. For the soil samples, the overall averages of the activity concentrations (± standard deviations) of ^{40}K, ^{226}Ra, ^{228}Ra and ^{228}Th are found to be 326 ± 83 Bq/kg, 20 ± 5 Bq/kg, 25 ± 10 Bq/kg and 25 ± 9 Bq/kg, respectively. These results are found to be lower or comparable to the global median activity concentrations of ^{40}K, ^{238}U and ^{232}Th, which are 400 Bq/kg, 35 Bq/kg and 30 Bq/kg [*UNSCEAR*, 2000], respectively. Moreover, we compared our results with data reported in several studies on the activity concentrations in soil samples from oilfields (Table 4.1). These data show a great variability, which can be attributed to natural features, such as geological and geochemical characteristics of different areas, and to human activities, such as the presence of contamination due to scales and sludges. Another case of study on natural radioactivity in Qatar [*Al-Sulaiti et al.*, 2012] relates the high concentration

of ^{226}Ra in soil samples to the NORM associated to oil and gas extraction processes. In our study, although most soil samples were found to be contaminated by crude oil and probably produced water, we do not observe any clear contamination from a radiological point of view. This is probably due to the fact that measured samples of produced water and crude oil show minimum detectable activities (MDA) for all radionuclides, corresponding to 0.4, 1.1, 0.4 and 1.4 Bq/kg, respectively, for ^{26}Ra, ^{228}Ra, ^{228}Th and ^{40}K.

Table 4.1 Average activity concentrations (±1σ) for ^{40}K, ^{226}Ra, ^{228}Ra and ^{228}Th in soil, oil-sand and sludge samples for different oilfields studied in Albania are reported together with the average (±1σ), absorbed dose rates (*DR*) and annual effective dose rates (*AEDR*). Average activity concentrations (±1σ) and ranges for ^{40}K, ^{226}Ra, ^{228}Ra and ^{228}Th in soil samples compared with those from oilfields reported in different studies.

Sample type	Country (Author)		No.	^{40}K (Bq/kg)	^{226}Ra (Bq/kg)	^{228}Ra (Bq/kg)	^{228}Th (Bq/kg)	DR (nGy/h)	AEDR (mSv/yr)
Soil	Albania (this study)	KU	21	297 ± 48	17 ± 2	19 ± 5	20 ± 5	32 ± 5	0.04 ± 0.01
		MA	3	360 ± 42	19 ± 3	33 ± 6	29 ± 5	44 ± 5	0.05 ± 0.01
		BA	3	253 ±75	21 ± 7	29 ± 8	29 ± 9	38 ± 11	0.05 ± 0.01
		HE	5	472 ± 41	30 ± 1	42 ± 6	40 ± 4	58 ± 4	0.07 ± 0.01
	Albania (this study)		32	**326 ± 83** (204 – 535)	**20 ± 5** (12 – 32)	**25 ± 10** (11 – 51)	**25 ± 9** (11 – 44)	**38 ± 11** (32 – 58)	**0.05 ± 0.01** (0.04 – 0.07)
	Tunisia [*Hrichi et al.*, 2013]		1	**176 ± 1**	**9 ± 0.1**	**11 ± 0.1**[a]		**18 ± 0.2**	**0.022**
	Kuwait [*Abdullah et al.*, 2013]		47	(191 – 296)	(12 – 25)	(9 – 16)[a]		-	-
	Nigeria [*Avwiri and Ononugbo*, 2012]		12	**263 ± 10** (134 – 395)	**30 ± 1** (16 – 52)	**17 ± 1**[a] (10 – 34)		**35** (23 – 47)	**0.04** (0.03 – 0.06)
	Nigeria [*Jibiri and Amakom*, 2010]		9	**129 ± 70** (MDA – 248)	**76 ± 34** (30 – 122)	**21 ± 6**[a] (12 – 29)		**53 ± 18** (25 – 73)	**0.06 ± 0.02** (0.03 – 0.09)
	Canada [*Saint-Fort et al.*, 2007]		21	-	(10 - 10×10^3)	(7 – 260)	(MDA – 10)	-	-
	Egypt [*Shawky et al.*, 2001]		4	(MDA - 45×10^3)	(18×10^3 - 438×10^3)	(35×10^3 - 987×10^3)	(MDA – 9×10^3)	-	-
Sludge	Albania (this study)	-	3	348 ±115	19 ± 4	22 ± 4	23 ± 6	36 ± 8	0.04 ± 0.01
		MA	1	314 ± 18	18 ± 3	22 ± 6	25 ± 3	35 ± 6	0.04 ± 0.01
		BA	2	175 ± 89	20 ± 11	21 ± 7	13 ± 1	29 ± 3	0.04 ± 0.01
Oil-sand	Albania (this study)	KU	10	549 ± 12	23 ± 2	23 ± 2	24 ± 3	47 ± 2	0.06 ± 0.01
		MA	2	366 ± 49	12 ± 2	14 ± 4	12 ± 4	29 ± 2	0.04 ± 0.01

[a]Reported as 232Th

Radium isotopes are generally unsupported in formation water, and because a fraction of them can precipitate with oil-sands during oil extraction, an increase in concentration and disequilibrium in the decay chain can occur. The disequilibrium in the ^{228}Ra decay segment was studied in terms of the ratio between the activity concentrations of ^{228}Th and ^{228}Ra (Figure 4.4). We observed ratio values systematically greater than unity; however, this cannot be considered a strong evidence of disequilibrium within the standard uncertainties. The ratios between the activity concentrations of ^{228}Ra/^{228}Th for soil, sludge and oil-sand samples (the last will be discussed below) and the corresponding goodness of the fit, expressed in terms of reduced χ^2 reported in parentheses, are 1.02 ± 0.07 (χ^2 = 0.5), 0.99 ± 0.20 (χ^2 = 3.9) and 1.05 ± 0.09 (χ^2 = 1.6), respectively. We also observe in this case ratio values close to unity for both sludge and oil-sand samples. However, in the context of the environmental legacy issue, only

^{226}Ra is of long-term concern because after 25 years only approximately 5% of ^{228}Ra remains, but the evaluation of secular equilibrium conditions is beyond the capacity of the MCA_Rad system.

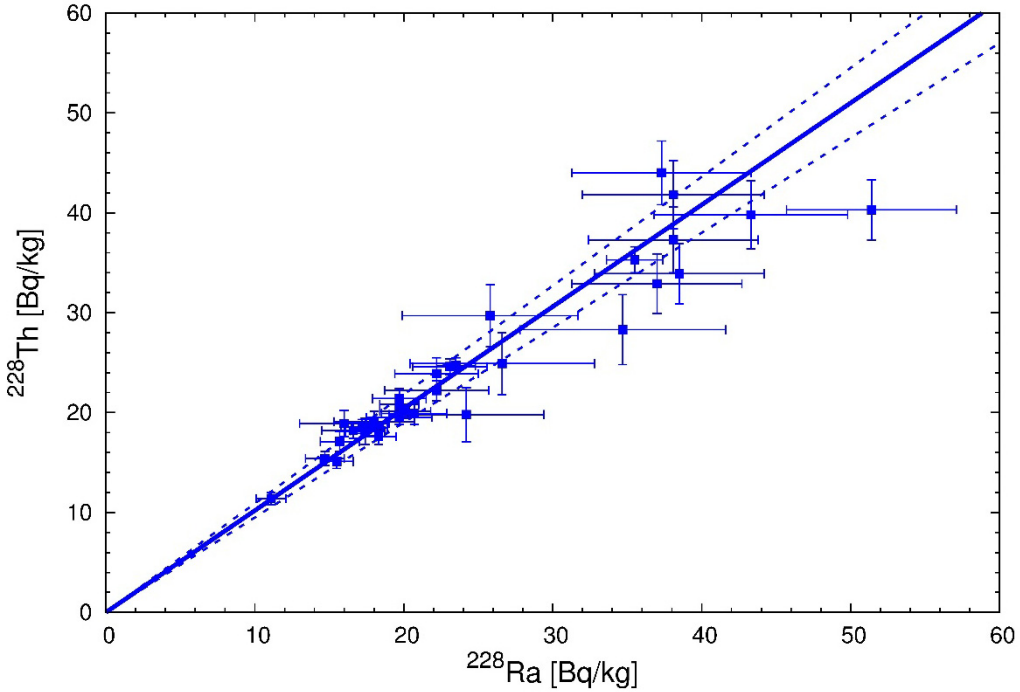

Figure 4.4 ^{228}Th/^{228}Ra activity concentration ratios for the soil samples. The linear fit function corresponds to ^{228}Th/^{228}Ra = 1.02 ± 0.07, with a reduced χ^2 value of 0.5.

The highest concentrations of ^{40}K, ^{226}Ra, ^{228}Ra and ^{228}Th are systematically observed in the HE oilfield, while the lowest ones in the KU oilfield. The KU and MA oilfields belong to the same hydrographic basin, located in the upstream and downstream sectors of the basin, respectively. This is confirmed by the presence of round pebbles with dimensions on the order of centimeters in the KU oilfield which are not present in fine grain soils of the MA oilfield. The higher concentration of ^{228}Ra and ^{228}Th observed in the sediments of the MA oilfield with respect to that of the KU oilfield may be correlated to a selective mechanical deposition, which could be observed in placer deposits. Indeed, as reported by [*Ostrosi et al.*, 1998], heavy mineral placers are exploited along the Adriatic Sea's shore. However, the higher activity concentrations observed in the HE oilfield can be a consequence of either different host rocks or differences in the geomorphological structure (slope debris) with respect to the KU and MA oilfields. Indeed, the genetic processes of soils originated on carbonate substrates tend to enrich the sediments, in particular with uranium and thorium; this may be the case for the soils from the HE oilfield [*Greeman et al.*, 1999].

^{137}Cs was observed only in the soil samples and with highly variable concentrations: the average concentration is 6 ± 4 Bq/kg in the KU oilfield, 14 ± 6 Bq/kg in the BA oilfield, 9 ± 9 Bq/kg in the HE oilfield and 15 ± 7 Bq/kg in the MA oilfield. Indeed, for undisturbed soils with a high presence of minerals, the vertical migration of ^{137}Cs is rather slow, and a greater fraction of activity concentration is expected in the topsoil (0–10 cm) [*UNSCEAR*,

2008]. The non-presence of ^{137}Cs in oil-sands can be used as a tracer to discriminate them from soil samples.

The activity concentration ratios (±1σ uncertainty) for $^{228}Ra/^{226}Ra$, $^{226}Ra/^{40}K$ and $^{228}Ra/^{40}K$ (Figure 4.5) (hereafter, assuming secular equilibrium, reported as Th/U, U/K and Th/K, respectively) are summarized in Table 4.2 and studied to understand the hidden geochemical patterns of the analyzed samples. We observe in general that the activity concentration ratios in the soil samples show a specific signature (confirmed at ±1σ) over the oilfield reservoirs, which allows us to attribute a clastic sedimentary origin to them (main constituents of the PAD unit, see Figure 4.1). Indeed, the measured activity concentration ratios Th/U, U/K and Th/K are comparable with the average activity concentration ratios in sandstone, which are 1.06, 0.062 and 0.068, respectively, and in shale, which are 1.07, 0.055 and 0.058, respectively [*Van Schmus*, 2013]. This is reasonable as the soils originated in alluvial deposits overlaying the PAD unit.

The oil-sand samples (discussed later) also have similar ratios (Figure 4.5); collectively interpreting the results from the oil-sands is relatively complex due to their different lithological origins. In the case of the MA oilfield, the activity concentration ratios (Figure 4.5) indicate an increase in Th and K with respect to an average carbonate rock, characterized by Th/U, U/K and Th/K values equal to 0.25, 0.32 and 0.082, respectively [*Van Schmus*, 2013]. This can be possibly ascribed to the lithological characteristics of the MA reservoir rock, which has a significant amount of terrigenous minerals (ION unit described in Figure 4.1). In the case of the KU oilfield, the activity concentration ratios are particularly similar to sandstone rocks [*Van Schmus*, 2013]; the slight difference can be attributed to the highly heterogeneous composition of the sandstone rocks.

Table 4.2 The ratio *m* (±1σ uncertainty expressed in significant digits) of $^{228}Ra/^{226}Ra$, $^{226}Ra/^{40}K$, $^{228}Ra/^{40}K$ in soil, sludge and oil-sand samples obtained through the reduced χ^2 minimization method. The goodness of the fit is expressed in terms of reduced χ^2.

Sample type	**$^{228}Ra/^{226}Ra$**		**$^{226}Ra/^{40}K$**		**$^{228}Ra/^{40}K$**	
	***m* (±1σ)**	**χ^2**	***m* (±1σ)**	**χ^2**	***m* (±1σ)**	**χ^2**
Soil	1.14 (18)	2.6	0.057 (7)	6.1	0.066 (13)	4.0
Sludge	1.27 (23)	3.1	0.049 (11)	15.3	0.065 (13)	4.0
Oil-sand	1.03 (3)	0.2	0.040 (4)	6.0	0.042 (4)	2.2

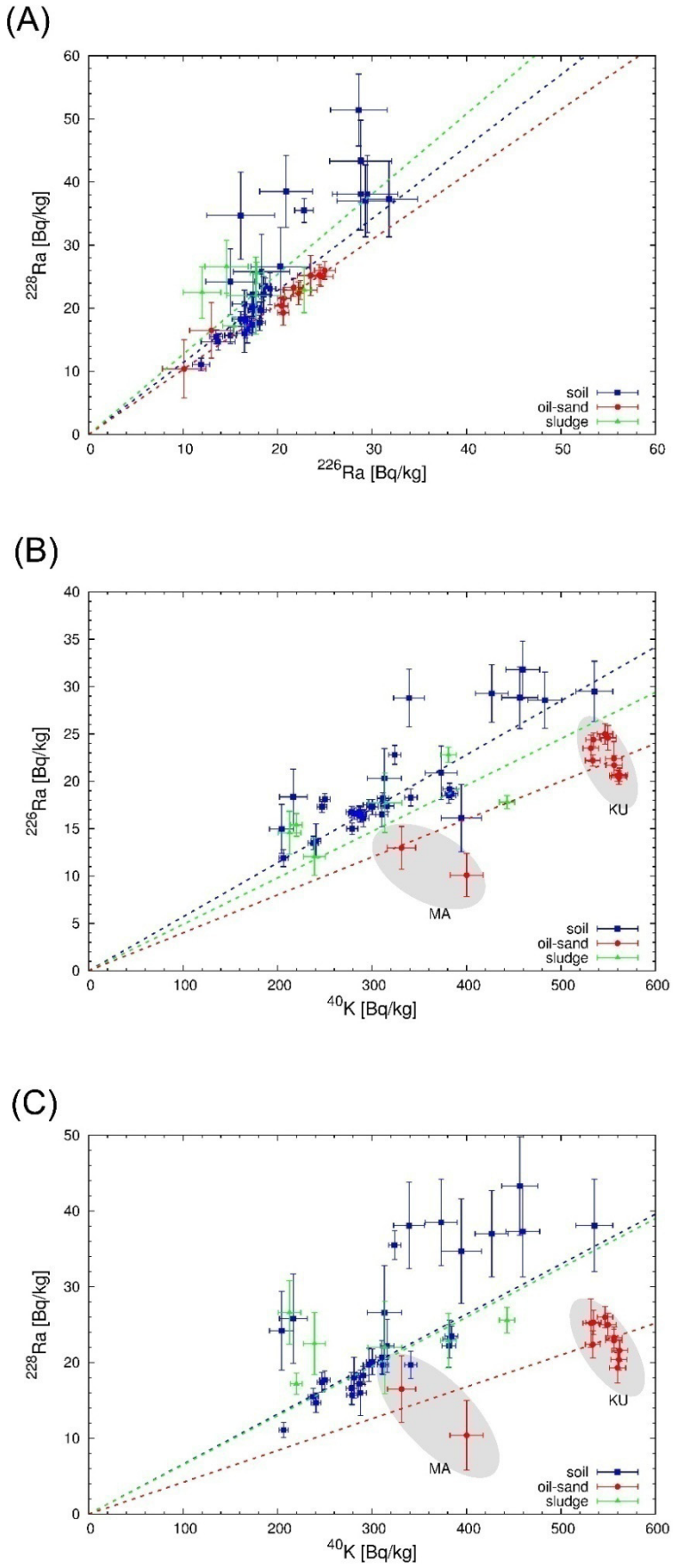

Figure 4.5 (A) ^{228}Ra/^{226}Ra, (B) ^{226}Ra/^{40}K and (C) ^{228}Ra/^{40}K activity concentration ratios for soil (blue), oil-sand (red) and sludge (green) samples

4.5.2 Activity concentrations in sludge samples

The averages of the activity concentrations of ^{40}K, ^{226}Ra, ^{228}Ra and ^{228}Th in the sludges are found to be comparable, within the uncertainty, for all the oilfields investigated (Table 4.1). As the sludges are a mixture of crude oil, oil-sand and soil, the variability observed in their activity concentrations is difficult to understand as it depends on the mixing fractions. However, we can state that a significant fraction of crude oil will result in a decreasing radioactivity level because the concentrations of radionuclides are very low. In the case of sludge samples from the KU oilfield, we observe a slight increase in the activity concentrations of ^{40}K, ^{226}Ra, ^{228}Ra and ^{228}Th with respect to the soil samples; this is probably due to the relatively high concentrations of oil-sand in the sludge samples. This assumption is confirmed in the case of the MA oilfield, where we observe a slight decrease in the activity concentrations of ^{40}K, ^{226}Ra, ^{228}Ra and ^{228}Th with respect to the soil samples due to the relatively low concentrations of oil-sand in the sludge samples.

4.5.3 Activity concentrations in oil-sand samples

The activity concentrations of ^{40}K, ^{226}Ra, ^{228}Ra and ^{228}Th in the oil-sand samples from the KU and MA oilfields differ significantly (within 2σ uncertainty) (Table 4.1). The two oilfields can be easily recognized using the patterns of the ^{226}Ra/^{40}K and ^{228}Ra/^{40}K ratios (Figure 4.5 B and 4.4 C). The discrimination between the two oilfields has also been achieved via a mineralogical analysis (Table 4.3) performed for oil-sand samples collected in different wells from the KU and MA oilfields. These results confirm that the KU oilfield reservoir is located in sandy lenses belonging to the PAD (absence of dolomite and very low calcite, along with the presence of muscovite and chlorite and an increase in K-feldspar), while the MA oilfield reservoir is located in the fractured limestones of the ION (presence of calcite and dolomite) (see Figure 4.1). This interpretation is also supported by the observation of a higher radioactivity content in the KU oilfield samples (more radioactive sandy lenses) with respect to that of the MA oilfield (less radioactive limestones) (Figure 4.5).

Table 4.3 Mineral percentage content measured by X-ray diffractometry and activity concentration measured by the MCA_Rad system for oil-sand samples collected in the KU and MA oilfield. The uncertainty associated to the mineralogical analysis is approximately 10-15% for Quartz and 20-30% for the other minerals (minerals estimated with an uncertainty greater than 30% are reported as <5). The Limit of Detection (LD) for XRD measurements is 1%.

Sample ID	Qtz	Pl	Kfs	Cal	Dol	Ms	Chl	^{40}K (Bq/kg)	^{226}Ra (Bq/kg)	^{228}Ra (Bq/kg)	^{228}Th (Bq/kg)
KU_OS1	40	20	6	<5	<LD	15	7	534 ± 8	22 ± 1	22 ± 2	25 ± 2
KU_OS5	44	20	13	<5	<LD	8	8	547 ± 8	25 ± 1	26 ± 1	29 ± 2
KU_OS6	43	20	8	<5	<LD	10	6	560 ± 9	21 ± 1	19 ± 2	21 ± 1
MA_OS1	60	12	8	12	<5	<LD	<5	331 ± 15	13 ± 2	16 ± 4	9 ± 2
MA_OS2	55	11	8	20	<5	<5	<LD	400 ± 18	10 ± 2	10 ± 5	14 ± 2

Qtz. Quartz, *Pl.* Plagioclase, *Kfs.*K-Feldspar, *Cal.*Calcite, *Dol.* Dolomite, *Ms.* Muscovite, *Chl.*Chlorite

The KU oil-sand samples are characterized by a significant terrigenous content (deep-sea sediments transported to the oceans by rivers from land sources) made up of quartz, feldspars, mica, chlorite and a very low amount of calcite. The presence of chlorite and muscovite minerals confirms the geodynamic model that predicts a dismantling of the magmatic rocks belonging to the Inner Units. In particular, the chlorite could be formed by the alteration of other silicate minerals that contain Mg and Fe (e.g., olivine, augite (pyroxene), hornblende, and biotite), which is typical of ophiolitic suites (deep-sea marine sediments overlying, from top to bottom, pillow basalts, sheeted dikes, gabbro, dunite, and peridotite). The percentages of Quartz, Feldspar and Lithics (QFL) (plotted in the ternary diagram of Figure 4.6) measured in 3 samples of KU oil-sand are comparable with those reported in [*Dickinson*, 1985], which correspond to mineralogical signatures typical of terrigenous Cenozoic sandstones deposited in different sites. Referring to the QFL triangle of [*Dickinson*, 1985], we can affirm that the oil-sand samples can be related to a source rock environment, such as a "dissected arc", which is connected to the exposure of volcanic and basement rocks (in this case the ophiolitic rocks of the Inner unit). Because the reservoir is formed by sands containing many minerals of magmatic derivation (muscovite, chlorite and feldspars), this may confirm the higher amount of radionuclides with respect to MA.

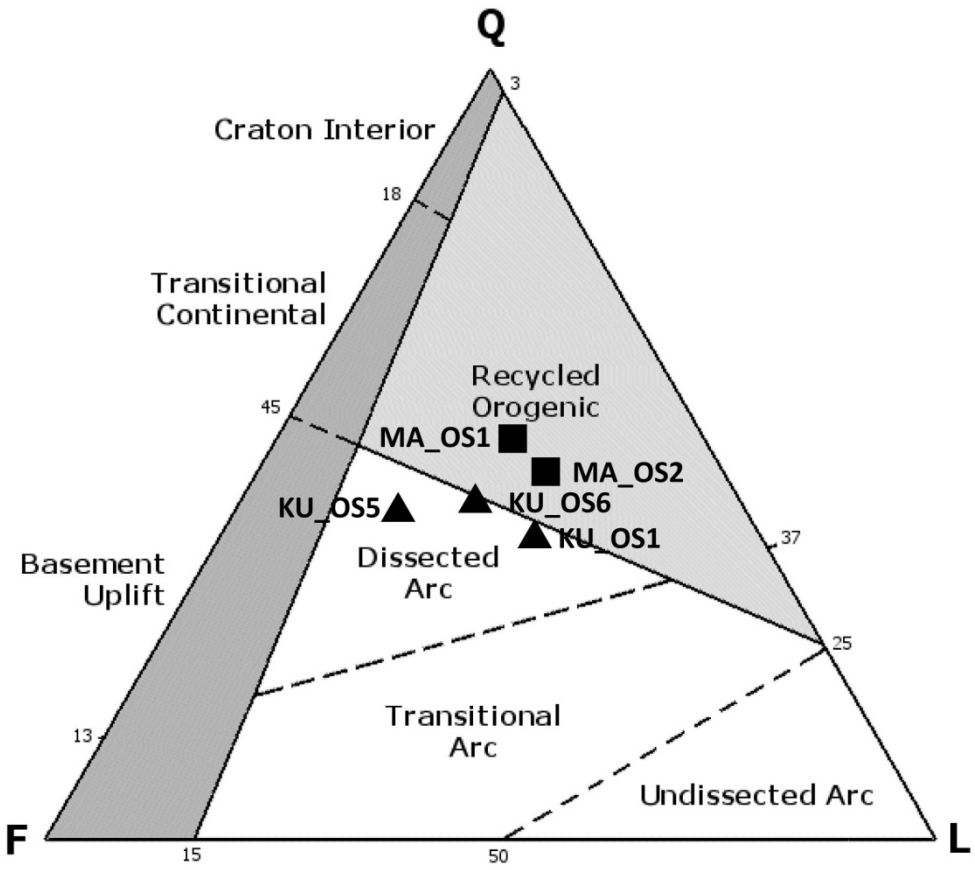

Figure 4.6 Quartz, Feldspar and Lithics ternary diagram after [*Dickinson*, 1985]. The studied oil-sand plot mainly in the dissected arc and recycled orogenic fields for KU (triangles) and MA (rectangles) oilfields.

In the MA oilfield, the depth provenance of oil-sand is greater with respect to that of the KU oil-sand samples due to the geological structure and to the existence of deep stratigraphic traps. In particular, the MA oil-sand samples come from a reservoir that is located near a planar discontinuity called a "major unconformity" (dashed line in Figure 4.3 Sect. BB'). The higher calcite content (Table 4.3) of both MA oil-sand samples indicates that the reservoir is located in the carbonate source rock (ION) or near the interface with overlying molasses sediments (PAD) (see Figure 4.1). The data from MA and KU in the QFL (Quartz, Feldspar and Lithics) confirm our analysis. In particular, the MA oil-sands are the result of recycled orogens. The deformation and uplift of supracrustal strata include sedimentary and volcanic rocks exposed in varied fold-thrust belts of orogenic regions. The lower radioactivity content fits perfectly with the geodynamic framework and the mineralogical nature of the oil-sand reservoir. In particular, the source rock with clear calcite content, which is typical for the ION, seems to lack radionuclides, making the extracted oil-sands a negligible source of NORM.

4.6 Radiological assessment

The absorbed dose rate (*DR*) in air from external gamma radiation at 1 m above ground level due to the presence of uniformly distributed natural radionuclides in measured soils is calculated according to [*UNSCEAR*, 2000]:

$$DR\ (\text{nGy/h}) = 0.0417A_K + 0.462A_U + 0.604A_{Th} \quad (4.1)$$

where A_K, A_U, and A_{Th} are the activity concentrations (in Bq/kg) for ^{40}K, ^{238}U (as ^{226}Ra) and ^{232}Th (as ^{228}Ra), respectively. Secular equilibrium was assumed for the dose calculation. The average outdoor absorbed dose rate (DR) (at $\pm 1\sigma$ uncertainty) in the KU oilfield area is 32 ± 5 nGy/h; in MA 44 ± 5 nGy/h; in BA 38 ± 11 nGy/h; and in HE 58 ± 4 nGy/h (Table 4.1). This dose rate is lower than or comparable to the population weighted average absorbed dose rate in outdoor air from terrestrial gamma radiation (60 nGy/h) [*UNSCEAR*, 2000].

The average outdoor absorbed dose rates (at $\pm 1\sigma$ uncertainty) from the sludge and oil-sand samples are reported in Table 4.1, which range between 27 and 50 nGy/h. Assuming the worst case scenario in the KU oilfield, which corresponds to oil-sands uniformly distributed over the topsoil, the absorbed dose rate was estimated to increase on average 50%, i.e., to a maximum value of 47 ± 2 nGy/h. In the same hypothesis, we observe a decrease in the absorbed dose rate for the other oilfields. Therefore, negligible radiation exposure to workers in the oil and gas industry can occur from increased gamma dose rates due to the relatively higher radioactivity content in the oil-sand residues in the KU oilfield.

The radiological hazard for workers and populations living in the oilfield areas is evaluated in terms of the Annual Effective Dose Rate (AEDR). The evaluation of the AEDR

was performed by adopting an outdoor time occupancy factor equal to 20% and a conversion factor of 0.7 (Sv/Gy), which accounts for the dose rate's biological effectiveness in causing damage to human tissues:

$$AEDR\ (\text{mSv/yr}) = DR \times 10^{-6}\ (\text{mGy/h}) \times 8760\ (\text{h/yr}) \times 0.7\ (\text{Sv/Gy}) \times 0.2 \qquad (4.2)$$

The results concerning the radiological assessment are summarized in Table 4.1. The annual outdoor effective dose rate of 0.05 ± 0.01 mSv/y associated to the radioactive content in soils is lower than the worldwide annual effective dose value of 0.07 mSv/y, as reported by [*UNSCEAR*, 2000]**.** Considering the worst-case scenario described above, we predict an increase in the *AEDR* of approximately 0.02 ± 0.01 mSv/y for the KU oilfield. This value is negligible considering the recommended excess limit of an effective dose for the local population (1 mSv/y). Therefore, in the KU, MA, BA and HE oilfields, there is no concern from a radiological point of view.

4.7 Final remarks

This study is the first screening campaign on the identification and monitoring of oil and gas industry processes involving NORMs. Accordingly, the KU, MA and BA-HE oilfields are chosen as pilot study areas, where secondary recovery techniques for oil extraction have recently been introduced. In particular, soil (N = 32), sludge (N = 6), oil-sand (N = 12), produced water (N =1) and crude oil (N = 1) samples are measured using the gamma-ray spectrometry method. The results reveal baseline information for local environmental legacy policies and the implementation of EU legislations.

The average activity concentrations (± standard deviations) of ^{40}K, ^{226}Ra, ^{228}Ra and ^{228}Th in the soil samples collected in the main oilfields in Albania are 326 ± 83 Bq/kg, 20 ± 5 Bq/kg, 25 ± 10 Bq/kg, 25 ± 9 Bq/kg and 6 ± 4 Bq/kg, respectively. The results for the soil samples are found to be comparable with data reported in several studies on activity concentrations in soil samples from oilfields. The activity concentrations in the soil samples show great variability, which can be attributed mainly to the geological and geochemical characteristics of the different areas and in a lower grade probably to human activities, such as the release of oil-sands and sludges. The impact caused by the contamination of the investigated soils collected in the surroundings of Albanian oilfields by crude oil and produced water is negligible from a radiological point of view, as the activity concentrations measured in the produced water and crude oil samples are found to be very low (below MDA). Geological and geochemical arguments are used to describe the observed activity concentrations in different oilfields. The higher radioactivity content observed in the soils from the HE oilfield with respect to that from the KU oilfield was attributed to both the carbonate origin of the host rocks and to different geomorphological structure. Indeed,

bibliographic studies confirm that soils that originate on carbonate substrates tend to enrich the sediments in uranium and thorium. In the case of the KU and MA oilfields, which are part of the same hydrographic basin, the increasing trend for the activity concentrations of thorium progenies gives an indication on the selective deposition and, as supported by bibliographic studies, on the occurrence of heavy placer deposits along the Adriatic Sea's shore. According to the Th/U, U/K and Th/K ratios, the origin of the soil samples can be reasonably connected to alluvial deposits overlaying the PAD unit.

The activity concentrations in the sludge samples are reasonably understood when considering sludges as a mixture of soil, crude oil, and oil-sand. This study is the first one reporting results on the activity concentrations in oil-sand samples generated during heavy oil extraction. The average activity concentrations of the oil-sand samples measured in the KU and MA oilfields differ at 2σ level, and are equal to 549 ± 12 Bq/kg (^{40}K), 23 ± 2 Bq/kg (^{226}Ra), 23 ± 2 Bq/kg (^{228}Ra) and 24 ± 3 Bq/kg (^{228}Th) in the KU oilfield and 366 ± 49 Bq/kg (^{40}K), 12 ± 2 Bq/kg (^{226}Ra), 14 ± 4 Bq/kg (^{228}Ra) and 12 ± 4 Bq/kg (^{228}Th) in the MA oilfield. Based on the mineralogical analysis of the oil-sand samples, we confirm bibliographic geophysical evidence regarding the origin of the oilfield reservoirs: sandy lenses located in the PAD unit for the KU oilfield and fractured limestone located in the ION unit for the MA oilfield. Indeed, the KU oil-sand samples are characterized by terrigenous contents with very low amounts of calcite, and the presence of chlorite and muscovite minerals confirms the geodynamic model that predicts a dismantling of magmatic rocks in the Inner Unit. On the other side, the MA oil-sands confirm their connection to the geological structure due to the higher amount of calcite. This different origin is also confirmed from the activity concentration results, as the KU samples containing many minerals from magmatic deviation show higher activity concentrations of ^{40}K, ^{226}Ra, ^{228}Ra and ^{228}Th with respect to the MA samples, which originate from carbonate rocks known to have a lower radioactive content. Based on this geological framework, the future radiological assessment of other fields in the region can be strategically planned to focus on the investigation of the oil-sands from Neogene molasses deposits.

The absorbed dose rate and annual effective dose rate were calculated to assess the radioactive exposure of workers or members of the public due to NORMs produced in the oil and gas industry, in compliance with EU recommendation. Assuming the worst case scenario, i.e., that sludge and oil-sands are uniformly distributed over the topsoil, the absorbed dose rate and the *AEDR* of the KU oilfield were estimated to increase on average by a maximum of 50%, i.e., to a maximum value of 47 ± 2 nGy/h or the corresponding 0.06 ± 0.01 mSv/y. In the other investigated oilfields, the impact of industrial processes has been estimated to be negligible. Considering the worldwide annual effective dose value of 0.07 mSv/y associated to the radioactive content in soils and the recommended excess limit of an effective dose for the local population of 1 mSv/y, we conclude that there is no concern from a radiological point of view in the KU, MA, BA and HE oilfields.

.

The content of this chapter is based on the following publication:

Xhixha G., Baldoncini M., Callegari I., Colonna T., Hasani F., Mantovani F., Shala F., Strati V. and Xhixha Kaçeli M. *A century of oil and gas exploration in Albania: Assessment of Naturally Occurring Radioactive Materials*. Chemosphere (2013) 139(0) 30-39.
DOI: 10.1016/j.chemosphere.2015.05.018

Chapter 5

A 3D geophyisical and geochemical model of the crust surrounding the Sudbury Neutrino Observatory (SNO+) for the prediction of geoneutrino flux

The geophysical and geochemical modeling of the crust, especially of the portion near to the detector, is certainly one of the most thorny charge for the scientists of the geoneutrino community. This is what was emphasized during the recent International workshop on KamLAND Geoscience (January 2015, Tokyo) and the Neutrino Geoscience Conference (June 2015, Paris) in which I had the privilege to participate. During these fruitful debates, a lot of questions arose about the strategies to follow for the construction of a model for the prediction of geoneutrino signal. The choice of a suitable spatial resolution, the integration of appropriate gephysical inputs and the compilation of a coherent geochemical dataset are just some of the crucial aspects for a reliable estimation of the geoneutrino signal and above all for the evaluation of the uncertainties. When in the next geoneutrino data will be available for several sites and looking forward the reduction of experimental uncertainties, improving prediction of the crustal geoneutrino is mandatory for discriminate the mantle signal and in turn to get insights about the composition of Earth's interior.

In this Chapter are described the methodology and the results of the construction of a detailed 3-D model of the regional crust centered at SNO+ from compiled geological, geophysical, and geochemical information. This study represented for me the opportunity to face the problematic aspects of the geoneutrino modeling and to propose advanced solutions taking advantages from the experiences developed in the geostatistic field and discussed in the previous chapters.

My main tasks consisted in the construction of the geophysical model that led to define the geometry of the lower and middle crust and of the main reservoirs of the upper crust. Thanks to application of the Ordinary Kriging on the seismic data inferred from the refraction and reflection cross sections, I provided the depth maps of the geophysical discontinuities together with the map of the uncertainty of the estimates. So, for the first time the masses of the main crustal reservoirs containing U and Th are estimated together with their uncertainties in the region surrounding SNO+. Moreover, the estimation of the geoneutrino signal comes from a refined evaluation of the different sources of uncertainties that permitted to individuate the major source of uncertainty, namely the lithologic unit including the Huronian Supergroup characterized by rocks with a high compositional variability. The recommendation for improving the knowledge of the U and Th content of this

unit is a key result of this study that highlights the necessity to put more stringent constraints on the local contribution to the geoneutrino signal for inferring the Earth's heat budget and chemical composition.

5.1 Background

Geoneutrinos, electron antineutrinos generated during beta decays of radioactive nuclides in the Earth, offer a means to determine the concentrations of heat-producing elements (HPEs, namely U, Th, and K), and hence the total radiogenic heat power of the Earth [*Dye*, 2010; 2012; *Šrámek et al.*, 2012; *Šrámek et al.*, 2013]. A better constraint on the total radiogenic heat power is critical for determining the Earth's heat budget, understanding the power driving plate tectonics, and the thermal and chemical evolution of the planet. Compositional models for the bulk silicate Earth (BSE) differ by a factor of three in U concentration and total radiogenic heat power of the planet [*Turcotte and Schubert*, 2002] [*Javoy et al.*, 2010; *McDonough and Sun*, 1995; *O'Neill and Palme*, 2008]. Geoneutrino data, when available for several sites on the Earth, should be able to define the range of permissible compositional models that describe the BSE.

The physical properties of geoneutrinos have been reviewed in the literature [e.g., *Dye*, 2012; *Fiorentini et al.*, 2007; *Šrámek et al.*, 2012]. The current detection mechanism is the inverse beta reaction, where an anti-neutrino combines with a free proton to produce a positron and a neutron, which are detected by prompt and delayed light flashes recorded in large underground liquid scintillation detectors. This reaction is sensitive to geoneutrinos produced from four beta decays: two each in the ^{238}U and ^{232}Th chains; all other geoneutrinos have energies lower than the threshold level (1.806 MeV) that is required to initiate the reaction. Geoneutrinos originating from U and Th decay chains can be distinguished based on their different energy spectra, e.g., only the ^{238}U chain can produce geoneutrinos with energy >2.25 MeV. KamLAND (Kamioka Liquid scintillator ANtineutrino Detector) in Japan [*Araki et al.*, 2005; *Gando et al.*, 2013; *Gando et al.*, 2011] and Borexino in Italy [*Bellini et al.*, 2010; *Bellini et al.*, 2013] are the two detectors that are currently accumulating geoneutrino events, and the experimental results have provided some constraints on the radiogenic heat power from U and Th in the Earth. The SNO+ detector will come on-line in 2014. This kiloton scale detector, a redeployment of the former Sudbury Neutrino Observatory (SNO) at SNOLAB, is located in Ontario, Canada, and will have a higher signal-to-noise ratio for geoneutrino events compared to other operating detectors [*Chen*, 2006]. SNO+ will provide new data on the geoneutrino signal mainly originating from U and Th in the surrounding continental crust.

[*Huang et al.*, 2013] developed a global reference model that predicted the geoneutrino signal from the crust and mantle. Using this model they predicted the geoneutrino flux at KamLAND, Borexino, SNO+, and Hanohano, the latter a proposal for a sea floor

detector. The predicted signal from the lithosphere at SNO+ was estimated at $36.7^{+7.5}_{-6.3}$ TNU (a Terrestrial Neutrino Unit is one geoneutrino event per 10^{32} target protons per year), of which $34.0^{+6.3}_{-5.7}$ TNU originates from the crust. The far field crust (FFC; defined as the remainder of the crust after removing the closest six 2° × 2° crustal tiles near the detector) contributes $15.1^{+2.8}_{-2.4}$ TNU, and the regional continental crust (closest six tiles) is the dominant geoneutrino source, contributing ~19 TNU. The geoneutrino signal from the mantle at SNO+ is predicted to be between 2 to 16 TNU [*Šrámek et al.*, 2013].

Since SNO+ will accumulate statistically significant amounts of geoneutrino data in the coming years, the calculated signal that is predicted to be derived from the lithosphere can be subtracted from the experimentally determined total geoneutrino signal to estimate the mantle contribution. Such a calculation is key to resolving different BSE compositional models [*Dye*, 2010; *Fogli et al.*, 2012]. It is therefore useful to construct a regional scale reference model based on detailed geological, geochemical and geophysical studies in order to calculate the geoneutrino signal and its uncertainties originating from the local crust. The construction of such a regional reference model is the primary aim of this study.

5.2 Constructing the model

We use the published 1:5,000,000 scale Geological Map of North America [*Reed et al.*, 2005] to describe the surface geological characteristics in the six 2°× 2° crustal tiles centered at SNO+ (outlined in Figure 5.1 including lithologies, boundaries between different geological terranes/provinces, and their relative proportions. Refraction seismic surveys carried out in this region provide information on the crustal velocity structure and thickness [*Epili and Mereu*, 1991; *Mereu et al.*, 1986; *Musacchio et al.*, 1997; *John A. Percival and West*, 1994; *Winardhi and Mereu*, 1997], whereas reflection seismic surveys and receiver function analysis provide additional constraints on the Moho depth (Figure 5.2) [*Brown et al.*, 1982; *Eaton et al.*, 2006; *Spence et al.*, 2010]. All of the above information is integrated into a 3-D regional crust model. In this model, the layer with P-wave velocities (Vp) between 6.6 and 6.8 km/s is defined as the middle crust, and the underlying layer having Vp between 6.8 and 8.0 km/s is the lower crust.

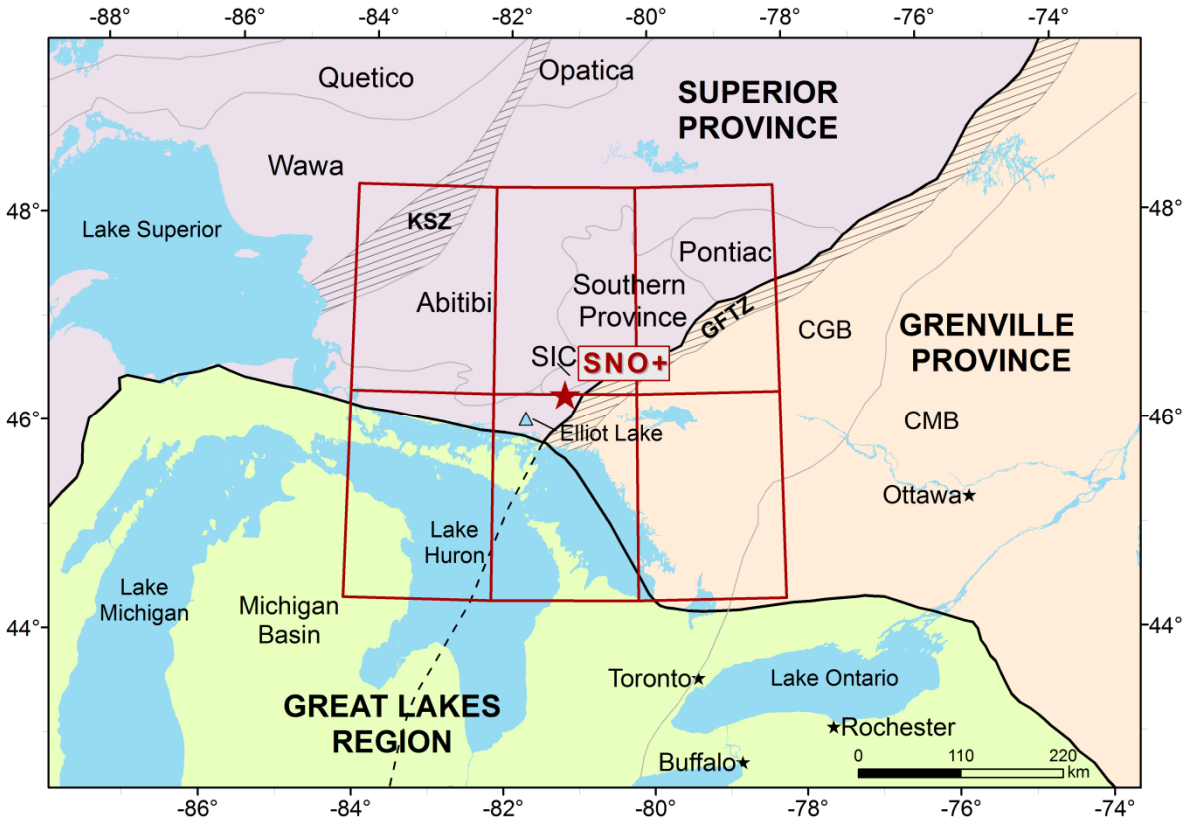

Figure 5.1 Schematic map of the region around Sudbury, where the SNO+ detector (red star) is located. The six 2°× 2° tiles (outlined by red lines) centered at SNo+ cover the area from which we build the 3-D regional crustal model. Light black lines show the major terrane boundaries within the Superior Province, which is separated with the Grenville Province by the Grenville Front Tectonic Zone (GFTZ). The Great Lakes region is covered by Paleozoic sediments, extending to the Great Lakes Tectonic Zone (GLTZ) in the north. The Kapuskasing Structural Zone (KSZ) is a prominent metamorphic zone in the Superior Province.

The upper crust is subdivided into seven different lithologic units based on surface exposures (Figure 5.3): 1) tonalite and tonalite gneiss of the Wawa-Abitibi sub-provinces, 2) Archean felsic intrusive rocks (granite, granodiorite, etc.), 3) gneissic rocks in the Central Gneiss Belt of the Grenville province, 4) Huronian Supergroup sedimentary to metasedimentary rocks, 5) volcanic/metavolcanic rocks in the Abitibi sub-province, 6) the Sudbury Igneous Complex (SIC), and 7) Paleozoic sediments in the southern portion of the study area.

Published databases of litho-geochemical studies performed by the Ontario Geological Survey (OGS) provide high quality U and Th abundance data, determined by ICP-MS or INAA, for most of the major lithologies in the region. The composition of volcanic/metavolcanic rocks in Abitibi is compiled mostly from data in GEOROC. The lake sediments in the Ontario area are assumed to have the same U and Th abundances as the Paleozoic sediments that cover the Great Lakes region. Data from the published literature for the chemical compositions of major lithologies in the study area that are not compiled by GEOROC are also incorporated into the model. Direct samples of the deep crust are limited (lower granulite facies rocks are only exposed in the Kapuskasing Structural Zone, which is at the northwest corner of the six tiles). Therefore, we follow the approach described by [*Huang*

et al., 2013], which is based on previous studies [e.g., *Christensen and Mooney*, 1995; *Rudnick and Fountain*, 1995] that link the seismic velocity data from refraction seismic surveys with the chemical composition of global amphibolite and granulite facies rocks [*Huang et al.*, 2013], in order to infer the U and Th abundances in the middle and lower crust in the region.

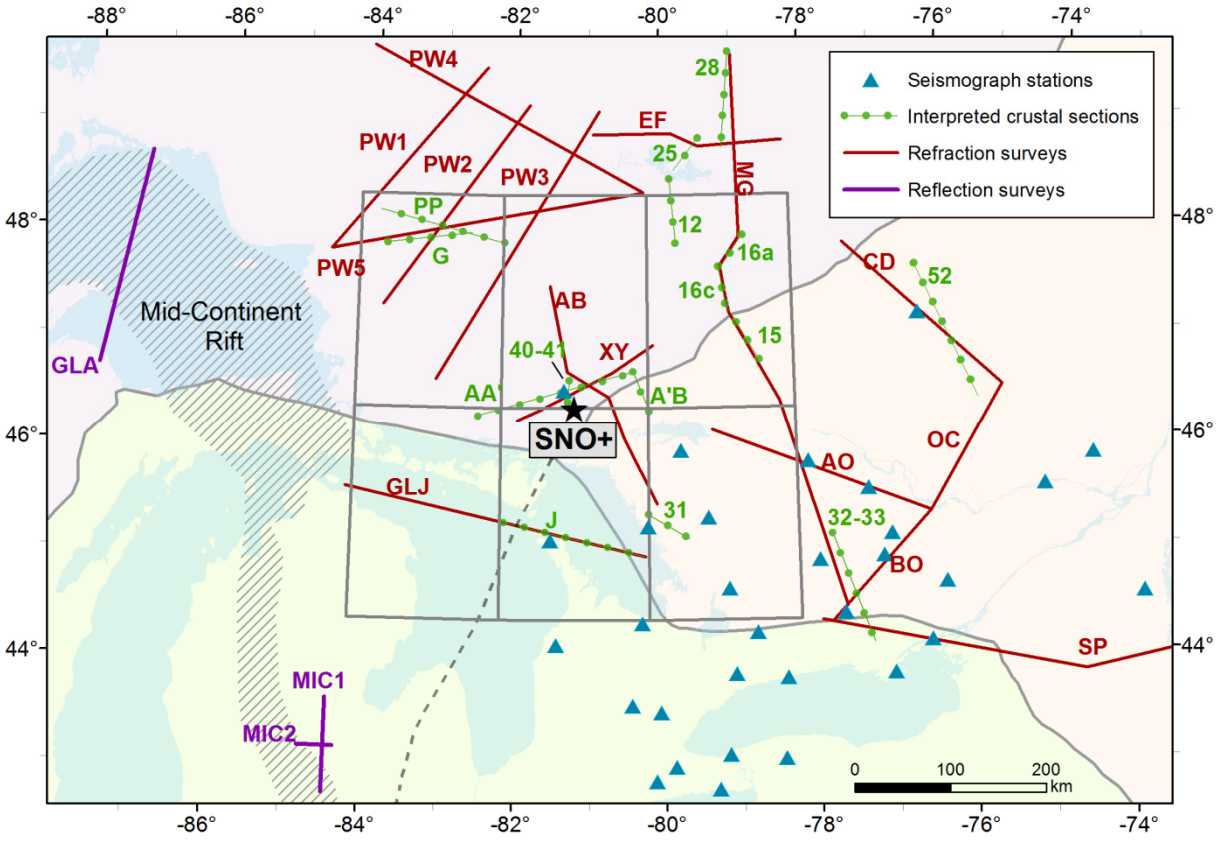

Figure 5.2 Geophysical constraints in the 3-D crustal model are from local refraction surveys (red lines), reflection surveys (purple lines), interpreted crustal cross sections (green-dotted lines), and broadband seismometers (blue triangles). Only refraction and reflection surveys provide seismic velocities to determine the boundaries between three crustal layers. Interpreted crustal cross sections are used to cross check our 3-D model.

The 3-D model is constructed based on the physical and chemical (U and Th abundances) properties of the regional crust. From these data, the geoneutrino signal at SNO+, as well as the heat production within the study area are calculated, and the associated uncertainties are propagated using Monte Carlo simulations. The geoneutrino signal from the regional model is compared with previous estimates for SNO+ [*Huang et al.*, 2013]. Heat production and heat flow in our model are compared with heat flow measurements in the area [e.g., *Perry et al.*, 2006]. We also evaluate SNO+'s sensitivity to the mantle geoneutrino signal in order to shed light on Earth's chemical composition.

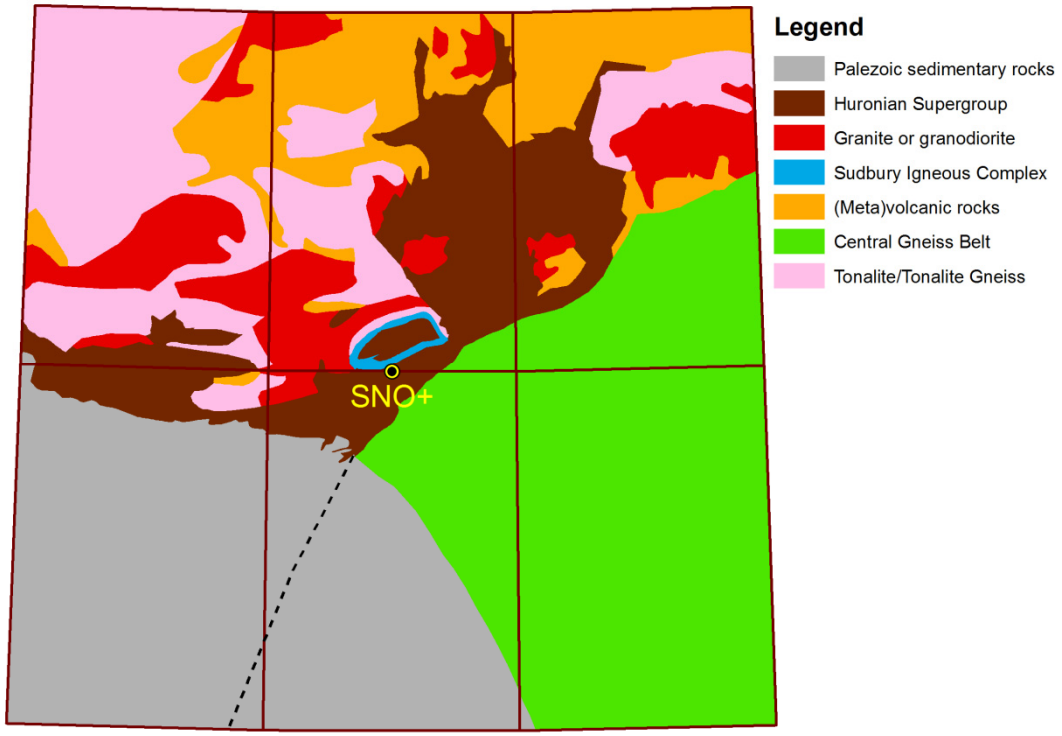

Figure 5.3 Simplified geological map of the six 2°× 2° tiles centered at SNO+. Each color represents a single subreservoir in the upper crust that is assumed to be chemically uniform. The dashed black line is the extension of GFTZ under the Paleozoic sedimentary cover in the Great Lakes region.

5.3 Geology framework of the regional crust

The six 2° × 2° crustal tiles centered at SNO+ (approximately 440 km × 460 km), outlined in Figure 5.1, comprise the study area used to construct the 3-D regional reference model and calculate the resulting regional geoneutrino signal. The SNO+ regional crust includes Precambrian rocks of the southeastern Canadian Shield and Paleozoic sediments of the Great Lakes and Michigan basin. The distribution of the Paleozoic sediments, extending to the Great Lakes Tectonic Zone (GLTZ in Figure 5.1), separates the study area into two distinct portions. The northern portion of the region consists of crystalline rocks of the Neoarchean southeastern Superior Province and the Mesoproterozoic Grenville Province, which borders the southeastern part of the Canadian Shield. The boundary between the Superior Province and Grenville Province is referred to as the Grenville Front Tectonic Zone (GFTZ). The Sudbury Igneous Complex (SIC) and Southern Province are distributed along the GFTZ in the study area (Figure 5.1). The southern portion of the study area is covered by Paleozoic sediments with thicknesses increasing in a southerly direction to the Michigan basin where the total sedimentary cover is up to ~5 km [e.g., *Howell and van der Pluijm*, 1999]. The crystalline basement in the southern region is obscured by this sedimentary cover. In the following sections, the geology of each of these regions is reviewed.

5.3.1 Superior Province

The Superior Province was constructed from fragments of much smaller Archean microcontinents from the Paleoarchean through the Neoarchean and later modified by subsequent collisional events during the Proterozoic. It is one of the world's largest Archean cratons and contains rocks ranging in age from 0.1 to 4.2 Ga. On the basis of lithology, structure, metamorphism, ages, and tectonic events, the Superior Province can be subdivided into several sub-provinces. The Wawa, Abitibi, and Pontiac sub-provinces occur within the six 2° × 2° crustal tiles of our model [e.g., *Benn and Moyen*, 2008; *Card*, 1990; *Pease et al.*, 2008; *J. A. Percival*, 2007]. The following geological descriptions are taken from *Card* [1990] and *J. A. Percival* [2007].

The Wawa sub-province has an east-west extent of about 600 km, extending east towards the Kapuskasing structure zone (KSZ in Figure 5.1). This sub-province is bounded on the southeast by the Early to Middle Proterozoic Southern Province, on the southwest by the Mid-Continent Rift (Figure 5.2), and on the north by the Quetico and Opatica sub-provinces. The southern extent of the Wawa sub-province is obscured by Lake Superior and Paleozoic sedimentary cover. The eastern Wawa sub-province consists of upper amphibolite facies gneiss that continues gradationally into granulite facies in the KSZ. The Wawa sub-province is composed of Neoarchean juvenile crustal additions of submarine volcanic successions of komatiites, tholeiites and andesites that are intruded by tonalite, granodiorite and granite. Foliated to gneissic tonalitic to granodioritic rocks with zircon U-Pb ages around 2.7 Ga are dominant in the eastern border near the KSZ. The gneiss is cut by younger granodioritic to granitic plutons.

The Abitibi sub-province is the world's largest Archean granite-greenstone belt. The sub-province is bounded on the west by the KSZ and on the east by the GFTZ, a zone of faulting that separates the Superior and Grenville provinces. The southern boundary of the Abitibi sub-province is the GLTZ. The Abitibi region comprises mafic to felsic volcanic/metavolcanic rocks concentrated in the central Abitibi greenstone belt. Tonalite gneiss forms batholithic complexes in and around greenstone belts and is intruded by granitic to granodioritic plutonic rocks.

The small Pontiac sub-province is bounded on the south and east by the GFTZ and on the north by the Abitibi sub-province. It is a Late Archean terrane comprised of lesser exposures of metasediments intruded by tonalite, granodiorite, quartz syenite and granite.

The main lithologies of the Superior Province in the regional model are the tonalite to tonalite gneiss in the Wawa and Abitibi sub-provinces, volcanic/metavolcanic rocks in the Abitibi greenstone belt, and scattered granitic to granodioritic intrusions. The metasedimentary rocks in the Pontiac sub-province are obscured by intrusions.

5.3.2 Grenville Province

The Grenville Province, located to the southeast of the GFTZ, is the primary exposure of the Grenville orogen, which extends from Lake Huron northeastward to the coast of Labrador. In the western Grenville of Ontario, seismic refraction and reflection surveys [e.g., *Mereu et al.*, 1986; *White et al.*, 2000] suggest a tectonic construct involving northwestward stacking of crustal segments to produce the Grenville orogen and an over-thickened crust. The Grenville orogen resulted from ~1100 Ma continent-continent and/or continent-arc collisions and consists of stacked Neoarchean, Paleoproterozoic, and Mesoproterozoic crustal sections [e.g., *Carr et al.*, 2000; *Ludden and Hynes*, 2000]. The Grenville Province comprises a complex assemblage of poly-metamorphosed crustal rocks including plutonic rocks, migmatites, ortho- and para-gneiss, as well as other metasedimentary and metavolcanic rocks. The rocks present in the regional study area range in age from 1.8 to 1.0 Ga. Of the two major belts in the Grenville Province, the Central Gneiss Belt (CGB) and the Central Metasedimentary Belt (CMB) [e.g., *Wynne-Edwards*, 1972], only the former belt is located within the area of interest. The GFTZ is a crustal-scale shear zone marking the northwestern edge of the Grenville orogeny.

The CGB is the oldest part of the Grenville Province, and is dominantly comprised of rocks from the Laurentian craton (pre-1.4 Ga) and younger supra-crustal rocks deposited along the craton margin. The rocks have been subjected to high pressure and high temperature metamorphism during Grenvillian orogenesis. These high-grade metamorphic rocks (e.g., gray gneisses) are exposures of deep sections of Earth's crust to depths of 20 – 30 km. The CMB is a lower grade metasedimentary belt that also corresponds to a lower crustal section. Since the CMB does not fall within the regional study area, we do not consider it further.

Because the seismic surveys coverage in the CGB is insufficient, we cannot identify all the smaller domains within the CGB in the 3-D model. Consequently, we simplify the regional reference model by treating the GFTZ and CGB as a single crustal type and assume that the high-grade gneiss is representative of the dominant lithology.

5.3.3 Southern Province and Sudbury Igneous Complex

The Southern Province comprises a passive margin sedimentary sequence deposited between 2.5 and 2.2 Ga on the southern margin of the Superior Province [e.g., *Long*, 2004; *Long*, 2009]. In the Sudbury region, strata of the Huronian Supergroup crop out extensively in the Southern Province. The main lithologies in the Huronian Supergroup are clastic sedimentary rocks such as sandstones, mudstones, conglomerates, and diamictites (with minor volcanic rocks) that have been metamorphosed at low grades. These sedimentary units crop out along the northern shore of Lake Huron and continue along the GFTZ to the Cobalt Embayment in the northeast. The thickness of the Huronian Supergroup can reach up to ~12 km to the south of the Sudbury Igneous Complex (SIC) [e.g., *Long*, 2009]. Some granitic

intrusions with ages 2.1 to 2.3 Ga, including the Skead, Murray and Creighton plutons were emplaced into the Huronian Supergroup.

The Sudbury Structure is a unique geological feature that straddles the boundary between the Superior Province and Southern Province immediately north of the Murray Fault, and about 15 km northwest of the Proterozoic GFTZ. The Sudbury structure is famous for its ore deposits of nickel, copper, cobalt and platinum group elements. The formation of this structure is due to a meteorite impact event 1.85 Ga ago [e.g., *Rousell et al.*, 1997; *Therriault et al.*, 2002]. The three major components of the structure include the Sudbury Basin, the SIC surrounding the basin in the form of an elliptical collar, and an outer zone of Sudbury Breccia [e.g., *Long*, 2009].

The Sudbury Basin is filled with sedimentary rocks of the Whitewater Group, which is approximately 3 km thick and consists of breccias of the Onaping formation, pelagic metasedimentary rocks of the Onwatin formation, and metagraywackes of the Chelmsford formation. The SIC consists of four units: the contact sublayer, norite, quartz gabbro, and granophyre [e.g., *Lightfoot et al.*, 1997c; *Naldrett and Hewins*, 1984]. The latter three units comprise the so-called Main Mass [*Naldrett and Hewins*, 1984]. The relative mass portions of the three units are approximately 40%, 10% and 50%. Footwall rocks consist of Archean granitic and mafic igneous rocks, including granulite facies rocks of the Levack gneiss complex to the north of the Sudbury Structure, and metavolcanic and metasedimentary rocks of the Huronian Supergroup to the south.

5.3.4 Palezoic sedimentary units

Paleozoic sediments, obscuring the underlying basement, cover approximately 25% of the surface of the study area. The Yavapai, Mazatzal, and Grenville boundaries beneath this Paleozoic sedimentary cover are extrapolated into the crust based on results from *Holm et al.* [2007] and *Van Schmus et al.* [2007]. Only one refraction seismic survey is available for the study area, the GLIMPCE – GLJ line [*Epili and Mereu*, 1991]. For this reason, we simplify the model and interpret the deep crust underlying this Paleozoic cover as extensions of Archean Superior Province and Proterozoic Grenville Province.

5.3.5 Simplified surface geology

The spatial resolution of existing seismic surveys available for determining the crustal structure in our regional model is less than that of the geological map of North America. Therefore, we have simplified the surface geological map on the basis of characteristic lithologies, metamorphism, tectonic events and U and Th abundances. For the upper crust in the 3-D model, we have identified seven main lithologic units (Figure 5.3, Table 5.5):

1. Tonalite and tonalite gneiss in Wawa and Abitibi sub-provinces;
2. Gneiss in the Central Gneiss Belt (CGB) of the Grenville Province;
3. Granitic to granodioritic intrusions of the Abitibi sub-province;

4. Paleozoic sedimentary cover in Great Lakes area;

5. Volcanic/metavolcanic rocks in the Abitibi greenstone belt;

6. The Sudbury Igneous Complex (SIC);

7. Sedimentary rocks of the Huronian Supergroup.

To construct the 3-D physical model of the study area, the simplified surface geology is combined with information for the vertical crustal structure obtained from refraction and reflection seismic surveys. Receiver function analyses from the Grenville Province provide additional constraints on the crustal thickness in this area [*Eaton et al.*, 2006]. The details of the geophysical inputs into the 3-D model are provided in the next section.

5.4 Geophysical 3-D model of the Regional Crust

Here we develop the 3-D geophysical model of the main reservoirs of U and Th in the regional crust centered at SNO+, including estimates of the volumes and masses of upper (UC), middle (MC) and lower crust (LC), together with their uncertainties. The seismic velocity data from deep crustal refraction surveys are used to distinguish the three crustal layers [*Epili and Mereu*, 1991; *Mereu et al.*, 1986; *Musacchio et al.*, 1997; *John A. Percival and West*, 1994; *Winardhi and Mereu*, 1997] . In this way, three boundary surfaces are defined in the 3-D model: the top of middle crust (TMC), the top of lower crust (TLC) and the Moho depth (MD). The P-wave velocities 6.6 km/s, 6.8 km/s and 8.0 km/s are adopted as contours to identify these surfaces. The upper crust is further modeled in detail for the seven dominant lithologic units as defined in the previous section by combining the simplified geological map and vertical crustal cross sections.

Table 5.1 The five seismic experiments that provide the 18 seismic lines used to model the crust in the region Surrounding SNO+.

Experiment	Main investigated area	Number of lines	Type[a]	Labels in Figure 5.2	Reference
LITHOPROBE	Sudbury Basin	2	RF	XY; AB	*Winardhi and Mereu* [1997]
	Superior Province	2	RF	EF; MG	*Winardhi and Mereu* [1997]
	Kapuskasing Structural Zone	5	RF	PW1; PW2; PW3; PW4; PW5	*John A. Percival and West* [1994]
COCRUST	Grenville Province	4	RF	AO; OB; BC; CD	*Mereu et al.* [1986]
O-NYNEX	Appalachian Province	1	RF	SP	*Musacchio et al.* [1997]
GLIMPCE	Great Lakes	1	RF	GLJ	*Epili and Mereu* [1991]
		1	RL	GLA	*Spence et al.* [2010]
COCORP	Michigan Basin	2	RL	MIC1; MIC2	*Brown et al.* [1982]

[a]RF: refraction; RL: reflection

5.4.1 Geophysical model of boundary surfaces

The geophysical inputs used for estimating the depth of the TMC, TLC and MD come from seismic surveys and receiver function analyses. To construct this 3-D model, five main reflection and refraction seismic experiments, performed over the last 30 years (Table 5.1), were used over an extended area that includes the six tiles (Figure 5.2). Some interpreted crustal cross sections based upon these seismic experiments (Table 5.2) were used to define the contacts between the seven lithologic units in the upper crust.

Table 5.2 The interpreted crustal cross sections used to define the contact between the seven dominant lithologic unit in the physical model of upper crust in the region surrounding SNO+.

Main investigated areas	Labels in Figure 5.2	Reference
Sudbury Basin	AA' - A'B	*Easton* [2000]
	40 - 41	*Adam et al.* [2000]
Superior Province	12 - 15 - 16a - 16c - 25 - 28 - 52	*Ludden and Hynes* [2000]
Kapuskasing Structural Zone	PP	*J. A. Percival and Peterman* [1994]
	G	*Geis et al.* [1990]
Grenville Province	31 - 32 - 33	*White et al.* [2000]
Great Lakes	J	*White et al.* [2000]

The Lithoprobe Abitibi-Grenville Seismic Refraction Experiment, which began in 1992, aimed to explore the main tectonic features of the Grenville and Superior provinces in the southeastern Canadian Shield [*Winardhi and Mereu*, 1997]. This project includes the acquisition of about 1250 km of seismic profiles along four long refraction lines. The profiles XY and AB, forming a cross-arm array centered a few kilometers away from SNO+, are particularly important for modeling the crustal structure directly beneath the detector (Figure 5.2). Profile EF images seismic discontinuities of the deep crustal layers beneath the Abitibi greenstone belt. The Central Metasedimentary Belt (CMB), the Central Gneiss Belt (CGB), the Grenville Front Tectonic Zone (GFTZ), the Pontiac sub-province and the Abitibi greenstone belt are investigated by the long refraction line MG. The five refraction profiles across the Kapuskasing Structural Zone ["PW" in Fig. 1b; *John A. Percival and West*, 1994] and the GLJ line in Lake Huron [*Epili and Mereu*, 1991] are used for constraining the crustal structure of the northern and southern region, respectively.

To increase the quality of the 3D model around the borders of the regional crust, we used data from four other seismic experiments that occur outside of the study area. The Ontario-New York-New England (O-NYNEX) refraction profile SP in the Appalachian Province [*Musacchio et al.*, 1997] and four refraction surveys made by the Canadian Consortium for Crustal Reconnaissance (COCRUST) [*Mereu et al.*, 1986] across the Ottawa

Graben are used to constrain the eastern boundary of our study area. Three reflection lines, GLA [*Spence et al.*, 2010], MIC1 and MIC2 [*Brown et al.*, 1982], located in the marginal western and southern area (Lake Superior and Michigan Basin) provide data on Moho depth in the southwestern region of the study area, but no refraction studies are available for this region.

The crustal thickness in the Grenville Province is obtained from receiver function analyses of 537 seismic events registered by 32 broadband seismic stations (blue triangles in Figure 5.2) [*Eaton et al.*, 2006]. The average uncertainty for the Moho depth obtained by the receiver function technique is ± 0.8 km, which is negligible and is not included in our model.

The Moho depth at the 32 teleseismic stations are combined with 343 and 22 data points digitized on 15 refraction and 3 reflection sections, respectively, in order to determine the depth of the different crustal layers. The average interval of digitalization along the 4552 km of refraction and reflection lines is 12.5 km. For refraction tomography, 343 depth points were digitized following the velocity contours of 6.6 and 6.8 km/s, which define the TMC and TLC surfaces. In Table 5.3 we report the descriptive statistics of depth-controlling points along each of the three boundary surfaces.

Table 5.3 Descriptive statistics of depth-controlling data points from refraction and reflection seismic profiles and receiver function analyses that are used to produce the TMC, TLC and MD depth maps. The minimum, mean and maximum values of the data points along each boundary surface are reported.

	N° point input	Variance (km^2)	Depth (km)		
			Min	Mean	Max
TMC	343	24.5	10.0	19.7	35.0
TLC	343	27.6	18.0	28.3	40.0
MD	397	23.2	31.0	42.6	56.0

Depth maps for TLC, TMC and MD surfaces are obtained by applying a geostatistical estimator (Ordinary Kriging) that infers the depths of these surfaces for locations without direct observations by interpolating between depth-controlling data points. The main advantages of this method are that it takes into account the spatial continuity of the depths and it provides the uncertainties of the estimated depths of three surfaces for each grid cell. The continuous depth maps for the TMC, TLC and MD surfaces (Figure 5.4 A, C, E) are obtained using this method. We also report the Normalized Estimation Errors (NEE) maps (Figure 5.4 B, D, F) that provide estimated uncertainties in terms of variance, normalized with respect to depth and expressed in percentage.

The average Moho depth in the six tiles is 42.3 ± 2.6 km, while the average TMC and TLC depths are 20.3 ± 1.1 km and 26.7 ± 1.5 km, respectively. The uncertainties associated with the average depths of TMC and TLC are correlated, and their sum corresponds to average uncertainty in the MD. Table 5.4 reports the average thickness and volumes of upper, middle and lower crust within the six tiles. The regional crustal model yields a very similar estimate of average crustal thickness (42.3 ± 2.6 km) as the global crustal reference model of

[*Huang et al.*, 2013] for the same region (42.6 ± 2.8 km). These two crustal thickness estimates are larger than the estimate provided in the new global crustal model CRUST 1.0, which yields an average crustal thickness of only 39.2 km for the study area, without uncertainty [*Laske et al.*, 2013]. The regional crustal model is based on *in situ* seismic surveys, which were carried out to understand the deep crustal structure, and thus provide a more accurate and precise evaluation of the crustal thickness and its uncertainty in this region than any global-scale crustal model. Another obvious difference between the regional crustal model and previous global models is the relative thickness of middle crust, which is very thin in the new 3-D regional model. This occurs because of our selection of the Vp interval from 6.6 to 6.8 km/s as the velocity range of the middle crust, which results in the thin middle crust.

Table 5.4 Physical properties (thickness, volume, volume fraction, density) of upper, middle and lower crust within the 3-D regional model, and comparisons with previous models.

	Thickness (km)			**Volume (10^6 km^3)**	**Volume (%)**	**ρ (g/cm^3)**		
	C 1.0[a]	**H'13[b]**	**This study**			**C 1.0**	**H'13**	**This study**
UC	11.8	14.7 ± 1.0	20.3 ± 1.1	4.2 ± 0.2	47.9	2.75	2.80	2.73 ± 0.08
MC	14.1	15.2 ± 1.0	6.4 ± 0.4	1.3 ± 0.1	15.3	2.82	2.88	2.96 ± 0.03
LC	13.3	12.7 ± 0.8	15.6 ± 1.0	3.2 ± 0.2	36.8	2.92	3.03	3.08 ± 0.06
Total	39.2	42.6 ± 2.8	42.3 ± 2.6	8.7 ± 0.5	100	==	==	==

[a]C 1.0 is the updated CRUST1.0 model by *Laske et al*. [2013] at http://igppweb.ucsd.edu/~gabi/rem.html; No uncertainty is provided in CRUST 1.0 for the thickness of crustal layers;
[b]Average of individual uncertainties for the 24 1° × 1° voxels in the reference model of [*Huang et al.*, 2013]

The densities of the middle and lower regional crust are estimated using the functional relationship between Vp and density provided by *Christensen and Mooney* [1995] (see their Table 8). Since the depth to center of the middle crust in the study area is about 25 km, we use the average densities obtained using the functions $\rho = a + b/Vp$ (where a and b are the empirically determined coefficients linking Vp and density) applied to 20 km, and 30 km depths, respectively, with average middle crust Vp as 6.7 ± 0.1 km/s. The center of the lower crust in the study area is about 35 km, and most of the layer has Vp of 7.0 ± 0.2 km/s. Thus, we use the functions for 30 km and 40 km depth. The average density of middle crust and lower crust are estimated to be 2.96 ± 0.03 and 3.08 ± 0.06 g/cm^3, respectively. The model of [*Huang et al.*, 2013] adopted the density information provided in CRUST 2.0 [*Bassin et al.*, 2000], and the updated CRUST 1.0 [*Laske et al.*, 2013] provides an even lower density crust (Table 5.4). The average densities for this region in the previous two global crust models are both lower than what we obtain here. This is perhaps due to the fact that the middle crust in

the regional model is deeper and thinner, and the lower crust is thicker than that of CRUST 1.0. The density of lower crust in [*Huang et al.*, 2013] falls within 1-sigma uncertainty of that in our regional model.

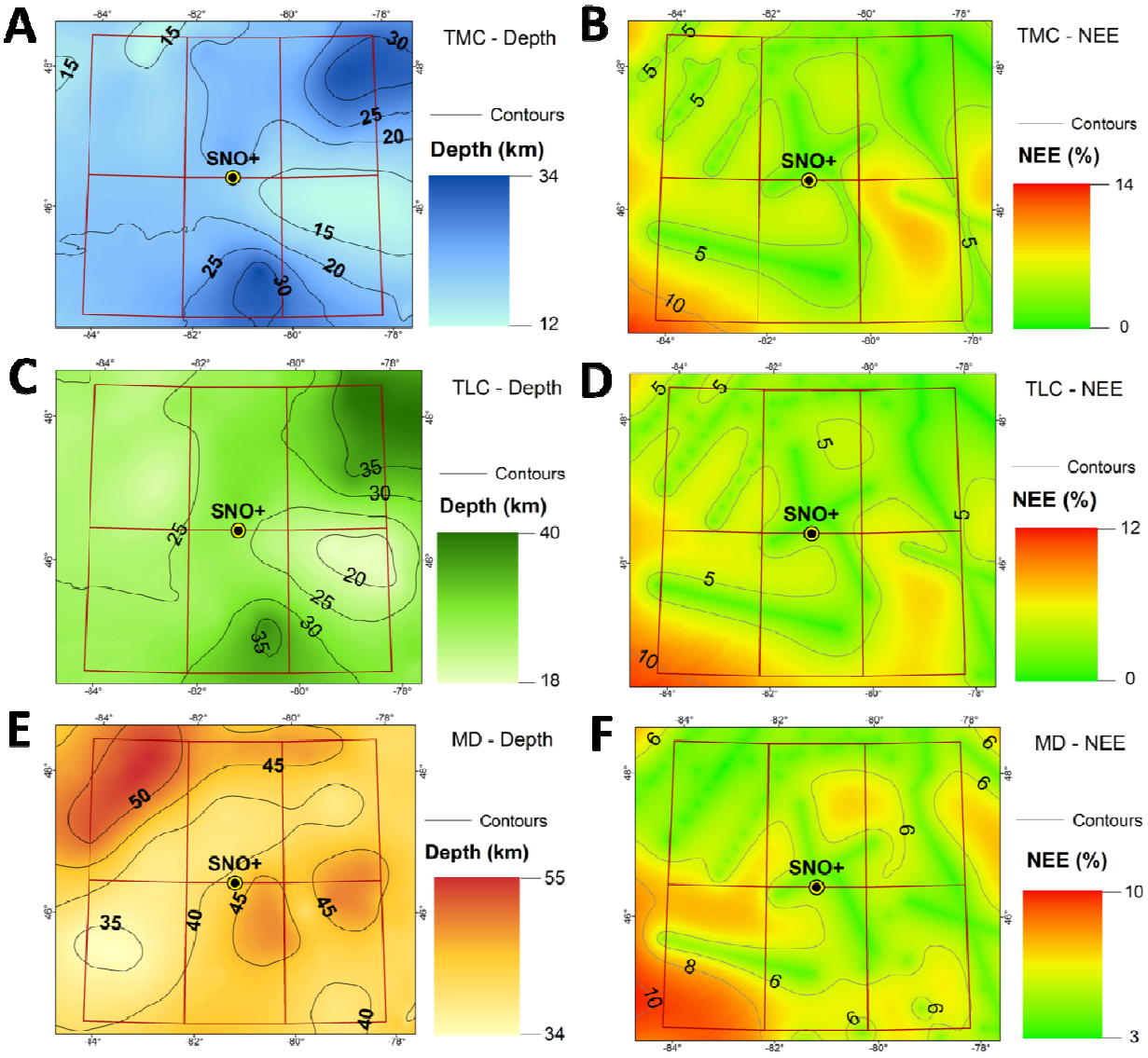

Figure 5.4 Maps (1 km × 1 km resolution) showing the surface depths of crustal boundary in the 3-D regional crust model: (A), (C), and (E) present the depth (km) to the TMC (Top of the Middle Crust), TLC (Top of the Lower Crust), and MD (Moho Depth), respectively. Maps of Figures 5.4B, 5.4D, and 5.5F are the normalized estimation of errors (in %) for the estimated depth of TMC, TLC, and MD, respectively.

5.4.2 Geophysical model of regional upper crust

As described previously, the geological map of the regional upper crust has been simplified into seven dominant lithologic units (Figure 5.3). The exposed contacts between the seven lithologic units are combined with interpreted crustal cross sections from the seismic profiles to construct the physical upper crust model. The physical properties (thickness, volume, density and mass) of each lithologic unit are reported in Table 5.5.

The tonalite or tonalite gneiss in the Wawa and Abitibi sub-provinces is the dominant lithology within the study area, accounting for 60% of the total volume of the regional upper crust. The top of this unit corresponds to the bottom of some minor lithologic units, or a flat Earth's surface, while its bottom is the TMC surface underneath the Superior Province, as revealed by interpreted crustal cross sections. Gneissic rocks in the CGB of the Grenville Province is the next most voluminous lithology, encompassing ~30% of the total volume of the regional upper crust; its surface exposure is not obscured by any other lithologies except for a thin veneer of Paleozoic sedimentary rocks in the southern portion of the study area (Figure 5.5 A and E). All other five lithologic units account for the remaining 10% of upper crustal volume. The thicknesses of these remaining lithologic units are constrained from interpreted crustal cross sections based on reflection seismic surveys. The thickness of the Paleozoic sedimentary cover in the Great Lakes region is further constrained by the contours of thicknesses of sedimentary rocks in the Michigan Basin [*Howell and van der Pluijm*, 1999]. South of the SIC, the thickness of the Huronian Supergroup can reach up to 12 km [e.g., *Long*, 2009] and, thus, for the purpose of better constraining its thickness, some virtual points with depths of 12 km are added to the 3-D model. The thickness of several regionally distributed granitic to granodioritic intrusions were estimated using reflection seismic surveys. The structure of the SIC has been extensively explored [*Boerner et al.*, 2000; *Milkereit et al.*, 1994; *Snyder et al.*, 2002] and existing seismic surveys are sufficient to constrain the SIC precisely. Some extrapolations regarding the thickness of the volcanic to metavolcanic rocks in the Abitibi greenstone belt were made based on existing geological cross-sections in order to estimate their thickness in areas lacking direct observations.

The density of each upper crustal lithologic unit is obtained from the literature. *Fountain et al.* [1990], *Salisbury and Fountain* [1994] and *Fountain and Salisbury* [1996] provide laboratory density measurements for a variety of samples from the Canadian Shield. The samples are here reclassified into tonalite-tonalite gneiss, granite-granodiorite and greenstone belt volcanic rocks and the average and standard deviation of the density are used for these lithologic units. The CGB gneissic rocks are assumed to have similar density to tonalite gneiss of comparable metamorphic grade. *Hinze et al.* [1978] provide drill core density information for sedimentary rocks in the Michigan Basin and we adopt this density for the Paleozoic sedimentary rocks. Densities of sedimentary rocks in the Huronian Supergroup are obtained from Ontario Geological Survey published preliminary map 2297. The density of the SIC is obtained from drill core information published by *Snyder et al.* [2002] and *Milkereit et al.* [1994]. Since 90% of the regional upper crust has a density of 2.73 ± 0.08 g/cm^3, the average upper crust is assumed to have the same density. With the volume and density information, the mass of each lithologic unit was calculated (Table 5.5).

Table 5.5 Physical properties (Geology feature, thickness, volume, volume fraction, density, and mass) of the seven lithologic units in the Upper Crust within the 3-D regional model.

Lithology/Geology	Average Thickness (km)	Volume (10^6 km^3)	Volume (%)	ρ (g/cm^3)	Mass (10^{18} kg)
Tonalite/Tonalite gneiss (Wawa-Abitibi)	16.6	2.51	60.6	2.73 ± 0.08[a]	6.9 ± 0.5
Central Gneiss Belt (Grenville Province)	14.5	1.25	30.2	2.73 ± 0.08[b]	3.4 ± 0.2
(Meta)volcanic rocks (Abitibi sub-province)	5.5	0.12	2.9	2.84 ± 0.14[a]	0.34 ± 0.01
Paleozoic sedimentary rocks	1.1	0.06	1.3	2.62 ± 0.19[c]	0.16 ± 0.01
Granite or granodiorite (Wawa-Abitibi)	5.2	0.09	2.2	2.67 ± 0.02[a]	0.24 ± 0.00
Huronian Supergroup, Sudbury Basin	4.4	0.11	2.7	2.69 ± 0.04[d]	0.30 ± 0.01
Sudbury Igneous Complex	6.1	0.006	0.1	2.8 ± 0.1[e]	0.02 ± 0.00

[a]Average values of data from [*Fountain and Salisbury*, 1996], [*Fountain et al.*, 1990] and [*Salisbury and Fountain*, 1994].
[b]Density of green unit is assumed equal to the density of the pink unit.
[c]Average values from data taken by [*Hinze et al.* 1978].
[d]Ontario Geological Survey - Geophysical Series - Preliminary map. 2297 - North Bay Marten River Area – Districts of Nipissing and Sudbury. Scale 1:100.000 (1980).
[e][*Snyder et al.*, 2002], [*Milkereit et al.*, 1994].

5.4.3 Cross-checking the 3-D model

Six schematic E-W and N-S cross-sections of the region show the results of the numerical 3-D model (Figure 5.5), with the correct positions and shapes of major tectonic features, such as the GFTZ in cross sections A-A', C-C' and D-D', and the SIC in cross sections A-A' and B-B'. The thickness of each minor lithologic units in the upper crust agrees with the interpreted cross-sections based on seismic surveys.

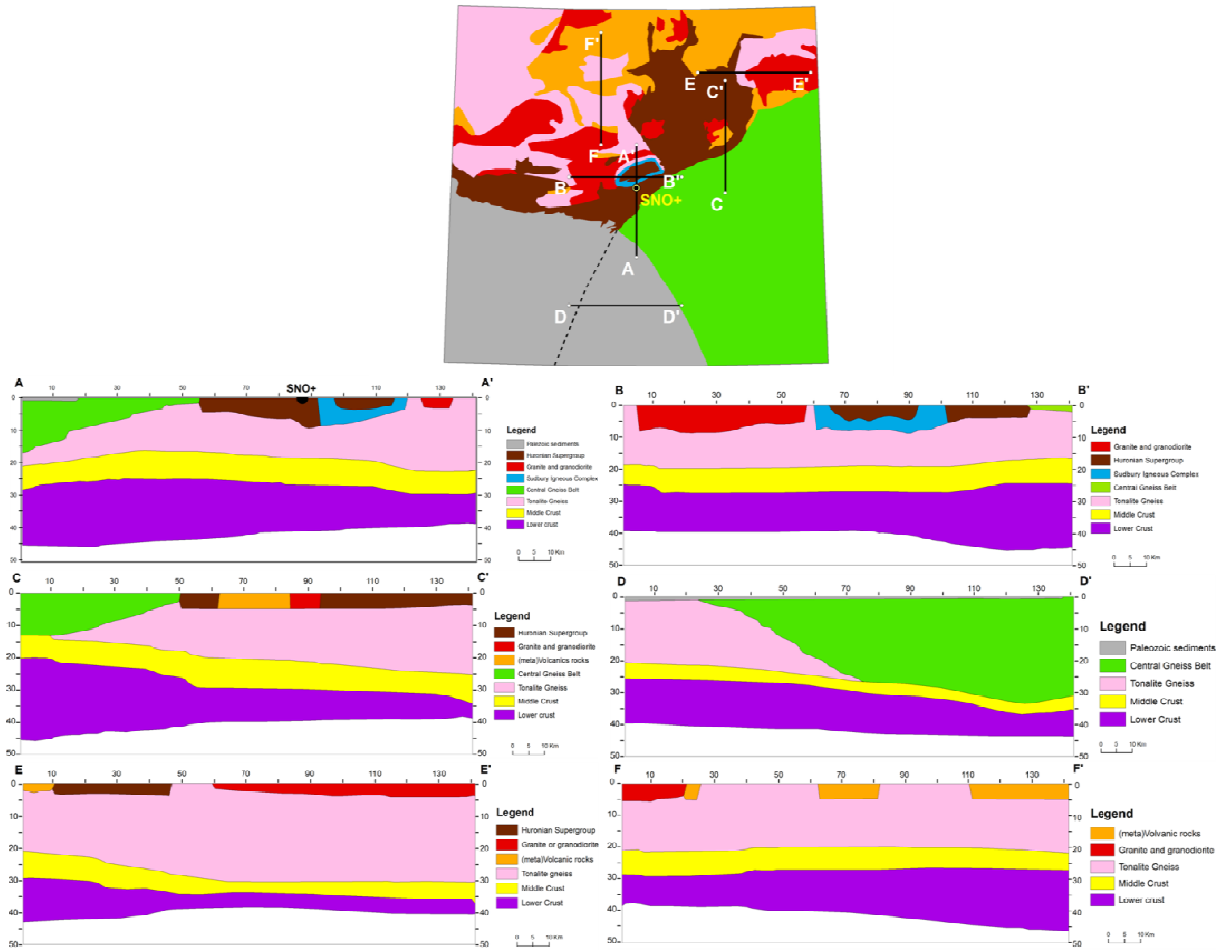

Figure 5.5 Six schematic E-W and N-S cross sections of the 3-D numerical model and their locations within the simplified geological map of the six tiles centered at SNO1. These modeled sections are located within major tectonic structures and display the 3-D architecture of the main lithologic units in the crust. Thicknesses and the shapes of the layers in the 3-D model are in good agreement with the seismic data reported in Figure 5.2 and listed in Tables 5.1 and 5.3.

5.5 Chemical composition of the crust near SNO+

The abundances of U and Th in the seven dominant, upper crustal lithologic units were evaluated based on analyses of representative outcrop samples. The OGS has published litho-geochemical databases that provide high quality U and Th abundance data (obtained mostly by inductively coupled plasma mass spectrometry -- ICP-MS, and sometimes by instrumental neutron activation analysis -- INAA) for some of the dominant lithologic units, such as the SIC, the Huronian Supergroup sedimentary rocks, granitic to granodioritic intrusions, and tonalite/tonalite gneiss. In addition, new unpublished compositional data for glacial tillites in the Huronian Supergroup were provided by Dr. Richard Gaschnig [*Gaschnig et al.*, 2014]. Data for the Abitibi greenstone belt volcanic rocks come from GEOROC, a web-based geochemical database, which contains a compilation of compositional data for volcanic to metavolcanic rocks from the belt. This compilation has also been supplemented with OGS data. For the CGB of the Grenville Province, there is limited U data, but abundant ICP-MS Th data provided by Dr. Trond Slagstad (NGU, Norway). The lake sediments in Ontario are

assumed to be sourced by Paleozoic sedimentary rocks. We use the composition of these lake sediments to represent the composition of the Paleozoic sedimentary rocks.

The quality of the dataset is improved by excluding all U and Th data determined by XRF, which is less sensitive and accurate compared to ICP-MS or INAA data. Some lithologic units are further subdivided into end members according to lithology/composition, such as Abitibi volcanic rock, the SIC, and felsic intrusions. The volcanic rocks of the Abitibi greenstone belt are a mixture of felsic, intermediate, and mafic rocks with relative mass proportions of 5%, 40% and 55%, respectively [*Card*, 1990]. The Main Mass of the SIC is composed of norite (40%), quartz gabbro (10%), and granophyre (50%) [e.g., *Lightfoot et al.*, 1997a]. Granite (60%) and granodiorite (40%) are the two dominant types of intrusive rocks. These proportions are obtained from the geological map by comparing the surface exposure areas of the two rock types in the red unit. For these three lithologic units, the weighted average composition is obtained using Monte Carlo simulations [*Huang et al.*, 2013] to predict the geoneutrino signals from these units.

After constructing the databases, average U and Th abundances for each of the lithologic units can be estimated, along with uncertainties. It has long been known that the frequency distributions of the abundances of highly incompatible elements, such as U and Th, in typical crustal reservoirs are strongly skewed and fit a log-normal distribution, rather than a Gaussian distribution [*Huang et al.*, 2013]. To reduce the influence of rare enriched or depleted samples on the log-normal average, we apply a 1.15-sigma filter that removes about 25% of the data. Then the median value of the distribution is used to represent the central tendency of the distribution, and 1-sigma uncertainty covers 68.3% of the remaining data population. The abundances of U and Th in each lithologic unit in the regional upper crust are reported in Table 5.6.

The U abundances in the tonalite and CGB gneiss, which together account for 90% of the upper crustal volume in the 3-D model, are $0.7^{+0.5}_{-0.3}$ ppm and 2.6 ± 0.4 ppm, and the Th abundances of these two units are $3.1^{+2.3}_{-1.3}$ ppm and $5.1^{+6.0}_{-2.8}$ ppm, respectively. There are only five high quality measurements of U abundances in the CGB gneiss, which is the key limitation of the statistics. This is also the reason why the U abundance in the CGB gneiss has a symmetric uncertainty. The Wawa-Abitibi volcanic rocks are depleted in HPEs compared to other lithologic units in the study area. The Huronian Supergroup metasedimentary rocks are the closest unit to the SNO+ detector and are enriched in U $4.2^{+2.9}_{-1.7}$ ppm and Th $11.1^{+8.2}_{-4.8}$ ppm relative to the greenstone belt rocks; therefore, this minor lithologic unit, due to its proximity to the detector, could be the dominant source of the geoneutrino signal at SNO+.

The composition of the middle and lower crust in the 3-D model is inferred from seismic velocity data from the refraction seismic surveys, using the same approach as that adopted by [*Huang et al.*, 2013]. The seismic velocity in the middle crust is 6.7 ± 0.1 (1-sigma) km/s, and for the top 70% of the lower crust is 7.0 ± 0.2 (1-sigma) km/s while the lower 30% has velocity >7.2 km/s.

Compiled laboratory ultrasonic velocity measurements of deep crustal samples taken at room temperature and various confining pressure are used to estimate the composition of the deep crust. At 600 MPa, felsic amphibolite-facies rocks have an average Vp of 6.34 ± 0.16 (1-sigma) km/s, while mafic amphibolite-facies rocks have a Vp of 6.98 ± 0.20 km/s. Felsic granulite-facies rocks have an average Vp of 6.52 ± 0.19 km/s, while mafic granulites have an average Vp of 7.21 ± 0.20 km/s [*Huang et al.*, 2013]. The temperature and pressure correction derivatives are -4×10^{-4} km s^{-1} $°C^{-1}$ and 2×10^{-4} km s^{-1} MPa^{-1} [*Christensen and Mooney*, 1995] [*Rudnick and Fountain*, 1995]. Assuming a typical conductive geotherm [*Pollack and Chapman*, 1977] corresponding to a surface heat flow of 50 mW m^{-2} (the observed average surface heat flow in the Sudbury region [*Perry et al.*, 2009]), the temperature in the crust increases linearly to 600°C at 50 km depth. The average depth of middle crust in the regional model is about 25 km, corresponding to a pressure of ~700 MPa and a temperature of ~300°C. Therefore, the pressure-temperature corrected felsic amphibolites have a Vp of 6.25 ± 0.16 km/s and mafic amphibolites have a Vp of 6.89 ± 0.20 km/s. For the lower crust, the pressure is ~1000 MPa and the temperature is ~400°C; therefore, the corrected felsic granulites have Vp of 6.45 ± 0.19 km/s and mafic ones have 7.14 ± 0.20 km/s. Given the Vp in the middle and top layer of lower crust is set to be 6.7 ± 0.1 km/s and 7.0 ± 0.2 km/s in the model, the fractions of felsic end member in the two reservoirs are 0.3 ± 0.4 and 0.2 ± 0.4, which are combined with the compositions of felsic and mafic end members from [*Huang et al.*, 2013] to calculate the U and Th abundances in the deep crust.

The abundances of U and Th in any single lithologic unit (except the CGB gneiss, for which only five U analyses are available) in the regional model are significantly correlated. Table 6 reports the correlation between logarithmic values of U and Th abundance in each reservoir. This correlation introduces a non-negligible effect on the uncertainties of the geoneutrino signal and radiogenic heat power. Previous reference models (global scale or regional scale) for the geoneutrino signal [*Coltorti et al.*, 2011; *Dye*, 2010; *Huang et al.*, 2013; *Mantovani et al.*, 2004] ignored the correlation between U and Th abundances. Here we use Monte Carlo simulations to incorporate fully the variations in U and Th abundances and the influence of the correlation between them in estimating uncertainties.

Table 5.6 U and Th abundances in Seven Lithologic Units in the Regional Upper Crust in the 3-D Model.

Lithologic Unit			U mean[a]	1-sigma		median	n	Th mean[a]	1-sigma		median	n	Correlation[b]
				+	-				+	-			
Tonalite/Tonalite gneiss		all	0.7	1.0	0.4	0.7	141	3.0	4.6	1.8	3.2	146	0.74
		filtered	**0.7**	**0.5**	**0.3**	0.7	111	**3.1**	**2.3**	**1.3**	3.1	107	
Gneiss in CGB		all	2.6	0.4	0.4	2.7	5	3.9	8.9	2.7	5.3	96	--
		filtered	**2.6**	**0.4**	**0.4**	2.7	5	**5.1**	**6.0**	**2.8**	5.9	68	
(Meta)volcanic rocks	Felsic (5%)	all	1.1	1.7	0.7	1.0	472	4.3	6.7	2.6	4.3	531	0.86
		filtered	**1.1**	**0.8**	**0.5**	1.0	402	**4.3**	**3.0**	**1.8**	4.1	416	
	Intermediate (40%)	all	0.5	1.1	0.3	0.5	192	1.6	3.3	1.1	1.6	246	0.87
		filtered	**0.5**	**0.4**	**0.2**	0.5	135	**1.5**	**1.3**	**0.7**	1.6	170	
	Mafic (55%)	all	0.3	0.8	0.2	0.3	333	0.9	2.4	0.6	0.8	414	0.88
		filtered	**0.2**	**0.4**	**0.1**	0.2	249	**0.8**	**1.0**	**0.4**	0.7	316	
Paleozoic sedimentary rocks		all	3.1	5.5	2.0	2.5	10606	4.5	3.0	1.8	4.4	2196	0.55
		filtered	**2.5**	**2.0**	**1.1**	2.3	8466	**4.4**	**1.6**	**1.2**	4.3	1700	
Felsic intrusion	Granite (60%)	all	3.9	4.1	2.0	4.1	26	24.1	26.8	12.7	28.0	25	0.60
		filtered	**4.0**	**2.3**	**1.4**	4.1	18	**29.7**	**12.0**	**8.6**	28.9	19	
	Granodiorite (40%)	all	1.1	0.8	0.5	1.1	92	5.4	6.2	2.9	5.5	92	0.81
		filtered	**1.2**	**0.5**	**0.3**	1.2	70	**5.2**	**3.1**	**2.0**	5.2	69	
Huronian Supergroup, Sudbury Basin		all	4.2	6.4	2.5	4.1	207	11.8	20.8	7.5	11.4	214	0.90
		filtered	**4.2**	**2.9**	**1.7**	4.2	156	**11.1**	**8.2**	**4.8**	11.3	177	
Sudbury Igneous Complex	Norite (40%)	all	1.1	0.5	0.3	1.2	80	5.6	1.6	1.2	5.7	80	0.76
		filtered	**1.2**	**0.2**	**0.2**	1.3	71	**5.7**	**0.7**	**0.7**	5.7	72	
	Quartz Gabbro (10%)	all	1.7	0.5	0.4	1.6	19	7.5	2.4	1.8	6.7	19	0.99
		filtered	**1.5**	**0.2**	**0.2**	1.5	13	**6.7**	**0.9**	**0.8**	6.6	14	
	Granophyre (50%)	all	3.3	0.2	0.2	3.2	25	14.9	1.0	1.0	14.8	25	0.95
		filtered	**3.3**	**0.1**	**0.1**	3.2	18	**15.2**	**0.7**	**0.6**	15.3	18	

[a]Log-normal mean, see *Huang et al.* [2013].

[b]Correlation between logarithmic values of the U and Th abundances.

5.6 Geoneutrino signal

In order to predict the geoneutrino signal and assign precise oscillation parameter values, the 3-D regional crustal model was divided into cells of 1 km × 1 km × 0.1 km dimension, generating a grid with about 9×10^7 cells. In each of these cells spatial, geophysical, and geochemical data were assigned.

Using the abundance and distribution of U and Th in the 3-D regional crustal model given above, the regional contribution to the geoneutrino signal at SNO+ is calculated by summing the geoneutrino signal produced by U and Th in each of the 9×10^7 cells.

For each cell the geoeneutrino flux is:

$$\phi(X) = \frac{n_X C_X}{4\pi\tau_X m_X} \frac{\rho(\vec{r}) a_X(r)}{\left|\vec{R}-\vec{r}\right|^2}$$

where:

- n_X is the number of antineutrinos emitted per decay chain.
- C_X, τ_X and m_X are the isotopic concentration, lifetime and mass of the nucleus X (i.e. U and Th).
- a_X is the elemental mass abundance of the nucleus X in each cell.
- $\rho(\vec{r})$ is the density of the cell.
- $\left|\vec{R}-\vec{r}\right|$ is the distance between the detector and the source of antineutrinos, assumed to be the at the centre of the cell.

The oscillated geoneutrino flux at SNO+ is calculated by taking into account three-flavor survival probability P_{ee} and the geoneutrino energy spectrum [*Fiorentini et al.*, 2012]: $\delta m^2 = 7.58 \cdot 10^{-5}\ \text{eV}^2$, $\sin^2(\theta_{12}) = 0.306$ and $\sin^2(\theta_{13}) = 0.021$. The survival probability for $\bar{\nu}_e$ having energy $E_{\bar{\nu}_e}$ (in natural units) produced at distance $\bar{r}$ from the detector is:

$$P_{ee}(E_{\bar{\nu}_e}, \vec{r}) = \cos^4(\theta_{13}) \left(1 - \sin^2(2\theta_{12}) \sin^2\left(\frac{\delta m^2 \vec{r}}{4E_{\bar{\nu}_e}}\right)\right) + \sin^4(\theta_{13})$$

For subsequent shells of Δr = 10 km the probability $P_{ee}(\vec{r}, X)$ is tabulated adopting the geoneutrino energy spectrum for U and Th. Assuming the detector efficiency ε = 1 and 10^{32} free target protons N_p, the geoneutrino signal in TNU originated by the radionuclide X for a fixed distance $\vec{r}$, can be calculated:

$$S(\vec{r}, X) = \phi(\vec{r}, X) P_{ee}(\vec{r}, X) \langle\sigma\rangle_X$$

where $\langle\sigma\rangle_X$ is the integrated inverse beta reaction cross section, i.e. 12.8×10^{-6} (TNU cm^2 s) and 4.04×10^{-6} (TNU cm^2 s) for U and Th, respectively. The total geoneutrino signal is calculated summing the contribution for each shell.

Monte Carlo simulation, as described by [*Huang et al.*, 2013] is employed to predict the uncertainty of the geoneutrino signal at SNO+. The uncertainties for thickness and density of each lithlogic unit, correlated abundances of U and Th, and fractions of felsic end members in the middle and lower crust are expressed by distributions of generated random number matrices. These input matrices are propagated through the geoneutrino signal calculation to obtain the distribution of the geoneutrino signal. The median value is chosen to describe the central tendency of the skewed output distribution, which is due to the propagation of log-normal distributions of U and Th abundances.

The predicted geoneutrino signals from U and Th and associated uncertainties (1-sigma) are reported in Table 5.7 for the seven dominant lithologic units in the upper crust, the middle and the lower crust. The uncertainties on the geoneutrino signals are apparently dominated by the uncertainties in U and Th abundances. For the upper crust, the Huronian Supergroup is the dominant geoneutrino source ($7.3^{+5.0}_{-3.0}$ TNU; 55% of the total contribution of the upper crust) because of its proximity to SNO+ and its high U and Th abundances. The tonalite/tonalite gneiss in the Wawa-Abitibi sub-provinces and CGB gneissic rocks contribute comparable geoneutrino signals (~2 TNU) at SNO+. The felsic intrusions and the SIC both contribute less than 1 TNU. The other two lithologic units (volcanic rocks in the Abitibi greenstone belt and Paleozoic sedimentary rocks in Great Lakes area) add negligible contributions. The total geoneutrino signal at SNO+ from the regional crust is predicted to be $15.6^{+5.3}_{-3.4}$ TNU, 85% of which originates from the upper crust.

It is of note that the Elliot Lake uranium deposit occurs within the study area (Figure 5.1). However, this deposit does not produce a significant geoneutrino signal at SNO+. Uranium mining in the area of Elliot Lake, Ontario was initiated in the mid-1950s, but operations have now ceased. The U abundances in the ores ranged between 100-1000 ppm. These inactive uranium mines are ~100 km to the west of the SNO+ detector. Assuming an exceptionally generous total volume of all the mines in Elliot Lake reached 5 km × 5 km × 5 km (5 km is projected to 1 mm in the 1:5M geology map used to construct the regional crust model) and the density of the ore is 3000 kg/m^3, the total mass of U is 3.8×10^{10} to 3.8×10^{11} kg. Given the geoneutrino activity of U is 7.64×10^7 kg^{-1} s^{-1} [*Fiorentini et al.*, 2007], the geoneutrino luminosity of these deposits in Elliot Lake is 2.9×10^{18} to 2.9×10^{19} s^{-1}, and the corresponding geoneutrino flux at the SNO+ is only 2.3×10^3 to 2.3×10^4 cm^{-2} s^{-1}, which translates into a geoneutrino signal of 0.02 to 0.2 TNU. Comparing to the total U signal at SNO+ originating from the regional crust (Table 5.7), the Elliot Lake U deposit can contribute only 0.2% to 2%, which is negligible given that the uncertainty on the geoneutrino signal is near 30%. For this reason, the Elliot Lake uranium deposit is not included in our regional crust model

Table 5.7 Abundances of U and Th (ppm), heat production (μW m^{-3}) and geoneutrino signal (TNU) at SNO+ from all reservoirs in the 3-D regional model.

Lithology/Geology	A(U)	A(Th)	H(U)	H(Th)	S(U)	S(Th)	S(U+Th)
Tonalite/Tonalite gneiss (Wawa-Abitibi)	$0.7^{+0.5}_{-0.3}$	$3.1^{+2.3}_{-1.3}$	$0.2^{+0.1}_{-0.1}$	$0.22^{+0.17}_{-0.09}$	$1.6^{+1.1}_{-0.7}$	$0.5^{+0.4}_{-0.2}$	$2.2^{+1.4}_{-0.9}$
Central Gneiss Belt (Grenville Province)	$2.6^{+0.4}_{-0.4}$	$5.1^{+6.0}_{-2.8}$	$0.70^{+0.11}_{-0.10}$	$0.36^{+0.43}_{-0.20}$	$1.8^{+0.3}_{-0.3}$	$0.2^{+0.3}_{-0.1}$	$2.1^{+0.4}_{-0.3}$
(Meta)volcanic rocks (Abitibi sub-province)	$0.4^{+0.3}_{-0.1}$	$1.5^{+0.9}_{-0.5}$	$0.1^{+0.1}_{-0.0}$	$0.11^{+0.06}_{-0.04}$	$0.02^{+0.01}_{-0.01}$	$0.004^{+0.003}_{-0.002}$	$0.02^{+0.01}_{-0.01}$
Paleozoic sediments	$2.5^{+2.0}_{-1.1}$	$4.4^{+1.6}_{-1.2}$	$0.65^{+0.51}_{-0.29}$	$0.30^{+0.11}_{-0.08}$	$0.04^{+0.03}_{-0.02}$	$0.01^{+0.00}_{-0.00}$	$0.05^{+0.04}_{-0.02}$
Granite or granodiorite (Wawa-Abitibi)	$2.8^{+1.4}_{-0.8}$	$19.6^{+7.1}_{-5.2}$	$0.76^{+0.36}_{-0.23}$	$1.41^{+0.51}_{-0.37}$	$0.3^{+0.2}_{-0.1}$	$0.2^{+0.1}_{-0.0}$	$0.5^{+0.2}_{-0.1}$
Huronian Supergroup, Sudbury Basin	$4.2^{+2.9}_{-1.7}$	$11.1^{+8.2}_{-4.8}$	$1.13^{+0.77}_{-0.46}$	$0.78^{+0.59}_{-0.33}$	$6.2^{+4.3}_{-2.6}$	$1.1^{+0.8}_{-0.5}$	$7.3^{+5.0}_{-3.0}$
Sudbury Igneous Complex	$2.3^{+0.2}_{-0.1}$	$10.7^{+0.4}_{-0.4}$	$0.63^{+0.03}_{-0.02}$	$0.77^{+0.03}_{-0.03}$	$0.6^{+0.0}_{-0.0}$	$0.2^{+0.0}_{-0.0}$	$0.8^{+0.0}_{-0.0}$
Upper crust	$1.4^{+0.3}_{-0.2}$	$4.6^{+2.3}_{-1.4}$	$0.38^{+0.08}_{-0.06}$	$0.33^{+0.17}_{-0.10}$	$10.9^{+4.4}_{-2.8}$	$2.4^{+1.0}_{-0.6}$	$13.3^{+5.2}_{-3.3}$
Middle crust	$0.8^{+0.5}_{-0.3}$	$3.5^{+2.8}_{-1.6}$	$0.2^{+0.1}_{-0.1}$	$0.25^{+0.20}_{-0.11}$	$0.9^{+0.5}_{-0.3}$	$0.3^{+0.2}_{-0.1}$	$1.2^{+0.7}_{-0.4}$
Lower crust	$0.2^{+0.2}_{-0.1}$	$1.4^{+1.8}_{-0.7}$	$0.06^{+0.04}_{-0.02}$	$0.10^{+0.13}_{-0.05}$	$0.5^{+0.3}_{-0.2}$	$0.2^{+0.3}_{-0.1}$	$0.7^{+0.6}_{-0.3}$
Total Crust	$0.9^{+0.2}_{-0.1}$	$3.6^{+0.6}_{-0.7}$	$0.3^{+0.1}_{-0.0}$	$0.26^{+0.11}_{-0.07}$	$12.5^{+4.4}_{-2.8}$	$3.0^{+1.0}_{-0.7}$	$15.6^{+5.3}_{-3.4}$

5.7 Discussions

5.7.1 Heat production

The estimates of U and Th abundances in different upper crustal lithologic units are based on measurements of outcrops of representative rock types. The heat flow measurements carried out in the Canadian Shield [e.g., *Perry et al.*, 2006] provide a test of the 3-D regional crustal model.

We calculate the heat production in each of the upper crustal lithologic unit in the regional crust model (Table 5.7). The heat production of the isotope X (i.e. ^{235}U, ^{238}U and ^{232}Th) for unit of volume is calculated as:

$$H(X) = \varepsilon'_H(X) \cdot \rho \cdot a(X)$$

where ρ is the density (Table 5.4 and Table 5.5), a and ε'_H are the abundances (Table 5.7) and the heat production rate for unit of mass at natural isotopic composition respectively [*Fiorentini et al.*, 2007].

The heat production and its uncertainty strictly depend on the U and Th abundances. We have not included K in our regional model, as geoneutrinos generated during its decay cannot be detected using current technology. We therefore assume that the K/U in the crust is about 10^4 [e.g., *Rudnick and Gao*, 2003; *Wasserburg et al.*, 1964], and therefore the heat production of K is 1/3 of that of U.

For the Superior Province, the tonalite/tonalite gneiss in the Wawa and Abitibi sub-provinces dominates the heat production in the upper crust. The calculated heat production of the upper crust of the Superior Province is 0.62 $\mu W\ m^{-3}$ (with contributions from U, Th and K of 0.25, 0.29 and 0.08 $\mu W\ m^{-3}$, respectively), while that of the middle crust is 0.54 $\mu W\ m^{-3}$ and the lower crust is 0.18 $\mu W\ m^{-3}$. Given a thickness of upper, middle and lower crust in the Superior Province of 20.3, 6.4 and 15.6 km, respectively, then the heat flow contribution from the bulk crust in the Superior Province (Wawa and Abitibi sub-provinces region) is estimated at 19 $mW\ m^{-2}$. If the mantle heat flow in this area is between 12-18 $mW\ m^{-2}$ [e.g., *Perry et al.*, 2006], the average surface heat flow in the Superior Province is between 31-37 $mW\ m^{-2}$, which is lower than the measured average heat flow of 40.9 ± 0.9 $mW\ m^{-2}$ [*Perry et al.*, 2006, where the uncertainty is expressed as the standard error of the mean and is likely to be an underestimate of the true uncertainty]. Given that the uncertainty on the estimate of crustal heat flow contribution from our model is greater than 25% (± 5 $mW\ m^{-2}$) or even higher considering the variations of U and Th abundances, the heat flow measurements and the 3-D regional model agree.

The upper crust of the CGB of the Grenville Province is relatively enriched in U and Th with a heat production of 1.29 $\mu W\ m^{-3}$ compared to the Superior Province. Thus, given the thickness of upper, middle and lower crust in Grenville Province is 14.5, 6.4 and 15.6 km, the crustal contribution to surface heat flow is 25 $mW\ m^{-2}$. The Grenville Province also has an average surface heat flow of 41 $mW\ m^{-2}$[*Mareschal and Jaupart*, 2004]. Assuming the mantle heat flow is 12-18 $mW\ m^{-2}$, the total surface heat flow is predicted to be 37-43 $mW\ m^{-2}$. Thus, the 3-D regional crustal model predicts a surface heat flow that agrees with surface measurements for the Grenville Province.

Heat flow measurements made near the SIC yield an average of 53 $mW\ m^{-2}$ [*Perry et al.*, 2009]. The locally enhanced heat flow is interpreted as being due to the thick Huronian Supergroup and granitic intrusions that are present around the SIC. The 3-D model shows a maximum thickness of Huronian Supergroup to the south of the SIC of 12 km, which can itself contribute a heat flow of 27 $mW\ m^{-2}$. If the rest of the upper crust is high-grade gneissic rock such as tonalite gneiss [*Lightfoot et al.*, 1997a], this unit can generate 4 $mW\ m^{-2}$. With 6 $mW\ m^{-2}$ from deep crust and 12-18 $mW\ m^{-2}$ mantle flow, the surface heat flow near the SIC is calculated to be 49-55 $mW\ m^{-2}$ for the 3-D model presented here. This range agrees with the surface heat flow measurements. However, the 3-D regional model does not have sufficiently high resolution to enable one to determine the variation of surface heat flow in the area near the SIC due to the lack of dense seismic survey coverage.

5.7.2 Mantle geoneutrino signal

The motivation for undertaking this regional crustal study in the Sudbury area is, in part, to determine whether the SNO+ detector, on its own, has the sensitivity to discriminate the mantle geoneutrino signal, which can be obtained by subtracting the crustal signal from future experimentally measured signal ($S_{tot,\ meas}$):

$$S_{mantle} = S_{tot,meas} - S_{FFC} - S_{LOC.}$$

The crustal signal is divided into two components FFC (Far Field Crust) and LOC (LOcal Crust). [*Huang et al.*, 2013] predicted the FFC signal at SNO+ to be $15.1^{+2.8}_{-2.4}$ TNU and the LOC to be $18.9^{+3.5}_{-3.3}$ TNU.

Our regional crustal study predicts an updated LOC signal of $15.6^{+5.3}_{-3.4}$ TNU, which is within 1-sigma uncertainty of the prediction obtained in the global reference model. The uncertainty for the LOC signal from the regional crustal study is larger than the uncertainty from the global reference model. The main reason for the larger uncertainty is the large variations in U and Th abundances in each of the dominant upper crustal lithologic units, especially the Huronian Supergroup (Table 5.6). Our model yields a larger uncertainly on U and Th abundances in the regional crust than global model, since the grid on the global model was so coarse that it could not account for regional variability. The only exception is the SIC, for which only a single dataset from an OGS Open File Report 5959 [*Lightfoot et al.*, 1997b] is used to estimate the U and Th abundances. Considering the much larger surface exposures of other lithologic units, the variations of rock type and chemical composition become larger.

The bulk crustal geoneutrino signal at SNO+ is estimated to be $30.7^{+6.0}_{-4.2}$ TNU, by summing the FFC signal [*Huang et al.*, 2013] with LOC signal from this study. Since the FFC and LOC geoneutrino signals at SNO+ are independently estimated, their individual uncertainties should be summed up in a quadratic approach, rather than linear. In this way, this regional crustal study for Sudbury slightly reduces the uncertainty on the predicted bulk crustal geoneutrino signal compared to the prediction based on global reference model, which is $34.0^{+6.3}_{-5.7}$ TNU [*Huang et al.*, 2013]. The continental lithospheric mantle is predicted to produce about 2 TNU at SNO+ [*Huang et al.*, 2013]. Assuming a BSE compositional model of *W F McDonough and S S Sun* [1995], the predicted mantle signal at SNO+ is 7 TNU [*Šrámek et al.*, 2013]. Without taking into account the uncertainties on the signal from continental lithospheric mantle and convecting mantle, the total geoneutrino signal at SNO+ is predicted to be 40^{+6}_{-4} TNU.

For the sake of simplicity, we adopt an uncertainty on the bulk crustal signal at SNO+ as 5.1 TNU in the discussion below. Following the equations defined by *Dye* [2010], the mantle signal determination at SNO+ has a systematic uncertainty of 2.1 TNU, assuming the systematic uncertainty for nuclear reactor events is 0.9 TNU and for detection exposure

determination is 1.9 TNU. Counting uncertainty for geoneutrino detection decreases with accumulation of geoneutrino events following Poisson's law. Assuming SNO+ can "see" 30 geoneutrino events per year, the counting uncertainty on the geoneutrino detection rate drops to 11% of 40 TNU after three years. By summing the counting and systematic uncertainties for the geoneutrino event rate at SNO+, the combined uncertainty becomes 4.7 TNU. Therefore, the mantle signal determination at SNO+ has a total uncertainty of 6.9 TNU after three years of full operation and after subtracting the crustal signal from the measured total signal.

Šrámek et al. [2013] predicted the mantle geoneutrino signal at SNO+ using various BSE compositional models and mantle structure to range between 2 to 16 TNU. To resolve these different mantle signals, the uncertainty for determining the mantle signal should be, at most, 7 TNU, which is the same as SNO+'s sensitivity to the mantle signal as described above. Unfortunately, the current constraints on the abundances and distributions of U and Th in the regional crust, especially in the Huronian Supergroup, are not good enough to make the goal of resolving the signal from the mantle feasible. There are three possible ways to advance this situation: 1) improving our knowledge of the distribution of the Huronian Supergroup by undertaking higher density seismic surveys, as well as performing a systematic study of the U and Th abundances in different representative metasedimentary/sedimentary rocks; 2) combing the experimental results at the three operating detectors to determine the mantle signal, rather than relying on any single detector; 3) conducting a geoneutrino experiment, such as the proposed Hanohano detector [*Learned et al.*, 2008], which is carried out in the oceans in order to minimize the signal from continental crust.

Performing high-density seismic surveys within the Huronian Supergroup would allow better estimation of its physical structure with smaller uncertainty (~10%). The geophysical uncertainty will contribute ~±1 TNU on the geoneutrino signal originating from the Huronian Supergroup. The relatively large variations of U and Th abundances in the Huronian Supergroup are the dominant sources of uncertainty on the geoneutrino signal from this source. Ideally, detailed geochemical mapping of U and Th abundance variations in the area will improve the geoneutrino signal prediction significantly. If the geochemical uncertainties on the Huronian Supergroup (e.g., U and Th abundances) can be reduced to 10 to 20%, they would contribute ~±1 to ±2 TNU uncertainty on the geoneutrino signal. Combining the geophysical and geochemical uncertainty contributions, higher resolution studies of the Huronian Supergroup are likely to reduce the uncertainty on the geoneutrino signal from this source to ~±2 TNU, smaller than the $^{+5.0}_{-3.0}$ TNU obtained in this study. Given that this task is feasible in the near future, the uncertainty on the LOC geoneutrino signal at SNO+ could be reduced to ~±2.5 TNU, and the bulk crust signal would have an uncertainty ~±3 TNU. Following this approach, the extracted mantle signal from future experimental results at SNO+ will have an uncertainty ~±5.6 TNU, which would allow better resolution of the various BSE compositional models.

5.8 Final remarks

We have constructed a 3-D regional crustal reference model aimed at predicting the geoneutrino signal at SNO+, a third geoneutrino detector located in Sudbury, Ontario, Canada, which is scheduled to come on-line in 2014. The uncertainty of the predicted geoneutrino signal is estimated through Monte Carlo simulation, and stems mainly from the large uncertainties on U and Th abundances in the upper crust. The main results of this study are as follows:

1. Surface geology, refraction and reflection seismic surveys, receiver function analyses, and interpreted vertical crustal cross sections in the Sudbury region are integrated into a 3-D model for the six 2° × 2° tiles centered at SNO+. The average thickness of the regional crust is estimated to be 42.3 ± 2.6 km, which is in good agreement with the results obtained in the previous global crustal reference model [*Huang et al.*, 2013]. The thickness of upper crust reaches 20.3 ± 1.1 km, which accounts for about half of the bulk regional crust.

2. The upper crust is subdivided into seven dominant lithological units in order to improve the resolution in predicting the geoneutrino signal. The tonalite/tonalite gneiss in the Wawa and Abitibi sub-provinces is the dominant rock type (60% of upper crust), and has $0.7^{+0.5}_{-0.3}$ ppm U and $3.1^{+2.3}_{-1.3}$ ppm Th. The low proportion of HPEs relative to global average upper continental crust reflects the fact that the Superior Province is an Archean craton with intrinsically low heat production, consistent with other Archean cratons globally. The high-grade gnessic rock, with 2.6 ± 0.4 ppm U and $5.1^{+6.0}_{-2.8}$ ppm Th, in the Central Gneiss Belt (CGB) of Grenville Province is the second dominant rock type in the 3-D model (30% of upper crust). Huronian Supergroup metasedimentary rocks are the closest unit to the SNO+ detector and are enriched in U $4.2^{+2.9}_{-1.7}$ μg/g and Th $11.1^{+8.2}_{-4.8}$ μg/g relative to the other units. All of the uncertainties are propagated through Monte Carlo simulations to the geoneutrino signal prediction.

3. The total regional crust contribution of the geoneutrino signal at SNO+ is predicted to be $15.6^{+5.3}_{-3.4}$ TNU. This signal is somewhat lower than the prediction made using the global reference model [*Huang et al.*, 2013], which is $18.9^{+3.5}_{-3.3}$ TNU. This difference is likely to be due to the lower HPEs in Archean to Proterzoic rocks of the Canadian Shield relative to the global average bulk upper continental crust. Considering the uncertainty, the two predictions of geoneutrino signal are consistent with each other. The Huronian Supergroup is predicted to be the dominant source of the geoneutrino signal and its uncertainty at SNO+, and variation in U and Th abundances within the Huronian Supergroup is the primary source of the large uncertainty on the predicted geoneutrino signal.

4. Assuming that the continental lithospheric mantle and convecting mantle together contribute a 9 TNU signal to SNO+, the total geoneutrino signal at SNO+ is estimated to be 40^{+6}_{-4} TNU.

5. The large uncertainty in the crustal geoneutrino signal indicates that SNO+, on its own, is unlikely to provide constraints on the mantle geoneutrino signal, and therefore to the debate regarding BSE compositional models. Several future approaches to constrain mantle geoneutrino signal are: improve the 3-D regional model for predicting the regional crustal contribution by increasing the resolution of the distribution of the Huronian Supergroup using a higher density of local seismic surveys and geochemical analyses; combining experimental results at the three operating detectors to place better constraints on the mantle signal; and conducting geoneutrino detection in the oceans, such as the proposed Hanohano detector, in order to minimize the signal from continental crust.

The content of this chapter is based on the following publication:

Huang Y., Strati V., Mantovani F., Shirey S.B. and McDonough W.F. *Regional study of the Archean to Proterozoic crust at the Sudbury Neutrino Observatory (SNO+), Ontario: Predicting the geoneutrino flux.* Geochemistry, Geophysics, Geosystem (2014) 15(10): 3925-3944.
DOI: 10.1002/2014gc005397

Chapter 6

Expected geoneutrino signal at JUNO

Since Pauli theorized the existence of antineutrinos in 1930, giant steps were made in the knowledge of neutrino physics (i.e. oscillation parameters, flavor states). Nevertheless to date the determination of the mass hierarchy as well as the absolute mass of electron, muon and tau neutrinos is still a missing piece of understanding. The construction of the JUNO detector represents the attempt of the Chinese scientific community to address these questions and at the same time to play a decisive role in Neutrino Geoscience. The Jiangmen Underground Neutrino Observatory (JUNO) located in southern Guangdong Province, has the manifest goal to determine neutrino mass hierarchy and precisely measure oscillation parameters by detecting reactor antineutrinos. Indeed beside the large mass (20 kton), the peculiarity of JUNO is the site location very close (~ 50 km) to the under construction Yangjiang and Taishan Nuclear Power Plants. So in 2020, when the data taking is expected to start, JUNO will be able to collect statistically significant reactor antineutrino data and also to observe supernova neutrinos and study the atmospheric, solar neutrinos and geoneutrinos.

This study represented for me the opportunity to provide the first estimate of the geoneutrino signal expected at JUNO that will be a reference point for the future studies of the whole Collaboration, to which I recently joined. On the base of existing reference model and following a well consolidated strategy [*Huang et al.*, 2013], I produced and studied geoneutrino spectrum adopting update oscillation parameters, with particular regards to the interference with reactor antineutrinos. The expected signal is predicted and the different contributions from the main Earth reservoirs are highlighted. I focused in particular in the area dedicated to the 6° × 4° local crust surrounding the detector that, as is explained in the previous chapter, is the most relevant aspect in the geoneutrino modeling. Taking advantage of the reference worldwide model for antineutrinos from reactors of [*Baldoncini et al.*, 2015] in which I was involved, I was able to provide also the ratio between reactor antineutrino and geoneutrino signals considering two different scenarios. These results shed light on the sensitivity of JUNO for the geoneutrino measurements and will guide the next refined modeling of the local crust, identifying the significant targets for improving the prediction of JUNO geoneutrino signal.

6.1 Background

Reactor antineutrino, i.e. electron antineutrinos emitted during the beta decays of fission products from ^{235}U, ^{238}U, ^{239}Pu and ^{241}Pu burning, are the most significant source of

background for geoneutrino measurements. Approximately 30% of the reactor antineutrino events are recorded in the geoneutrino energy window extending from the IBD threshold up to the endpoint of the ^{214}Bi beta decay spectrum (3.272 MeV) [*Fiorentini et al.*, 2010]. The Terrestrial Neutrino Unit (TNU), which is the signal that corresponds to one IBD event per 10^{32} free protons per year at 100% efficiency, is used to compare the different integrated spectral components (i.e. antineutrinos from U, Th and reactors) measured by the detectors or just beneath the Earth's surface.

In the past decade reactor antineutrino experiments played a decisive role in unraveling the neutrino puzzle, which currently recognizes three flavor eigenstates (ν_e, ν_μ, ν_τ), each of which mixes with three mass eigenstates (ν_1, ν_2, ν_3) via three mixing angles (θ_{12}, θ_{13}, θ_{23}). The quantities that govern the oscillation frequencies are two differences between squared masses, (i.e. $\delta m^2 = m_2^2 - m_1^2 > 0$ and $\Delta m^2 = m_3^2 - (m_1^2+m_2^2)/2$). Central to neutrino studies is understanding the neutrino mass hierarchy (i.e. $\Delta m^2 > 0$ or $\Delta m^2 < 0$) [*Capozzi et al.*, 2014; *Ge et al.*, 2013].

Massive (>10kton) detectors such as the JUNO [*Li*, 2014] and Reno-50 [*Kim*, 2013] experiments are being constructed at medium baseline distances (a few tens of km) away from bright reactor antineutrino fluxes in order to assess significant physics goals regarding the neutrino properties, in first place the mass hierarchy. These experiments intend also to obtain sub-percent precision measurements of neutrino oscillation parameters and along the way make observations of events of astrophysical and terrestrial origin.

The Jiangmen Underground Neutrino Observatory (JUNO) is located (N 22.12° E 112.52°) in Kaiping, Jiangmen, Guangdong province (South China), about 53 km away from the Yangjiang and Taishan nuclear power plants, which are presently under construction. The combined thermal power of these two units is planned to be on the order of 36 GW [*Li and Zhou*, 2014] (Figure 6.1). The JUNO experiment is designed as a liquid scintillator detector of 20 kton mass that will be built in a laboratory some 700 m underground (approximately 2000 m water equivalent). This amount of overburden will attenuate the cosmic muon flux, which contributes to the overall detector background signal, but this overburden is significantly less than that at the KamLAND and Borexino experiments. The detector energy response and the spatial distribution of the reactor cores are the most critical features affecting the experimental sensitivity [*Li et al.*, 2013] required to achieve the intended physics goals.

The goal of this present study is to predict the geoneutrino signal at JUNO on the basis of an existing reference Earth model, together with an estimate of the expected reactor antineutrino signal. Since a significant contribution to the expected geoneutrino signal comes from U and Th in the continental crust surrounding the site, we follow past approaches to study the local contribution [*Coltorti et al.*, 2011; *Fiorentini et al.*, 2012; *Huang et al.*, 2014], with a particular interest in focusing in on the closest 6° × 4° grid surrounding the detector, we define this latter region as the LOcal Crust (LOC) (Figure 6.1).

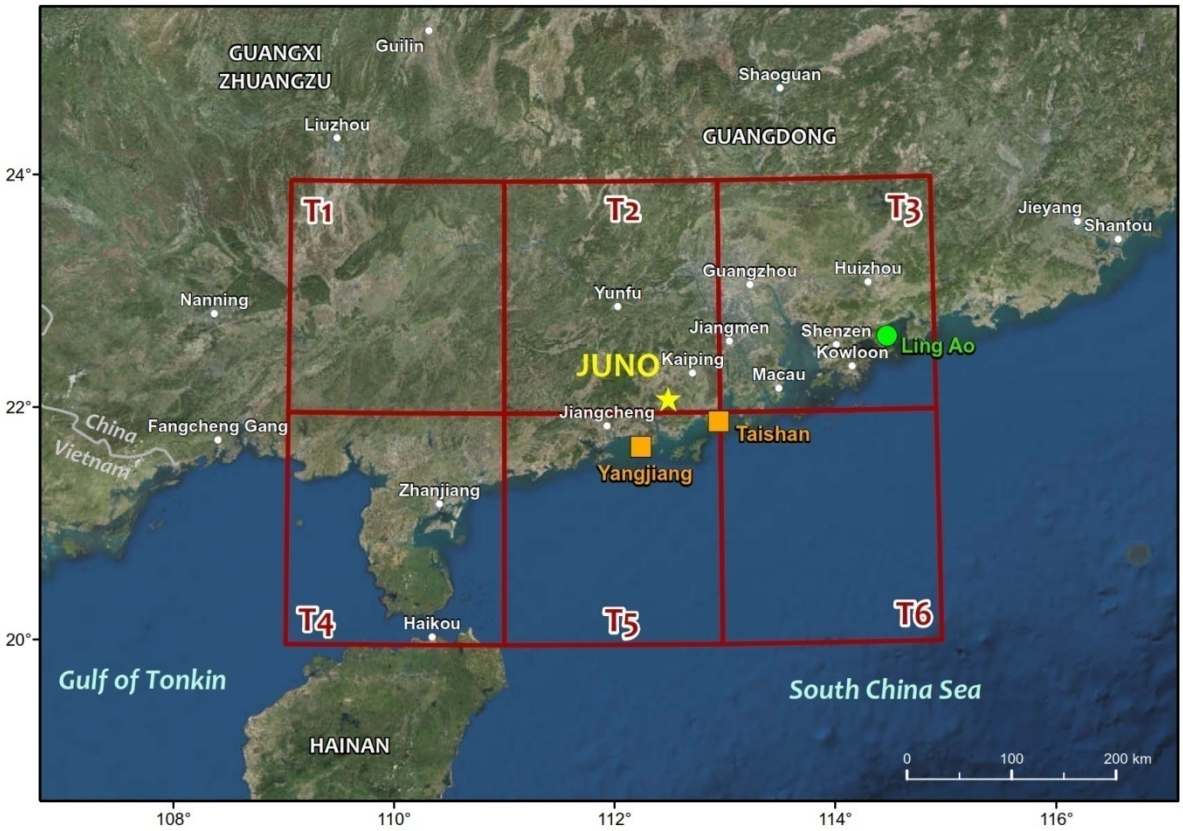

Figure 6.1 Map of LOC surrounding JUNO. JUNO (yellow star) is located in Kaiping, Jiangmen, Guangdong province (South China) and the planned (orange square) and operational (green circle) nuclear power plants. The six 2° × 2° Tiles (dark red lines) define the LOC.

6.2 Methods

The reference Earth model developed in [*Huang et al.*, 2013] provides a description of the abundances and distribution of the Heat-Producing Elements (HPEs, i.e. U, Th and K) in the Earth's crust, along with their uncertainties. According to this model the silicate portion of the Earth is composed of five dominant reservoirs: the Depleted Mantle (DM), the Enriched Mantle (EM), the Lithospheric Mantle (LM), the Continental Crust (CC) and the Oceanic Crust (OC). The continental crust is dominantly composed of Lower Crust (LC), Middle Crust (MC) and Upper Crust (UC) and it is overlain by shallow layers of Sediments (Sed) which also covers the OC.

The surface geoneutrino flux is calculated by dividing the Earth surface in 1° × 1° tiles that are projected vertically into discrete volume cells and each cell is assigned physical and chemical states (see section 5.6). The total crustal thickness of each cell and its associated uncertainty correspond, respectively, to the mean and the half-range of three crustal models obtained from different approaches: the global crustal model based on reflection and refraction data "CRUST 2.0" [*Bassin et al.*, 2000; *Laske et al.*, 2001], the global shear-velocity model of the crust and upper mantle "CUB 2.0" [*Shapiro and Ritzwoller*, 2002] and the high-resolution crustal model "GEMMA" [*Negretti et al.*, 2012; *M. Reguzzoni and*

Sampietro, 2015] based on the GOCE satellite gravity mission [*Drinkwater et al.*, 2003; *Mirko Reguzzoni and Tselfes*, 2009]. The reference model incorporates the relative proportional thickness of the crustal layers along with density and elastic properties (compressional and shear waves velocity) reported in CRUST 2.0. The same information are adopted for the Sed layer using the global sediment map of [*Laske and Masters*, 1997]. In Figure 6.2 the thickness of the continental crust layers in the 24 cells constituting the LOC for JUNO are reported. Their total crustal thickness ranges between 26.3 km and 32.3 km with an uncertainty for each cell of ~7%.

The HPEs abundances in the Sed, OC and UC layers are assumed to be relatively homogenous and correspond to the values reported in Table 3 of [*Huang et al.*, 2013]. The ratio between Felsic and Mafic components in the deep CC (MC and LC) is inferred from seismic velocity data and these data are in turn used to estimate the U and Th content of each cell of the reference crustal model. Focusing on the LOC, the central values of U abundance in MC and LC vary in the range 0.8 - 1.2 μg/g and 0.3 - 0.1 μg/g, respectively. The Th/U ratio in deep CC of the LOC is typically ~5 as compared to a bulk silicate Earth ratio of 3.9 or a bulk CC ratio just greater than 4.0; the higher Th/U ratio in the deep CC is likely due to the greater upward mobility of U during dehydration reactions that accompany granulite facies metamorphism of the deep CC.

In the reference model of [*Huang et al.*, 2013] the LM corresponds to the portion of Earth between the Moho discontinuity and an assumed standard depth of 175 km beneath the surface. The thickness of this unit in the LOC ranges between 143 km and 149 km and its composition is modeled from the database reported in [*McDonough*, 1990] and the update in [*Huang et al.*, 2013]. In our calculation we adopt for the LM the U and Th abundances of $0.03^{+0.05}_{-0.02}$ μg/g and $0.15^{+0.28}_{-0.10}$ μg/g, respectively.

The sublithospheric mantle extends down from the base of the lithosphere to the core-mantle boundary and is divided in two spherically symmetric domains, the Depleted Mantle (DM) and the Enriched Mantle (EM), whose density profiles are derived from the Preliminary Reference Earth Model, "PREM" [*Dziewonski and Anderson*, 1981]. Adopting a mass ratio M_{DM} / M_{EM} = 4.56 [*Arevalo et al.*, 2013], we calculate the masses of these two reservoirs $M_{DM} = 3.207 \cdot 10^{24}$ kg and $M_{EM} = 0.704 \cdot 10^{24}$ kg. In a survey of MidOcean Ridge Basalts (MORB) [*Arevalo and McDonough*, 2010] reported the log-normal based average abundances of $a_{MORB}(U)$ = 80 ng/g and $a_{MORB}(Th)$ = 220 ng/g, and from this calculated the $a_{DM}(U)$ = 8 ng/g and $a_{DM}(Th)$ = 22 ng/g based on a simple melting model. Based on these assumptions the a_{EM} can be calculated:

$$a_{EM}(U) = \frac{M_{BSE}(U) - M_C(U)}{M_{EM}} - a_{DM}(U)\frac{M_{DM}}{M_{EM}}$$

where M_{BSE} (U) = 8.1 $\cdot 10^{16}$ kg is the U mass in the Bulk Silicate Earth (BSE) [*McDonough and Sun*, 1995] and M_C (U) = 3.1 $\cdot 10^{16}$ kg is the total U mass in the crust

[*Huang et al.*, 2013]. The mantle geoneutrino signals reported in Table 6.1 are calculated with $a_{DM}(U) = 8$ ng/g and $a_{EM}(U) = 34$ ng/g together with $(Th/U)_{DM} = 2.8$ and $(Th/U)_{EM} = 4.8$.

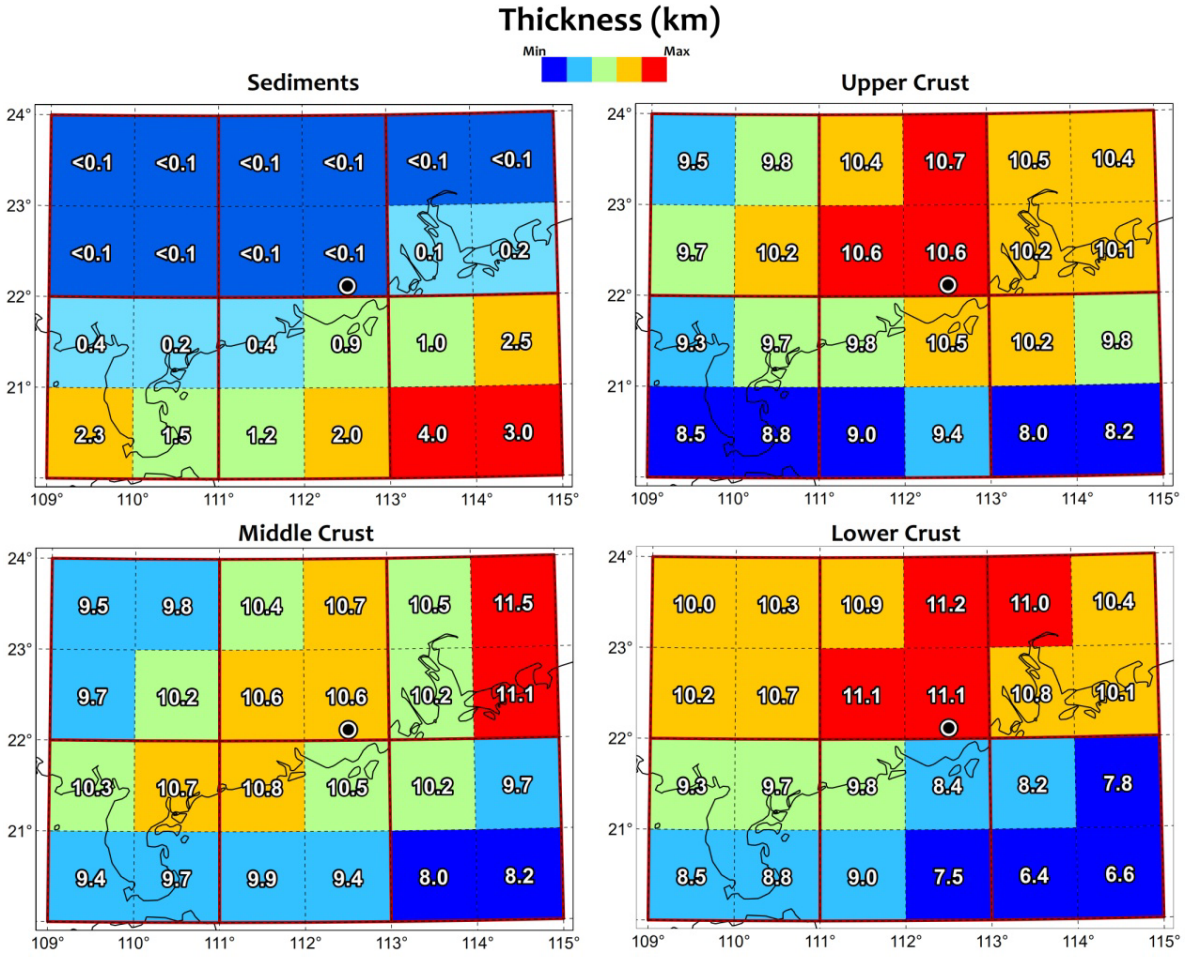

Figure 6.2 Thicknesses of the 4 crustal layers in the LOC. The thicknesses in km of the Sed, UC, MC and LC layers are reported for each of the 24 cells constituting the LOC surrounding JUNO (black circle), with color coding to illustrate gradients in thickness.

6.3 Results and discussions

In Table 6.1 we summarize the contributions to the expected geoneutrino signal at JUNO produced by U and Th in each of the reservoirs identified in the model. The central value and the asymmetric uncertainties are respectively the median and 1σ errors of a positively skewed distribution obtained from Monte Carlo simulation. This approach was developed for the first time in [*Huang et al.*, 2013] in order to combine Gaussian probability density function of geophysical and (some) geochemical inputs, together with the lognormal distributions of U and Th abundances observed in the felsic and mafic rocks of MC and LC.

The total geoneutrino signal at JUNO is $G = 39.7^{+6.5}_{-5.2}$ TNU where the 1σ error only recognizes the uncertainties of the inputs of the lithosphere, which are mainly due to the uncertainties in the composition of the rocks and subsequently to the geophysical inputs. The predicted mantle contribution at JUNO, $S_M \approx 9$ TNU, is estimated with no confidence due to

the large uncertainty accompanying the prediction of the lithospheric contribution, $\delta G \approx \pm 6$ TNU. The expected geoneutrino signal from the mantle is essentially model dependent and it is estimated according to a mass balance argument. An exhaustive discussion of different mantle's structure is described in [*Šrámek et al.*, 2013], in which ranges of geoneutrino signals for different mantle's models are reported.

Table 6.1 Geoneutrino signals from U and Th expected in JUNO. The inputs for the calculations are taken from [*Huang et al.*, 2013] and the signals from different reservoirs indicated in the first column are in TNU.

	S (U)	**S (Th)**	**S (U+Th)**
Sed CC	$0.5^{+0.1}_{-0.1}$	$0.16^{+0.02}_{-0.02}$	$0.64^{+0.1}_{-0.1}$
UC	$14.6^{+3.5}_{-3.4}$	$3.9^{+0.5}_{-0.5}$	$18.5^{+3.6}_{-3.4}$
MC	$4.7^{+3.0}_{-1.8}$	$1.7^{+1.6}_{-0.8}$	$6.8^{+3.6}_{-2.3}$
LC	$0.9^{+0.7}_{-0.4}$	$0.4^{+0.7}_{-0.2}$	$1.5^{+1.0}_{-0.6}$
Sed OC	$0.08^{+0.02}_{-0.02}$	$0.03^{+0.01}_{-0.01}$	$0.11^{+0.02}_{-0.02}$
OC	$0.05^{+0.02}_{-0.02}$	$0.01^{+0.01}_{-0.01}$	$0.06^{+0.02}_{-0.02}$
Bulk Crust	$21.3^{+4.8}_{-4.2}$	$6.6^{+1.9}_{-1.2}$	$28.2^{+5.2}_{-4.5}$
CLM	$1.3^{+2.4}_{-0.9}$	$0.4^{+1.0}_{-0.3}$	$2.1^{+2.9}_{-1.3}$
Total Lithosphere	$23.2^{+5.9}_{-4.8}$	$7.3^{+2.4}_{-1.5}$	$30.9^{+6.5}_{-5.2}$
DM	4.2	0.8	4.9
EM	2.9	0.9	3.8
Gran Total	$30.3^{+5.9}_{-4.8}$	$9.0^{+2.4}_{-1.5}$	$39.7^{+6.5}_{-5.2}$

Thus, a future refinement of the abundances and distribution of HPEs in the UC surrounding the JUNO detector is strongly recommended, as this region provides ~ 47% of G and is a significant contributor to the total uncertainty.

Plotting the cumulative geoneutrino signal as a function of the distance from JUNO for the different Earth reservoirs (Figure 6.3), we observe that half of the total signal comes from U and Th in the regional crust that lies within 550 km of the detector. Since the modeling of the geoneutrino flux is based on 1° × 1° cells, we study the signal produced in LOC subdivided in six 2°× 2° tiles (Figure 6.1).

The geoneutrino signals from U and Th in the lithosphere of each tile are reported in Table 6.2 with their uncertainties. The main contribution (27% of G) comes from tile T2 in which the JUNO experiment is located (Figure 6.1). The thick UC in this tile, which is covered by a very shallow layer of Sed (Figure 6.2), is predicted to give a signal of $7.6^{+1.5}_{-1.4}$

TNU. Therefore a refined study of the U and Th content of the UC in tile T2 is a high-value target for improving the accuracy and precision of the predicted geoneutrino signal at JUNO.

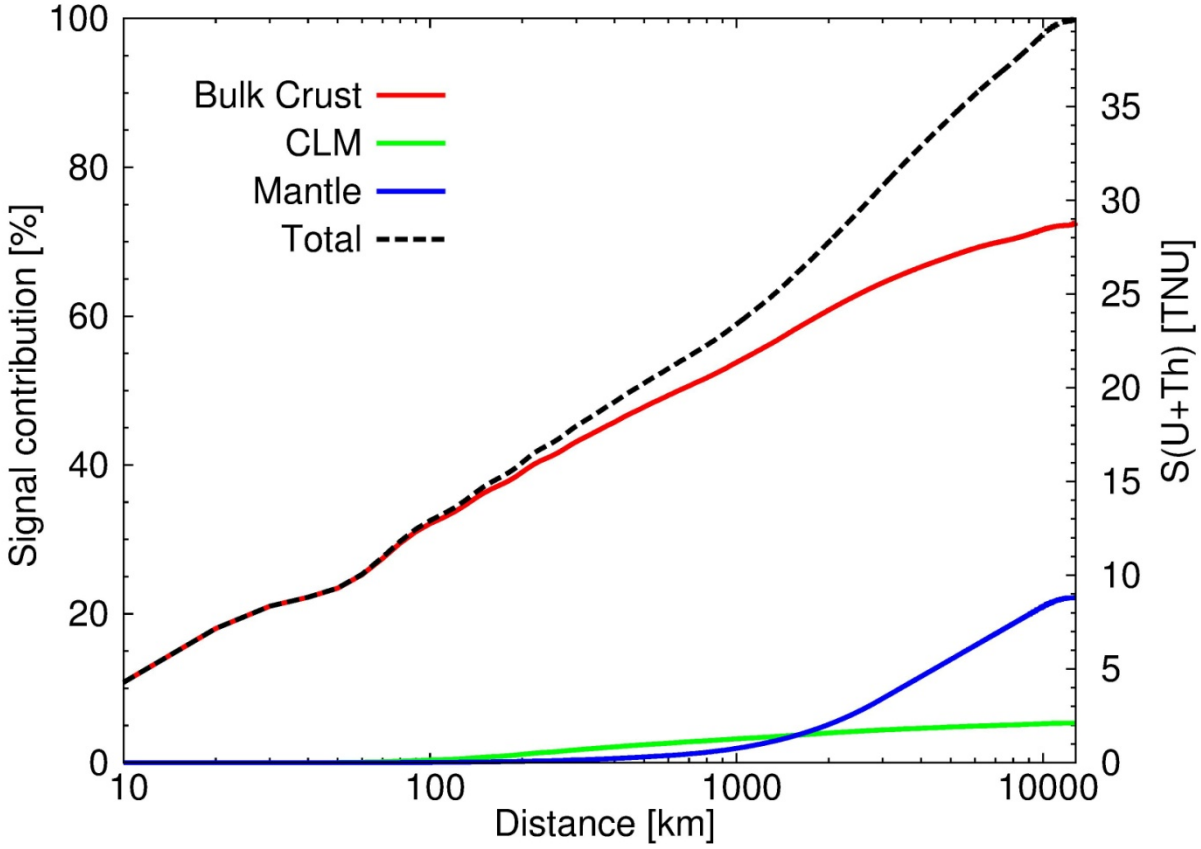

Figure 6.3 Geoneutrino signal contribution. The cumulative geoneutrino signal and the percentage contributions of the Bulk Crust, Continental Lithospheric Mantle (CLM) and Mantle are represented as function of the distance from JUNO.

Table 6.2 Geoneutrino signals from 6 tiles of the LOC. The expected geoneutrino signal in TNU from U and Th contained in the lithosphere (CC+CLM) of the 6 tiles in Figure 6.1. In the last column contributions in percentage are reported.

Tile	S (U)	S (Th)	S (U+Th)	Percentage
T1	$0.4^{+0.1}_{-0.1}$	$0.1^{+0.1}_{-0.1}$	$0.5^{+0.1}_{-0.1}$	3.0
T2	$8.1^{+1.9}_{-1.7}$	$2.6^{+0.8}_{-0.5}$	$10.8^{+2.1}_{-1.8}$	62.1
T3	$1.1^{+0.3}_{-0.2}$	$0.4^{+0.2}_{-0.1}$	$1.5^{+0.3}_{-0.3}$	8.6
T4	$0.3^{+0.1}_{-0.1}$	$0.1^{+0.1}_{-0.1}$	$0.4^{+0.1}_{-0.1}$	2.2
T5	$2.5^{+0.5}_{-0.5}$	$0.7^{+0.2}_{-0.1}$	$3.2^{+0.6}_{-0.5}$	18.2
T6	$0.8^{+0.2}_{-0.2}$	$0.2^{+0.1}_{-0.1}$	$1.0^{+0.2}_{-0.2}$	5.9

Evaluating the antineutrino signal requires knowledge of several ingredients necessary for modeling the three antineutrino life stages: production, propagation to the detector site and detection in liquid scintillation detectors via the IBD reaction. The propagation and detection processes are independent by the source of the particles and we modeled these two stages

using the oscillation parameters from [*Ge et al.*, 2013] and the IBD cross section from [*Strumia and Vissani*, 2003]. Spectral parameters for U and Th geoneutrinos are from [*Fiorentini et al.*, 2007] and modulation of these fluxes are based on [*Huang et al.*, 2013]. Reactor antineutrino production is calculated adopting data from a worldwide reference model from [*Baldoncini et al.*, 2015]. Reported in Figure 6.4 are the energy distributions of geoneutrinos and reactor antineutrino signals in two different scenarios: in the full energy region $R_{OFF} = 95.3^{+2.6}_{-2.4}$ TNU is obtained with data from worldwide commercial reactors operating in 2013 and $R_{ON} = 1566^{+111}_{-100}$ TNU, including the Yangjiang (17.4 GW) and Taishan (18.4 GW) nuclear power plants operating at a 80% annual average load factor [*Baldoncini et al.*, 2015]. In the geoneutrino energy window (i.e. 1.806 - 3.272 MeV) the reactor signal is $S_{OFF} = 26.0^{+2.2}_{-2.3}$ TNU and $S_{ON} = 354^{+45}_{-41}$ TNU (Table 6.3). Assuming a scenario whereby JUNO's signal does not have a background signal from Yangjiang and Taishan nuclear power plants, the ratio of $S_{OFF}/G = 0.7$, which compares to a value of 0.6 for the Borexino detector [*Baldoncini et al.*, 2015]. Considering only the statistical uncertainties, in the R_{OFF} scenario JUNO is an excellent experiment for geoneutrino measurements reaching a 10% accuracy on the geoneutrino signal in approximately 105 days (assuming a $C_{17}H_{28}$ liquid scintillator composition, a 100% detection efficiency and reactor antineutrinos as the sole source of background), given 576 geoneutrino events per year for a target mass of $14.5 \cdot 10^{32}$ free protons. This optimistic expectation doesn't take into account the uncertainties of S_{OFF} and the background due to production of cosmic-muons spallation, accidental coincidences and radioactive contaminants in the detector.

Table 6.3 The total geoneutrino signal (G) is the sum of the contributions from the local lithosphere (S_{LOC}), from the rest of the lithosphere (i.e. Far Field Crust, S_{FFC}) and from the Mantle (SM). The reactor antineutrino signal in the geoeneutrino window is calculated from data for commercial reactors operating all over the world in the 2013 (S_{OFF}) and adding the contribution of the Yangjiang (17.4 GW) and Taishan (18.4 GW) nuclear power plants (S_{ON}) [*Baldoncini et al.*, 2015]. All the signals are expressed in TNU.

	S [TNU]
Local contribution	$17.4^{+3.3}_{-2.8}$
Far Field Crust	$13.4^{+3.3}_{-2.4}$
Mantle	8.8
Gran total geoneutrinos	$39.7^{+6.5}_{-5.2}$
Reactors OFF	$26.0^{+2.2}_{-2.3}$
Reactors ON	354^{+45}_{-41}

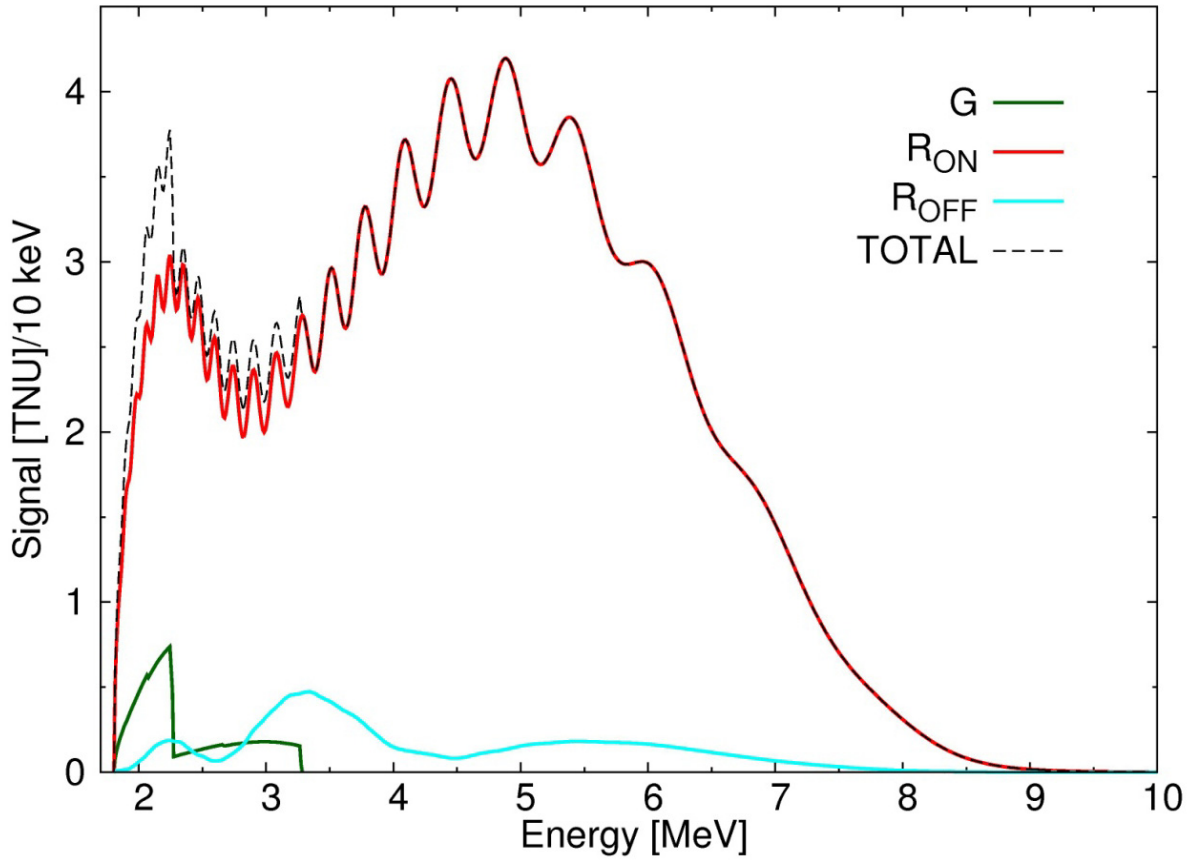

Figure 6.4 Antineutrino energy spectra expected at JUNO. Geoneutrino energy spectrum (green) is reported together with the energy reactor antineutrino spectra computed considering the commercial reactors operating all over the world in 2013 (cyan) and adding the contribution of the Yangjiang and Taishan nuclear power plants (red). The reactor antineutrino spectra are computed assuming normal hierarchy and neutrino oscillation. The total spectrum (black dashed lines) is obtained assuming the R_{ON} scenario.

6.4 Final remarks

Designed as a 20 kton liquid scintillator detector, the JUNO experiment will collect high statistics for antineutrino signals from reactors and from the Earth. In this study we focused on predicting the geoneutrino signal using the Earth reference model of [*Huang et al.*, 2013]. The contribution originating from naturally occurring U and Th in the 6 ° × 4° LOcal Crust (LOC) surrounding the JUNO detector (Figure 6.1) was determined. The main results of this study are summarized as follows.

The thickness of the Sed, UC, MC and LC layers of the 24 1° × 1° cells of the LOC are reported (Figure 6.2). The Moho depth of the continental LOC ranges between 26.3 km and 32.3 km and the uncertainty for each 1° × 1° cell is of the order of 7%.

The total and local geoneutrino signals at JUNO are $G = 39.7^{+6.5}_{-5.2}$ TNU and $S_{LOC} = 17.4^{+3.3}_{-2.8}$ TNU, respectively. The asymmetric 1σ errors are obtained from Monte Carlo simulations and account only for uncertainties from the lithosphere. The major source of uncertainty comes from predicting the abundances and distribution of U and Th in local crustal rocks.

High-resolution seismic data acquired in the LOC can improve the present geophysical model of the crust and CLM, of which the latter is assumed to have a homogenous depth of 175 ± 75 km. The CLM composition is derived from data for U and Th abundances inferred from the peridotite xenoliths and its geoneutrino signal is of $2.1^{+2.9}_{-1.3}$ TNU.

The HPEs in the regional crust extending out to 550 km from the detector produce half of the total expected geoneutrino signal (Figure 3). The U and Th in the 2° × 2° tile that hosts JUNO produces $10.8^{+2.1}_{-1.8}$ TNU corresponding to 27% of G. Since this region is characterized by a thick UC, which gives $7.6^{+1.5}_{-1.4}$ TNU, a refined geophysical and geochemical model of the UC of this tile is highly desired.

The reactor signal in the geoneutrino window assuming two scenarios is S_{OFF} = $26.0^{+2.2}_{-2.3}$ TNU with the 2013 reactor operational data only and $S_{ON} = 355^{+44}_{-41}$ TNU when the contributions of the Yangjiang and Taishan nuclear power plants are added. There is a potential to achieve up to 10% accuracy on geoneutrinos after 105 days of data accumulation, under conditions of Yangjiang and Taishan nuclear power plants being off.

The JUNO experiment has the potential to reach a milestone in geoneutrino science, although some technical challenges must be addressed to minimize background (e.g. production of cosmic-muons spallation, accidental coincidences, radioactive contaminants in the detector). Assuming S_{OFF}/G = 0.7, JUNO can collect hundreds of low background geoneutrino events in less than a year under optimal conditions. A future refinement of the U and Th distribution and abundance in the LOC is strongly recommended. Such data will lead to insights on the radiogenic heat production in the Earth, the composition of the mantle and constraints on the chondritic building blocks that made the planet.

The content of this chapter is based on the following publication:

Strati V., Baldoncini M., Callegari I., Mantovani F., McDonough W.F. and Ricci B. *Expected geoneutrino signal at JUNO* Progress in Earth and Planetary Science (2015) 2(1): 1-7.
DOI: 10.1186/s40645-015-0037-6

Future perspectives

The scientific challenges and the results described in this thesis revealed many questions that will enliven my research activity over the next years. The problems that I addressed also provided to me the occasion to compare and enrich my knowledge in a broader context of international meeting and congresses.

In the past years I developed skills that are not exclusive to any specific branch of science, but are broadly applicable to nuclear physics, geology and nuclear monitoring activities. The studies reported in these six chapters reflect the melting of three fundamental scientific disciplines: (1) Particle physics, (2) Earth science and (3) Statistics. Their interconnections reveals a great potential for advancing the frontiers of knowledge. I had to deal with specific problems that necessarily emerge when different, but not distant, fields of science are called to interact (Figure 7.1).

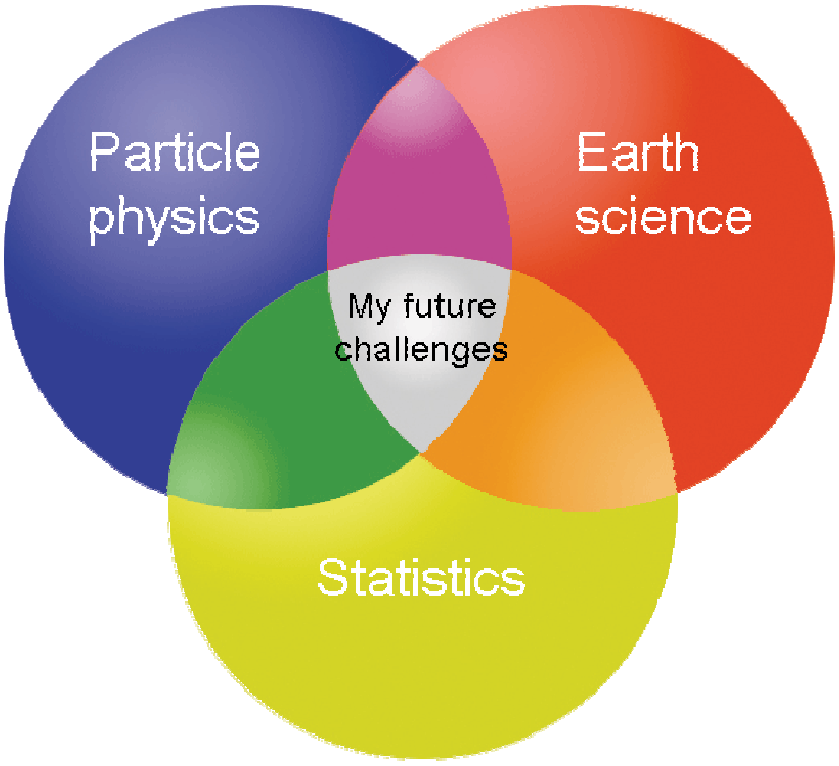

Figure 7.1 The expertise matured during my PhD with respect to the main close disciplines: I see in their overlap the main potential for my scientific progresses**.**

Questions remain as to how to combine geochemical and geophysical uncertainties for building a homogeneous picture of the Earth. Likewise, how can we better identify biases in geochemical databases that come from due to sampling or human subjectivity so to improve the knowledge of radiogenic budget of a terrestrial reservoir? What are the effects of having a log-normal distribution in the concentration of elements in the evaluation of terrestrial heat budget? How might we treat in combination the geoneutrino measurements

from KamLAND, Borexino, SNO+ and JUNO to understand the radiogenic power and radioactivity content of the Earth's mantle? These are just some of the many unsolved questions that a scientist positioned in the intersection of particle physics, Earth science and statistics will face in the next future.

As demonstrated in this thesis, the application of appropriate geostatistical methods implies a rigorous study of the distributions. Even though a lot of efforts have been invested in fitting the experimental frequency distributions with normal or lognormal distributions, geochemical data particularly to trace elements (e.g. uranium and thorium) do not follow an 'a priori distribution'. Concerning this topic, a recent successful research article entitled "*Normal and lognormal data distribution in geochemistry: death of a myth. Consequences for the statistical treatment of geochemical and environmental data*" [*Reimann and Filzmoser*, 2000] animated the debate in the scientific community. The definition of a well-constrained model that describes better the positive abundances, usually right skewed, of trace elements still lacks of knowledge of the complete distribution and this is a complication for geoscientists.

The implementation of a statistically significant dataset constituted by γ-ray measurements of several hundred rock samples collected in Veneto region shed light on the delicate analysis of relevant fractions of measurements below the minimum detection limit. Although this problem is very frequent in many environmental surveys, often not enough attention is paid in the analysis method. Thus, a bias in the estimation of the statistical parameters can be easily introduced.

In the geochemical characterization of the 3D model of the crust near the SNO+ detector, the influence of rare enriched or depleted samples on the lognormal average is controlled by a filter proportional to the sigma of the distribution. We developed a strategy deal with its affects on geochemical datasets, given the presence of outliers data. Indeed often values originated from different distributions associated with processes, that are rare in the environment, are superimposed on the investigated population. The detection of these values is one of the main tasks in the statistical analysis of the geochemical data.

As observed the deviations from normal distributions, the presence of outliers and the treatment of the censored data have strong influences on the calculation of the statistical parameters describing a statistical population. The assessment of NORMs together with the evaluation of the outdoor adsorbed dose rate requires a rigorous statistical study, including reporting of the mean (or median) and standard deviation of the measured sample.

In order to reduce uncertainties in the estimate of crustal geoneutrino signals, a better characterization of the Huronian Supergroup and a refined model of the crust surrounding JUNO are needed. The research documented in the studies reported here reveal the importance of collecting representative rock samples and carrying out a full statistical interpretation of data.

Since the geoneutrino signal originated by U and Th in the mantle is dominated by the crustal one (in absence of a detector located in oceanic crust or directional detectors), careful statistical studies and low-uncertainties crust models are essential ingredients to get insights

about Earth interior. Indeed, the mantle signal can be inferred only subtracting form the experimental data the estimated signal from the crust. In this framework, the combination from ongoing (Borexino and KamLAND) and future experiment (e.g. SNO+ and JUNO) open new perspectives but at the same time shed light on some critical issues related to the treatment of the uncertainties. The U and Th distribution in the crust is not homogenous and so the expected crustal signals at each detector are different but highly correlated. These correlated phenomena have significant consequences for the statistical treatment uncertainties of the subtraction of the various combined crustal signals.

Thanks to incessant technological development, the environmental spatial data will be more frequently gathered using different measurements instruments. In this framework multivariate geostatistical algorithms are available to play a decisive role in making prediction of the distribution of the investigated variables and of the uncertainties on these predictions. The combination of quantitative information, qualitative constraints, and the analysis of different confidence levels the experimental techniques are key points for the elaboration of reliable models.

Bibliography

Abdullah, F. H., H. Saad, and A. Farhan (2013), An investigation of Naturally Occurring Radioactive Material (NORM) in Oilfields and Oil Lakes in Kuwait, *SPE International Conference on Health, Safety, and Environment in Oil and Gas Exploration and Production*.

Adam, E., G. Perron, B. Milkereit, J. Wu, A. J. Calvert, M. Salisbury, P. Verpaelst, and D.-J. Dion (2000), A review of high-resolution seismic profiling across the Sudbury, Selbaie, Noranda, and Matagami mining camps, *Canadian Journal of Earth Sciences*, *37*(2-3), 503-516.

Al-Sulaiti, H., et al. (2012), Determination of the natural radioactivity levels in north west of Dukhan, Qatar using high-resolution gamma-ray spectrometry, *Applied Radiation and Isotopes*, *70*(7), 1344-1350.

Almeida, A. S., and A. G. Journel Joint simulation of multiple variables with a Markov-type coregionalization model, *Mathematical Geology*, *26*(5), 565-588.

Anderson, D. L. (2006), Speculations on the nature and cause of mantle heterogeneity, *Tectonophysics*, *416*(1-4), 7-22.

Antonelli, R., G. Barbieri, G.V. Dal Piaz, A. D. Pra, V. D. Zanche, P. Grandesso, P. Mietto, R. Sedea, and A. Zanferrari (1990), Carta geologica del Veneto - Scala 1:250000, *Servizio Geologico Nazionale*

Araki, T., et al. (2005), Experimental investigation of geologically produced antineutrinos with KamLAND, *Nature*, *436*(7050), 499-503.

Arevalo, R., and W. F. McDonough (2010), Chemical variations and regional diversity observed in MORB, *Chemical Geology*, *271*(1-2), 70-85.

Arevalo, R., W. F. McDonough, A. Stracke, M. Willbold, T. J. Ireland, and R. J. Walker (2013), Simplified mantle architecture and distribution of radiogenic power, *Geochemistry, Geophysics, Geosystems*, *14*(7), 2265-2285.

Atkinson, P. M., R. Webster, and P. J. Curran (1992), Cokriging with ground-based radiometry, *Remote Sensing of Environment*, *41*(1), 45-60.

Avwiri, G. O., and C. P. Ononugbo (2012), Natural Radioactivity Levels in Surface Soil of Ogba/Egbema/Ndoni Oil and Gas Fields, *Energy Science and Technology*, *4*(2), 92-101.

Baldoncini, M., I. Callegari, G. Fiorentini, F. Mantovani, B. Ricci, V. Strati, and G. Xhixha (2015), Reference worldwide model for antineutrinos from reactors, *Physical Review D*, *91*(6), 065002.

Barca, S., L. Carmignani, G. Oggiano, P. Pertusati, I. Salvatori, and L. Carmignani (1996), Carta geologica della Sardegna, Servizio Geologico Nazionale, *Litografia Artistica Cartografica, Firenze*.

Bassin, C., G. Laske, and T. G. Masters (2000), The current limits of resolution for surface wave tomography in North America, *EOS Trans.*

Bea, F. (2012), The sources of energy for crustal melting and the geochemistry of heat-producing elements, *Lithos*, *153*, 278-291.

Bellini, G., et al. (2010), Observation of geo-neutrinos, *Physics Letters B*, *687*(4–5), 299-304.

Bellini, G., et al. (2013), Measurement of geo-neutrinos from 1353 days of Borexino, *Physics Letters B*, *722*(4–5), 295-300.

Benn, K., and J.-F. Moyen (2008), The Late Archean Abitibi-Opatic terranes, Superior Province: a Late Archean oceanic plateau modified by subduction and slab window magmatism, in *When Did Plate Tectonics Begin on Planet Earth?*, edited by V. Pease and K. C. Condie, Geological Society of America Special Publication, Boulder.

Beqiraj, I., S. Drushku, B. Seiti, and D. Topi (2010), Environmental problems in Albanian fields of production and processing of the petroleum, paper presented at 4th International Symposium of Ecologists of Montenegro, Budva, Montenegro, 6-10 October 2010.

Bierkens, M. F. P., and P. A. Burrough (1993), The indicator approach to categorical soil data, *Journal of Soil Science*, *44*(2), 361-368.

Bierwirth, P. N., and R. S. Brodie (2008), Gamma-ray remote sensing of aeolian salt sources in the Murray–Darling Basin, Australia, *Remote Sensing of Environment*, *112*(2), 550-559.

BIPM, IEC, IFCC, ISO, IUPAC, IUPAP, and OIML (2008), Evaluation of Measurement Data—Supplement 1 to the 'Guide to the Expression of Uncertainty in Measurement'—Propagation of Distributions Using a Monte Carlo Method, *Bureau International des Poids et Mesures*(JCGM 101).

Bochicchio, F., et al. (2005), Annual average and seasonal variations of residential radon concentration for all the Italian Regions, *Radiation Measurements*, *40*(2-6), 686-694.

Boerner, D. E., B. Milkereit, and A. Davidson (2000), Geoscience impact: a synthesis of studies of the Sudbury Structure, *Canadian Journal of Earth Sciences*, *37*(2-3), 477-501.

Bonin, B. (2007), A-type granites and related rocks: Evolution of a concept, problems and prospects, *Lithos*, *97*(1-2), 1-29.

Borexino Collaboration (2015), Spectroscopy of geo-neutrinos from 2056 days of Borexino data, *Submitted to Physical Review D*.

Bortolotti, V., M. Fazzuoli, E. Pandeli, G. Principi, A. Babbini, and S. Corti (2001), Geology of central and eastern Elba island, Italy, *Ofioliti*, *26*(2a), 97-150.

Brown, L., L. Jensen, J. Oliver, S. Kaufman, and D. Steiner (1982), Rift structure beneath the Michigan Basin from COCORP profiling, *Geology*, *10*(12), 645-649.

Buttafuoco, G., A. Tallarico, G. Falcone, and I. Guagliardi (2009), A geostatistical approach for mapping and uncertainty assessment of geogenic radon gas in soil in an area of southern Italy, *Environ Earth Sci*, *61*(3), 491-505.

Caciolli, A., et al. (2012), A new FSA approach for in situ γ ray spectroscopy, *Science of The Total Environment*, *414*(0), 639-645.

Callegari, I., et al. (2013), Total natural radioactivity, Tuscany, Italy, *Journal of Maps*, *9*(3), 438 - 443.

Capozzi, F., E. Lisi, and A. Marrone (2014), Neutrino mass hierarchy and electron neutrino oscillation parameters with one hundred thousand reactor events, *Physical Review D*, *89*(1), 013001.

Card, K. D. (1990), A review of the Superior Province of the Canadian Shield, a product of Archean accretion, *Precambrian Research*, *48*(1–2), 99-156.

Carr, S. D., R. M. Easton, R. A. Jamieson, and N. G. Culshaw (2000), Geologic transect across the Grenville orogen of Ontario and New York, *Canadian Journal of Earth Sciences*, *37*(2-3), 193-216.

Carroll, S. S., and T. R. Carroll (1989), Effect of forest biomass on airborne snow water equivalent estimates obtained by measuring terrestrial gamma radiation, *Remote Sensing of Environment*, *27*(3), 313-319.

Casini, L., S. Cuccuru, M. Maino, G. Oggiano, and M. Tiepolo (2012), Emplacement of the Arzachena Pluton (Corsica–Sardinia Batholith) and the geodynamics of incoming Pangaea, *Tectonophysics*, *544–545*(0), 31-49.

Casini, L., S. Cuccuru, A. Puccini, G. Oggiano, and P. Rossi (2015a), Evolution of the Corsica–Sardinia Batholith and late-orogenic shearing of the Variscides, *Tectonophysics*, *646*, 65-78.

Casini, L., S. Cuccuru, M. Maino, G. Oggiano, A. Puccini, and P. Rossi (2015b), Structural map of Variscan northern Sardinia (Italy), *Journal of Maps*, *11*(1), 75-84.

CD2013/59/EURATOM (2014), Council Directive 2013/59/Euratom of 5 December 2013 laying down basic safety standards for protection against the dangers arising from exposure to ionising radiation, and repealing Directives 89/618/Euratom, 90/641/Euratom, 96/29/Euratom, 97/43/Euratom and 2003/122/Euratom, *Official Journal of the European Union*, *57*.

CGT (2011), Accordo di programma quadro ricerca e trasferimento tecnologico per il sistema produttivo - c.1. geologia e radioattività naturale - sottoprogetto a: Geologia (regional framework program for research and technological transfer to industry, c.1. geology and natural radioactivity, sub-project a: Geology). *Technical report, CGT Center for GeoTechnologies, University of Siena; Tuscany Region: Italian Ministry of Education, University and Research*.

Chen, M. C. (2006), Geo-neutrinos in SNO+, *Earth, Moon, and Planets*, *99*(1-4), 221-228.

Chiles, J.-P., and P. Delfiner (1999), *Geostatistics: modeling spatial uncertainty. Probability and Statistics Series*.

Christensen, N. I., and W. D. Mooney (1995), Seismic velocity structure and composition of the continental crust: A global view, *Journal of Geophysical Research-Solid Earth*, *100*(B6), 9761-9788.

Coltorti, M., et al. (2011), U and Th content in the Central Apennines continental crust: A contribution to the determination of the geo-neutrinos flux at LNGS, *Geochimica et Cosmochimica Acta*, *75*(9), 2271-2294.

Corsini, M., and Y. Rolland (2009), Late evolution of the southern European Variscan belt: Exhumation of the lower crust in a context of oblique convergence, *Comptes Rendus Geoscience*, *341*(2-3), 214-223.

Cruciani, G., M. Franceschelli, H.-J. Massonne, R. Carosi, and C. Montomoli (2013), Pressure–temperature and deformational evolution of high-pressure metapelites from Variscan NE Sardinia, Italy, *Lithos*, *175–176*, 272-284.

Deraisme, J., and M. Strydom (2009), Estimation of iron ore resources integrating diamond and percussion drillholes, paper presented at APCOM

Desbarats, A. J., C. E. Logan, M. J. Hinton, and D. R. Sharpe (2002), On the kriging of water table elevations using collateral information from a digital elevation model, *Journal of Hydrology*, *255*(1-4), 25-38.

Dickinson, W. R. (1985), Interpreting Provenance Relations from Detrital Modes of Sandstones, *Mathematical and Physical Sciences* 333-361.

Dini, A., S. Rocchi, D. S. Westerman, and F. Farina (2002a), The late Miocene intrusive complex of Elba Island: two centuries of studies from Savi to Innocenti, *Acta Vulcanologica*, *2*, 213-229.

Dini, A., F. Mazzarini, G. Musumeci, and S. Rocchi (2008), Multiple hydro-fracturing by boron-rich fluids in the Late Miocene contact aureole of eastern Elba Island (Tuscany, Italy), *Terra Nova*, *20*(4), 318-326.

Dini, A., F. Innocenti, S. Rocchi, S. Tonarini, and D. S. Westerman (2002b), The magmatic evolution of the late Miocene laccolithdyke granitic complex of Elba Island, Italy, *Geological Magazine*, *139*(03), 257-279.

Doyen, P. M., L. D. den Boer, and W. R. Pillet (2013), Seismic Porosity Mapping in the Ekofisk Field Using a New Form of Collocated Cokriging.

Drinkwater, M. R., R. Floberghagen, R. Haagmans, D. Muzi, and A. Popescu (2003), GOCE: ESA's First Earth Explorer Core Mission, *17*, 419-432.

Duranti, S., R. Palmeri, P. C. Pertusati, and C. A. Ricci (1992), Geological evolution and metamorphic petrology of the basal sequences of Eastern Elba (Complex II), *Acta Vulcanologica*, *2*, 213-229.

Dye, S. T. (2010), Geo-neutrinos and silicate earth enrichment of U and Th, *Earth Planet. Sci. Lett.*, *297*(1-2), 1-9.
Dye, S. T. (2012), Geoneutrinos and the radioactive power of the Earth, *Reviews of Geophysics*, *50*(3).
Dziewonski, A. M., and D. L. Anderson (1981), Preliminary reference Earth model, *Physics of the Earth and Planetary Interiors*, *25*, 297-356.
Easton, R. (2000), Variation in crustal level and large-scale tectonic controls on rare-metal and platinum-group element mineralization in the Southern and Grenville provinces, *Ontario Geological Survey, Open File Report 6032*, 28-21-28-16.
Eaton, D. W., S. Dineva, and R. Mereu (2006), Crustal thickness and VP/VS variations in the Grenville orogen (Ontario, Canada) from analysis of teleseismic receiver functions, *Tectonophysics*, *420*(1–2), 223-238.
Epili, D., and R. F. Mereu (1991), The Grenville Front Tectonic Zone: Results from the 1986 Great Lakes Onshore Seismic Wide-Angle Reflection and Refraction Experiment, *Journal of Geophysical Research*, *96*(B10), 16335.
Farina, F., A. Dini, F. Innocenti, S. Rocchi, and D. S. Westerman (2010), Rapid incremental assembly of the Monte Capanne pluton (Elba Island, Tuscany) by downward stacking of magma sheets, *Geological Society of America Bulletin*, *122*(9-10), 1463-1479.
Finger, F., M. P. Roberts, B. Haunschmid, A. Schermaier, and H. P. Steyrer (1997), Variscan granitoids of central Europe: their typology, potential sources and tectonothermal relations, *Mineralogy and Petrology*, *61*(1-4), 67-96.
Fiorentini, G., M. Lissia, and F. Mantovani (2007), Geo-neutrinos and earth's interior, *Physics Reports*, *453*(5-6), 117-172.
Fiorentini, G., G. Fogli, E. Lisi, F. Mantovani, and A. Rotunno (2012), Mantle geoneutrinos in KamLAND and Borexino, *Physical Review D*, *86*(3).
Fiorentini, G., A. Ianni, G. Korga, M. Lissia, F. Mantovani, L. Miramonti, L. Oberauer, M. Obolensky, O. Smirnov, and Y. Suvorov (2010), Nuclear physics for geo-neutrino studies, *Physical Review C*, *81*(3).
Fogli, G. L., E. Lisi, A. Marrone, D. Montanino, A. Palazzo, and A. M. Rotunno (2012), Global analysis of neutrino masses, mixings, and phases: Entering the era of leptonic CP violation searches, *Physical Review D*, *86*(1), 013012.
Fountain, D. M., and M. H. Salisbury (1996), Seismic properties of rock samples from the Pikwitonei granulite belt - God's lake domain crustal cross section, Manitoba, *Canadian Journal of Earth Sciences*, *33*(5), 757-768.
Fountain, D. M., M. H. Salisbury, and J. Percival (1990), Seismic structure of the continental crust based on rock velocity form the Kapuskasing uplift, *Journal of Geophysical Research-Solid Earth and Planets*, *95*(B2), 1167-1186.
Gando, A., et al. (2013), Reactor on-off antineutrino measurement with KamLAND, *Physical Review D*, *88*(3), 033001.
Gando, A., et al. (2011), Partial radiogenic heat model for Earth revealed by geoneutrino measurements, *Nature Geoscience*, *4*(9), 647-651.
Garfagnoli, F., F. Menna, E. Pandeli, and G. Principi (2004), Stratigraphy and tectonic etamorphic evolution of the Porto Azzurro UNit in the Monte Calamita promontory (Southeastern ELba island, Tuscany), *Ofioliti*, *29*(2), 269.
Gaschnig, R., R. L. Rudnick, W. F. McDonough, Z. Hu, S. Gao, and A. J. Kaufman (2014), Onset of oxidative continental weathering recorded by transition metal concentrations in ancient glacial deposits, *Geology*, *In Review*.
Ge, S.-F., K. Hagiwara, N. Okamura, and Y. Takaesu (2013), Determination of mass hierarchy with medium baseline reactor neutrino experiments, *J. High Energ. Phys.*, *2013*(5), 1-23.

Geis, W. T., F. A. Cook, A. G. Green, B. Milkereit, J. A. Percival, and G. F. West (1990), Thin thrust sheet formation of the Kapuskasing structural zone revealed by Lithoprobe seismic reflection data, *Geology*, *18*(6), 513-516.

Gerdes, A., G. Worner, and A. Henk (2000), Post-collisional granite generation and HT-LP metamorphism by radiogenic heating: the Variscan South Bohemian Batholith, *Journal of the Geological Society*, *157*(3), 577-587.

Goovaerts, P. (1997), *Geostatistics for natural resources evaluation. Oxford University Press, Oxford, New York*.

Grasty, R. L. (2004), The annual effective dose from natural sources of ionising radiation in Canada, *Radiation Protection Dosimetry*, *108*(3), 215-226.

Greeman, D. J., A. W. Rose, J. W. Washington, R. R. Dobos, and E. J. Ciolkosz (1999), Geochemistry of radium in soils of the Eastern United States, *Applied Geochemistry*, *14*(3), 365-385.

Guastaldi, E., et al. (2013), A multivariate spatial interpolation of airborne γ-ray data using the geological constraints, *Remote Sensing of Environment*, *137*(0), 1-11.

Guri, A., S. Guri, A. Aliu, and O. Lubonja (2013), The Impact of Oil Development Activities on Environment and Sustainable Development in Fier Area, Albania, *Academic Journal of Interdisciplinary Studies*.

Havancsák, I., F. Koller, J. Kodolányi, C. Szabó, V. Hoeck, and K. Onuzi (2012), Chromite-hosted Silicate Melt Inclusions from Basalts in the Stravaj Complex, Southern MirditaOphiolite Belt (Albania), *Turkish Journal of Earth Sciences*, *21*, 79-96.

Helsel, D. R. (1990), Less than obvious - statistical treatment of data below the detection limit, *Environmental Science & Technology*, *24*(12), 1766-1774.

Hengl, T., N. Toomanian, H. I. Reuter, and M. J. Malakouti (2007), Methods to interpolate soil categorical variables from profile observations: Lessons from Iran, *Geoderma*, *140*(4), 417-427.

Hinze, W. J., J. W. Bradley, and A. R. Brown (1978), Gravimeter survey in the Michigan Basin deep borehole, *Journal of Geophysical Research: Solid Earth*, *83*(B12), 5864-5868.

Holm, D. K., R. Anderson, T. J. Boerboom, W. F. Cannon, V. Chandler, M. Jirsa, J. Miller, D. A. Schneider, K. J. Schulz, and W. R. Van Schmus (2007), Reinterpretation of Paleoproterozoic accretionary boundaries of the north-central United States based on a new aeromagnetic-geologic compilation, *Precambrian Research*, *157*(1-4), 71-79.

Howell, P. D., and B. A. van der Pluijm (1999), Structural sequences and styles of subsidence in the Michigan basin, *Geological Society of America Bulletin*, *111*(7), 974-991.

Hrichi, H., S. Baccouche, and J.-E. Belgaied (2013), Evaluation of radiological impacts of tenorm in the Tunisian petroleum industry, *Journal of Environmental Radioactivity*, *115*, 107-113.

Huang, Y., V. Chubakov, F. Mantovani, R. L. Rudnick, and W. F. McDonough (2013), A reference Earth model for the heat-producing elements and associated geoneutrino flux, *Geochemistry, Geophysics, Geosystems*, *14*(6), 2023-2029.

Huang, Y., V. Strati, F. Mantovani, S. B. Shirey, and W. F. McDonough (2014), Regional study of the Archean to Proterozoic crust at the Sudbury Neutrino Observatory (SNO+), Ontario: Predicting the geoneutrino flux, *Geochemistry, Geophysics, Geosystems*, *15*(10), 3925 - 3944.

Hudson, G., and H. Wackernagel (1994), Mapping temperature using kriging with external drift: Theory and an example from scotland, *International Journal of Climatology*, *14*(1), 77-91.

IAEA (1991), Airborne gamma-ray spectrometry surveying. Technical Report Series 323, *Technical Report Series 323, International Atomic Energy Agency, Vienna.*

IAEA (2003), Guidelines for radioelement mapping using gamma ray spectrometry data, *IAEA-TECDOC-1363*.
IAEA (2010), Radioelement mapping, *IAEA nuclear energy series*, *No. NF-T-1.3, Vienna*.
ICDD (2013), Powder Diffraction File (PDF), PDF-2 Release, *International Centre for Diffraction Data*.
Javoy, M., et al. (2010), The chemical composition of the Earth: Enstatite chondrite models, *Earth Planet. Sci. Lett.*, *293*(3-4), 259-268.
Jibiri, N. N., and C. M. Amakom (2010), Radiological Assessment of Radionuclide Contents in Soil Waste Streams from an Oil Production Well of a Petroleum Development Company in Warri, Niger Delta, Nigeria, *Indoor and Built Environment*, *20*(2), 246-252.
Journel, A. G. (1986), Constrained interpolation and qualitative information—The soft kriging approach, *Mathematical Geology*, *18*(3), 269-286.
Keller, J. V. A., and M. P. Coward (1996), The structure and evolution of the Northern Tyrrhenian Sea, *Geological Magazine*, *133*(01), 1-16.
Kemski, J., A. Siehl, R. Stegemann, and M. Valdivia-Manchego (2001), Mapping the geogenic radon potential in Germany, *Science of The Total Environment*, *272*(1–3), 217-230.
Kim, S.-B. (2013), Proposal for RENO-50, paper presented at International Workshop on RENO-50, Seoul National University, Korea, June 13-14.
Laske, G., and T. G. Masters (1997), A global digital map of sediment thickness, *EOS Trans. AGU*, *78 F483*.
Laske, G., T. G. Masters, and C. Reif (2001), CRUST 2.0: A new global crustal model at 2 x 2 degrees, edited, http://igppweb.ucsd.edu/~gabi/crust2.html.
Laske, G., G. Masters, Z. Ma, and M. Pasyanos (2013), Update on CRUST1.0 - A 1-degree global model of Earth's crust, *Geophys. Res. Abstracts*, *15*, Abstract EGU2013-2658.
Learned, J. G., S. T. Dye, and S. Pakvasa (2008), Hanohano: a deep ocean anti-neutrino detector for unique neutrino physics and geophysics studies, paper presented at Proceedings of the Twelfth International Workshop on Neutrino Telescopes, Venice, March 2007, Venice, March 2007.
Lexa, O., K. Schulmann, V. JanouŠEk, P. ŠTÍPskÁ, A. Guy, and M. Racek (2011), Heat sources and trigger mechanisms of exhumation of HP granulites in Variscan orogenic root, *Journal of Metamorphic Geology*, *29*(1), 79-102.
Li (2014), Overview of the Juangmen Undergorun Neutrino Observatory (JUNO), *arXiv:1402.6143 [hep-ex, Physics:physics] http://arxiv.org/abs/1402.6143*.
Li, and Y.-L. Zhou (2014), Shifts of neutrino oscillation parameters in reactor antineutrino experiments with non-standard interactions, *Nuclear Physics B*, *888*(0), 137-153.
Li, J. Cao, Y. Wang, and L. Zhan (2013), Unambiguous determination of the neutrino mass hierarchy using reactor neutrinos, *Physical Review D*, *88*(1), 013008.
Li, X.-H., M. Faure, and W. Lin (2014), From crustal anatexis to mantle melting in the Variscan orogen of Corsica (France): SIMS U–Pb zircon age constraints, *Tectonophysics*, *634*(0), 19-30.
Lightfoot, P. C., A. J. Naldrett, and G. G. Morrison (1997a), Sublayer and offset dikes of the Sudbury Igneous Complex - an introduction and field guide*Rep.*, 37 pp, Ontario Geological Survey, Open File Report 5956.
Lightfoot, P. C., W. Doherty, K. P. Farrell, M. Moore, and D. Pekeski (1997b), Geochemistry of the main mass, sublayer, offsets, and inclusions from the Sudbury Igneous Complex, Ontario*Rep.*, 231 pp, Ontario Geological Survey, Open File Report 5959.
Lightfoot, P. C., R. R. Keays, G. G. Morrison, A. Bite, and K. P. Farrell (1997c), Geologic and geochemical relationships between the contact sublayer, inclusions, and the main

mass of the Sudbury Igneous Complex; a case study of the Whistle Mine Embayment, *Economic Geology*, *92*(6), 647-673.

Long, D. G. F. (2004), The tectonostatigraphic evolution of the Huronian basement and the subsequent basin fill: geological constraints on impact models of the Sudbury event, *Precambrian Research*, *129*(3–4), 203-223.

Long, D. G. F. (2009), The Huronian Supergroup*Rep.*, 14-30 pp, Ontario Geological Survey.

Ludden, J., and A. Hynes (2000), The Lithoprobe Abitibi-Grenville transect: two billion years of crust formation and recycling in the Precambrian Shield of Canada, *Canadian Journal of Earth Sciences*, *37*(2-3), 459-476.

Maino, M., L. Casini, A. Ceriani, A. Decarlis, A. Di Giulio, S. Seno, M. Setti, and F. M. Stuart (2015), Dating shallow thrusts with zircon (U-Th)/He thermochronometry--The shear heating connection, *Geology*, *43*(6), 495-498.

Mantovani, F., L. Carmignani, G. Fiorentini, and M. Lissia (2004), Antineutrinos from Earth: A reference model and its uncertainties, *Physical Review D*, *69*(1).

Mareschal, J., and C. Jaupart (2004), Variations of surface heat flow and lithospheric thermal structure beneath the North American craton, *Earth and Planetary Science Letters*, *223*(1-2), 65-77.

Mazzarini, F., G. Musumeci, and A. R. Cruden (2011), Vein development during folding in the upper brittle crust: The case of tourmaline-rich veins of eastern Elba Island, northern Tyrrhenian Sea, Italy, *Journal of Structural Geology*, *33*(10), 1509-1522.

McDonough, and Sun (1995), The composition of the Earth, *Chemical Geology*, *120*, 223-253.

McDonough, W. F. (1990), Constraints on the composition of the continental lithospheric mantle, *Earth Planet. Sci. Lett.*, *101*(1), 1-18.

McDonough, W. F., and S. S. Sun (1995), The composition of the Earth, *Chemical Geology*, *120*, 223-253.

Mereu, R. F., et al. (1986), The 1982 COCRUST seismic experiment across the Ottawa–Bonnechere graben and Grenville Front in Ontario and Quebec, *Geophysical Journal of the Royal Astronomical Society*, *84*(3), 491-514.

Milkereit, B., A. Green, J. Wu, D. White, and E. Adam (1994), Integrated seismic and borehole geophysical study of the Sudbury Igneous Complex, *Geophysical Research Letters*, *21*(10), 931-934.

Minty, B. (2011), Airborne geophysical mapping of the Australian continent, *GEOPHYSICS*, *76*(5), A27-A30.

Minty, B., and P. McFadden (1998), Improved NASVD smoothing of airborne gamma-ray spectra, *Exploration Geophysics*, *29*(4), 516-523.

Mohamud, A. H., J. S. Cózar, J. Rodrigo-Naharro, and L. Pérez del Villar (2015), Distribution of U and Th in an Iberian U-fertile granitic complex (NW, Spain): airborne-radiometry, chemical and statistical approaches, *Journal of Geochemical Exploration*, *148*(0), 40-55.

Musacchio, G., W. D. Mooney, J. H. Luetgert, and N. I. Christensen (1997), Composition of the crust in the Grenville and Appalachian Provinces of North America inferred from Vp/Vs ratios, *Journal of Geophysical Research: Solid Earth (1978–2012)*, *102*(B7), 15225-15241.

Musumeci, G., and L. Vaselli (2012), Neogene deformation and granite emplacement in the metamorphic units of northern Apennines (Italy): Insights from mylonitic marbles in the Porto Azzurro pluton contact aureole (Elba Island), *Geosphere*, *8*(2), 470-490.

Musumeci, G., F. Mazzarini, M. Tiepolo, and G. Di Vincenzo (2011), U□Pb and 40Ar□39Ar geochronology of Palaeozoic units in the northern Apennines: determining protolith age and alpine evolution using the Calamita Schist and Ortano Porphyroid, *Geological Journal*, *46*(4), 288-310.

Naldrett, A. J., and R. H. Hewins (1984), The Main Mass of the Sudbury Igneous Complex*Rep.*, 235-252 pp, Ontario Geological Survey.

Negretti, M., M. Reguzzoni, and D. Sampietro (2012), A web processing service for GOCE data exploitation, in *First International GOCE Solid Earth workshop*, edited, Enschede, The Netherlands.

O'Neill, H. S. C., and H. Palme (2008), Collisional erosion and the non-chondritic composition of the terrestrial planets, *Philosophical Transactions of the Royal Society A: Mathematical, Physical and Engineering Sciences*, *366*(1883), 4205-4238.

Oggiano, G., G. Cherchi, A. Aversano, A. Di Pisa, A. Ulzega, P. Orrù, and C. Pintus (2005), Note illustrative della Carta Geologia d'Italia, Foglio 428 Arzachena, *S. EL. CA, Firenze*.

Ostrosi, B., V. Qirici, and A. Grazhdani (1998), The heavy minerals shore placers of Adriatic Sea in Albania, *Bulletin of the Geological Society of Greece*, *32*(3), 173-177.

Pagel, M. (1982), The Mineralogy and Geochemistry of Uranium, Thorium, and Rare-Earth Elements in Two Radioactive Granites of the Vosges, France, *Mineralogical Magazine*, *46*(339), 149-161.

Pandeli, E., M. Puxeddu, and G. Ruggieri (2001), The metasiliciclastic-carbonate sequence of the Acquadolce Unit (eastern Elba Island): new petrographic data and paleogeographic interpretation, *Ofioliti*, *26*(2a), 207-2018.

Pardo-Igúzquiza, E., and P. A. Dowd (2005), Multiple indicator cokriging with application to optimal sampling for environmental monitoring, *Computers & Geosciences*, *31*(1), 1-13.

Pease, V., J. A. Percival, H. Smithies, G. Stevens, and M. J. van Kranendonk (2008), When did plate tectonics begin? Evidence from the orogenic record, in *When Did Plate Tectonics Begin on Planet Earth?*, edited by V. Pease and K. C. Condie, Geological Society of America Special Publication, Boulder.

Pei, T., C.-Z. Qin, A. X. Zhu, L. Yang, M. Luo, B. Li, and C. Zhou (2010), Mapping soil organic matter using the topographic wetness index: A comparative study based on different flow-direction algorithms and kriging methods, *Ecological Indicators*, *10*(3), 610-619.

Peiffert, C., C. nguyen-Trung, and M. Cuney (1996), Uranium in granitic magmas: Part 2. Experimental determination of uranium solubility and fluid-melt partition coefficients in the uranium oxide-haplogranite-H2O-NaX (X = Cl, F) system at 770°C, 2 kbar, *Geochimica et Cosmochimica Acta*, *60*(9), 1515-1529.

Percival, J. A. (2007), Eo- to Mesoarchean terranes of the Superior Province and their tectonic content, in *Earth's Oldest Rocks*, edited by M. J. van Kranendonk, H. Smithies and V. C. Bennett, pp. 1065-1086, Elserier, Amsterdam.

Percival, J. A., and G. F. West (1994), The Kapuskasing uplift: a geological and geophysical synthesis, *Canadian Journal of Earth Sciences*, *31*(7), 1256-1286.

Percival, J. A., and Z. E. Peterman (1994), Rb–Sr biotite and whole-rock data from the Kapuskasing uplift and their bearing on the cooling and exhumation history, *Canadian Journal of Earth Sciences*, *31*(7), 1172-1181.

Pérez-Soba, C., C. Villaseca, D. Orejana, and T. Jeffries (2014), Uranium-rich accessory minerals in the peraluminous and perphosphorous Belvís de Monroy pluton (Iberian Variscan belt), *Contributions to Mineralogy and Petrology*, *167*(5).

Perry, H. K. C., J. C. Mareschal, and C. Jaupart (2009), Enhanced crustal geo-neutrino production near the Sudbury Neutrino Observatory, Ontario, Canada, *Earth Planet. Sci. Lett.*, *288*(1-2), 301-308.

Perry, H. K. C., C. Jaupart, J. C. Mareschal, and G. Bienfait (2006), Crustal heat production in the Superior Province, Canadian Shield, and in North America inferred from heat flow data, *Journal of Geophysical Research*, *111*(B4).

Pollack, H. N., and D. S. Chapman (1977), On the regional variation of heat flow, geotherms, and lithospheric thickness, *Tectonophysics*, *38*(3–4), 279-296.
Popescu, B. M. (1994), Hydrocarbons of Eastern Central Europe: Habitat, Exploration and Production History, *Springer-Verlag Berlin Heidelberg*, 1-27.
Prifti, I., and K. Muska (2013), Hydrocarbon occurrences and petroleum geochemistry of Albanian oils, *Italian Journal of Geosciences*, *132*(2), 228-235.
Reed, J. C. J., J. O. Wheeler, and B. E. Tucholke (2005), Geological Map of North America, The Geological Society of America, Boulder.
Reguzzoni, M., and N. Tselfes (2009), Optimal multi-step collocation: application to the space-wise approach for GOCE data analysis, *Journal of Geodesy*, *83*(1), 13-29.
Reguzzoni, M., and D. Sampietro (2015), GEMMA: An Earth crustal model based on GOCE satellite data, *International Journal of Applied Earth Observation and Geoinformation*, *35*, 31-43.
Reimann, and P. Filzmoser (2000), Normal and lognormal data distribution in geochemistry: death of a myth. Consequences for the statistical treatment of geochemical and environmental data, *Environmental Geology*, *39*(9), 1001-1014.
Reimann, C. (2005), Geochemical mapping: technique or art?, *Geochemistry: Exploration, Environment, Analysis*, *5*(4), 359-370.
Rivoirard, J. (2001), Which models for Collocated Cokriging?, *Mathematical Geology*, *33*(2), 117-131.
Robertson, A., and M. Shallo (2000), Mesozoic–Tertiary tectonic evolution of Albania in its regional Eastern Mediterranean context, *Tectonophysics*, *316*(3–4), 197-254.
Rossi, and A. Cocherie (1991), Genesis of a Variscan batholith: Field, petrological and mineralogical evidence from the Corsica-Sardinia batholith, *Tectonophysics*, *195*(2–4), 319-346.
Rossi, J. L. Dungan, and L. R. Beck (1994), Kriging in the shadows: Geostatistical interpolation for remote sensing, *Remote Sensing of Environment*, *49*(1), 32-40.
Roure, F., et al. (2010), The use of palaeo-thermo-barometers and coupled thermal, fluid flow and pore-fluid pressure modelling for hydrocarbon and reservoir prediction in fold and thrust belts, *Geological Society, London, Special Publications*, *348*(1), 87-114.
Rousell, D. H., H. L. Gibson, and I. R. Jonasson (1997), The tectonic, magmatic and mineralization history of the Sudbury Structure, *Exploration and Mining Geology*, *6*(1), 1-22.
Rudnick, R. L., and D. M. Fountain (1995), Nature and composition of the continental crust: A lower crustal perspective, *Reviews of Geophysics*, *33*(3), 267-309.
Rudnick, R. L., and S. Gao (2003), Composition of the continental crust, in *The Crust, Vol. 3 Treatise on Geochemistry*, edited by R. L. Rudnick, pp. 1-64, Elsevier, Oxford.
Rybach, L., B. Bucher, and G. Schwarz (2001), Airborne surveys of Swiss nuclear facility sites, *Journal of Environmental Radioactivity*, *53*(3), 291-300.
Saint-Fort, R., M. Alboiu, and P. Hettiaratchi (2007), Evaluation of TENORMs field measurement with actual activity concentration in contaminated soil matrices, *Journal of Environmental Science and Health, Part A*, *42*(11), 1649-1654.
Salisbury, M. H., and D. M. Fountain (1994), The seismic velocity and Poisson's ratio structure of the Kapuskasing uplift from laboratory measurements, *Canadian Journal of Earth Sciences*, *31*(7), 1052-1063.
Sanderson, D. C. W., A. J. Cresswell, F. Hardeman, and A. Debauche (2004), An airborne gamma-ray spectrometry survey of nuclear sites in Belgium, *Journal of Environmental Radioactivity*, *72*(1-2), 213-224.
Santawamaitre, T., D. Malain, H. A. Al-Sulaiti, D. A. Bradley, M. C. Matthews, and P. H. Regan (2014), Determination of 238U, 232Th and 40K activity concentrations in

riverbank soil along the Chao Phraya river basin in Thailand, *Journal of Environmental Radioactivity*, *138*, 80-86.
Schetselaar, E. (2000), Integration of Landsat TM, Gamma-Ray, Magnetic, and Field Data to Discriminate Lithological Units in VegetatedGranite-Gneiss Terrain, *Remote Sensing of Environment*, *71*(1), 89-105.
Schwarz, G. F., E. Klingelé, and L. Rybach (1992), How to handle rugged topography in airborne gamma-ray spectrometry surveys, *First Break 10*(1), 7.
Shapiro, N. M., and M. H. Ritzwoller (2002), Monte-Carlo inversion for a global shear-velocity model of the crust and upper mantle, *Geophysical Journal International*, *151*, 88-105.
Shawky, S., H. Amer, A. A. Nada, T. M. Abd El-Maksoud, and N. M. Ibrahiem (2001), Characteristics of NORM in the oil industry from Eastern and Western deserts of Egypt, *Applied Radiation and Isotopes*, *55*(1), 135-139.
Silo, E., K. Muska, and V. Silo (2013), Hydrocarbon evaluation aspects in neogene clastic reservoirs, Vlora-Elbasan Region, Albania, *Italian Journal of Geosciences*, *132*(2), 220-227.
Smith, S. A. F., R. E. Holdsworth, and C. Collettini (2010), Interactions between low-angle normal faults and plutonism in the upper crust: Insights from the Island of Elba, Italy, *Geological Society of America Bulletin*, *123*(1-2), 329-346.
Snyder, D., G. Perron, K. Pflug, and K. Stevens (2002), New insights into the structure of the Sudbury Igneous Complex from downhole seismic studies, *Canadian Journal of Earth Sciences*, *39*(6), 943-951.
Spence, G., R. M. Clowes, D. J. White, and Z. Hajnal (2010), Mantle heterogeneities and their significance: results from Lithoprobe seismic reflection and refraction – wide-angle reflection studiesThis article is one of a series of papers published in this Special Issue on the themeLithoprobe — parameters, processes, and the evolution of a continent.Lithoprobe Contribution 1486, *Canadian Journal of Earth Sciences*, *47*(4), 409-443.
Šrámek, O., W. F. McDonough, and J. G. Learned (2012), Geoneutrinos, *Advances in High Energy Physics*, *2012*, 1-34.
Šrámek, O., W. F. McDonough, E. S. Kite, V. Lekić, S. T. Dye, and S. Zhong (2013), Geophysical and geochemical constraints on geoneutrino fluxes from Earth's mantle, *Earth Planet. Sci. Lett.*, *361*, 356-366.
Strati, V., et al. (2015), Total natural radioactivity, Veneto (Italy), *Journal of Maps*, *11*(4), 545-551.
Strumia, A., and F. Vissani (2003), Precise quasielastic neutrino/nucleon cross-section, *Physics Letters B*, *564*(1-2), 42-54.
Tartèse, R., P. Boulvais, M. Poujol, and J.-L. Vigneresse (2011), Granite petrogenesis revealed by combined gravimetric and radiometric imaging, *Tectonophysics*, *501*(1-4), 98-103.
Therriault, A. M., A. D. Fowler, and R. A. F. Grieve (2002), The Sudbury Igneous Complex: A Differentiated Impact Melt Sheet, *Economic Geology*, *97*(7), 1521-1540.
Trevisan, L. (1950), L'Elba orientale e la sua tettonica di scivolamento per gravità. Mem. Ist. Geol. Univ. Padova, *Mem. Ist. Geol. Univ. Padova*, *16*, 5-35.
Trotti, F., R. Biancotto, M. Lanciai, P. Mozzo, F. Predicatori, and A. Tacconi (1994), Indoor Exposure to Natural Radioactivity in Veneto, *Radiation Protection Dosimetry*, *56*(1-4), 309-313.
Trotti, F., A. Tanferi, M. Lanciai, P. Mozzo, V. Panepinto, S. Poli, F. Predicatori, F. Righetti, A. Tacconi, and R. Zorzin (1998), Mapping of Areas with Elevated Indoor Radon Levels in Veneto, *Radiation Protection Dosimetry*, *78*(1), 11-14.

Turcotte, D. L., and G. Schubert (2002), *Geodynamics, applications of continuum physics to geological problems* Cambridge University Press, second edition.

UNSCEAR (2000), Exposures from Natural Radiation Sources, *United Nations Scientific Committee on the Effects of Atomic Radiation, UN, New York.*

UNSCEAR (2008), Health effects due to radiation from the Chernobyl accident, *United Nations Scientific Committee on the Effects of Atomic Radiation, UN, New York.*

Van Schmus, W. R. (2013), Natural Radioactivity of the Crust and Mantle, 283-291.

Van Schmus, W. R., D. A. Schneider, D. K. Holm, S. Dodson, and B. K. Nelson (2007), New insights into the southern margin of the Archean–Proterozoic boundary in the north-central United States based on U–Pb, Sm–Nd, and Ar–Ar geochronology, *Precambrian Research*, *157*(1-4), 80-105.

Wackernagel, H. (2003), *Multivariate Geostatistics: An Introduction With Applications (3rd ed.)*.

Wasserburg, G. J., G. J. F. Macdonald, W. A. Fowler, and F. Hoyle (1964), Relative contribution of uranium, thorium and potassium to heart production in Earth, *Science*, *143*(3605), 465-469.

Weatherill, B., A. C. Seto, S. K. Gupta, and L. Çobo (2013), Cold Heavy Oil Production at Patos-Marinza, Albania, *SPE International Thermal Operations and Heavy Oil Symposium*, 1-18.

Webster, R., and M. Oliver (2001), *Geostatistics for Natural Environmental Scientists*.

Wetterlind, J., B. Tourlière, G. Martelet, J. Deparis, N. P. A. Saby, A. C. Richer de Forges, and D. Arrouays (2012), Are there any effects of the agricultural use of chemical fertiliser on elements detected by airborne gamma-spectrometric surveys?, *Geoderma*, *173–174*(0), 34-41.

White, D. J., D. A. Forsyth, I. Asudeh, S. D. Carr, H. Wu, R. M. Easton, and R. F. Mereu (2000), A seismic-based cross-section of the Grenville Orogen in southern Ontario and western Quebec, *Canadian Journal of Earth Sciences*, *37*(2-3), 183-192.

Winardhi, S., and R. F. Mereu (1997), Crustal velocity structure of the Superior and Grenville provinces of the southeastern Canadian Shield, *Canadian Journal of Earth Sciences*, *34*(8), 1167-1184.

Wynne-Edwards, H. R. (1972), The Grenville Province, in *Variations in Tectonic Styles in Canada: Geological Association of Canada Special Paper*, edited by R. J. W. Douglas, pp. 263-334.

Xhixha, G., et al. (2015), Calibration of HPGe detectors using certified reference materials of natural origin, *J Radioanal Nucl Chem*.

Xhixha, G., et al. (2013), The worldwide NORM production and a fully automated gamma-ray spectrometer for their characterization, *J Radioanal Nucl Chem*, *295*(1), 445-457.

Xu, W., T. T. Tran, R. M. Srivastava, and A. G. Journel (1992), Integrating Seismic Data in Reservoir Modeling: The Collocated Cokriging Alternative.